

Master's thesis

A first-principles study of point defects in w-AlN for quantum technologies

Luis Roberto Jimenez Arteta
luisrj@uio.no

Physics
60 ECTS study points

Department of Physics
Faculty of Mathematics and Natural Sciences

Spring 2025



Luis Roberto Jimenez Arteta
luisrj@.ui.no

A first-principles study of point
defects in w-AlN for quantum
technologies

Supervisor:
Marianne Etzelmüller Bathen
Morten Hjorth-Jensen
Christopher Linderälv
David Rivas Gongora

"One thing I have learned in a long life that all our science, measured against reality, is primitive and childlike and yet it is the most precious thing we have."

Albert Einstein
(1879-1955)

To my ghostwriter

Abstract

NO READY YET

In this project, it is studied (AlN) since it makes a promising material for applications in quantum technologies as a potential host for defects acting as solid-state (**SPEs**) and spin qubits for coherent spin manipulation. The aim will be to study different point defects in AlN and assess their suitability for quantum technologies (**QT**).

This thesis investigates the role of defects in AlN, focusing on their applications in quantum technologies, particularly for spin qubits and single-photon emitters. The primary goal is to examine different defects using insights from the literature to identify those exhibiting the desired behavior. This is achieved by studying various defects through first-principles calculations based on density functional theory (**DFT**). After these calculations, the defects are analyzed by examining the Kohn-Sham (**KS**) eigenvalues and the localization factor of the single **KS** wavefunction. The localization factor is determined using two methods: ion orbital weights (**IOWs**) and the inverse participation ratio (**IPR**). Additionally, the spin-charge transition level energies for different defects are computed. Furthermore, configuration coordinate diagrams (**CCDs**) are used to analyze the zero-phonon line (**ZPL**), absorption and emission transition energies. The final analysis involves many-body perturbation theory (**MBPT**) calculations for selected defects to refine the transition energy levels.

List of Figures

2.1	A two-dimensional Bravais lattice and the resulting crystal structure formed by adding a basis to each lattice point.	4
2.2	Illustration of various unit cell choices in a square 2D crystal system, representing the primitive unit cells (blue), the conventional unit cell (green), and the Wigner–Seitz cell (red).	6
2.3	Schematic chematic representation of the LCAOs approach for the simplest case of the hydrogen molecule, illustrating bonding and antibonding molecular orbital formation.	9
2.4	Illustration of band formation in solids through the LCAOs approach. The figure indicates the progression from an isolated atomic system ($N = 1$) to a large number of atoms (solid), showing the evolution of energy levels as two, three, four, five, and very large of atoms are brought together. It also represents the valence band (VB) and the conduction band (CB) in a solid.	10
2.5	Classification of crystalline materials based on their band structure: conductors, semiconductors, and insulators.	11
2.6	Energy dispersion for free electron problem in a big box, where for simplicity $\mathbf{k} = k_x$ and $k_y, k_z = 0$. This meaning moving only in the k_x direction	13
2.7	Schematic direct and indirect band gaps, from the fact that the VBM and CBM do not necessarily lie at the same wavector \mathbf{k} for all semiconductors.	14
2.8	Illustration electron distribution in intrinsic semiconductor at temperature $T > 0$	16
2.9	Illustration of n-type and p-type semiconductor at temperature $T > 0$	17
2.10	Illustration of different types of point defects in a binary material. Those labels with (a) are simples point defects, (b) are two example of complex defects	18
2.11	Illustration of a shallow and deep defect leves in semiconductors.	19
2.12	Illustration desired two-level quantum system in deep defect levels . . .	21
2.13	w-AlN primitive unit cell and stacing AB bilayers	22
2.14	The first BZ for hexagoal structure and the higer-symetric points Γ , A, L, M, K, and H	22
2.15	Illustration of the different selected point defects: V_N , V_{Al} , Al_N , C_N , $V_{Al}V_N$, and C_NC_{Al}	23
3.1	Schematic representation of the PES	30
4.1	Illustration of the supercell approach for a point defect using PBC . .	42
4.2	Flowchart of the SCF KS method	44

5.1	Formation energy diagram for a defect X consider 3 different charge states, (a) it is a full formation energy diagram, (b) resumed formation energy diagram	52
5.2	Khon-Shan eigenvalues and orbital localization factor spectrum	54
5.3	Configuration coordination diagram of a defect X under harmonic approximation for the ground and excited state.	55
6.1	Energy cutoff convergence test for the w-AlN unit cell.	58
6.2	\mathbf{k} -point density convergence test for w-AlN unit cell.	60
6.3	Supercell size convergence test for w-AlN	61
6.4	Orbital localization factors of the KS eigenvalue distribution for the neutral nitrogen vacancy (\mathbf{V}_N^0), calculated using PBE at the Γ -point: (a) for a supercell size of $6 \times 6 \times 3$, and (b) for a supercell size of $5 \times 5 \times 3$. In the figure, the orbital localization factors are represented by the color bar, with yellow/green indicating localized states and purple indicating delocalized states.	63
6.5	Orbital localization factors of the KS eigenvalue distribution for the neutral nitrogen vacancy \mathbf{V}_N^0 , calculated using HSE06 at the Γ -point: (a) for a supercell size of $6 \times 6 \times 3$, and (b) for a supercell size of $5 \times 5 \times 3$. In the figure, the orbital localization factors are represented by the color bar, with yellow/green indicating localized states and purple indicating delocalized states.	63
6.6	Energy cutoff convergence test for w-AlN supercell	64
6.7	\mathbf{k} -point density convergence test for w-AlN supercell	65
6.8	Band structure and total density of states for w-AlN	66
6.9	Defect formation energies	68
6.10	Metastability of \mathbf{V}_N^{-1} in the two different spin electronic configurations: $s = 1$ and $s = 0$, with the specified localized orbitals a and e denoting singly and doubly degenerate orbital states, respectively. These spin configurations are constructed based on the KS eigenstate distribution and their corresponding orbital localization factors (Figure. A.3).	69
6.11	Scheme showing the Kohn–Sham eigenvalue distribution for \mathbf{V}_N^0	74
6.12	Khon-Shan eigenvalue distibution and corresponding orbital localization factor for $(\mathbf{V}_{\text{Al}}\mathbf{V}_N)^{+2}$	74
6.13	Scheme showing the Kohn–Sham eigenvalue distribution for $\mathbf{V}_{\text{Al}}^{0/-2/-3}$	75
6.14	Khon-Shan eigenvalue distibution and corresponding orbital localization factor for $\mathbf{V}_{\text{Al}}^{0/-1/-2}$	76
6.15	Scheme showing the Kohn–Sham eigenvalue distribution for $\mathbf{Al}_N^{+2/+1/0}$	77
6.16	Khon-Shan eigenvalue distibution and corresponding orbital localization factor for $\mathbf{V}_{\text{Al}}^{+2/+1/0}$	78
6.17	Scheme showing the Kohn–Sham eigenvalue distribution for \mathbf{V}_N^{-1} , $(\mathbf{V}_N\mathbf{V}_{\text{Al}})^{-1}$ and $(\mathbf{C}_N\mathbf{C}_{\text{Al}})^{+1}$	80
6.18	Khon-Shan eigenvalue distibution and corresponding orbital localization factor for \mathbf{C}_N^0 , $(\mathbf{V}_N\mathbf{V}_{\text{Al}})^{-1}$ and $(\mathbf{C}_N\mathbf{C}_N)^{+1}$	81
A.1	Unit cell	87
A.2	Supercell	88

A.3	Khon-Shan eigenvalue distribution and corresponding orbital localization factor for V_N^{-1} in the two different metastable spin electronic configurations: $s = 1$ and $s = 0$	90
A.4	Khon-Shan eigenvalue distribution and corresponding orbital localization factor for $(V_N V_{AL})^{+2/0}$ in the stable spin electronic configurations: $s = 1$	91

List of Tables

2.1	Different 2D lattice systems, including the number of Bravais lattices and their corresponding geometric parameters.	5
2.2	Different 3D lattice systems, including the number of Bravais lattices and their corresponding geometric parameters.	5
6.1	Calculated values from the energy cutoff convergence test for w-AlN unit cell	59
6.2	Calculated values from the \mathbf{k} -point density unit cell convergnce test for w-AlN unit cell	60
6.3	Calculated values of the size test for w-AlN	61
6.4	Bulk structure properties of w-AlN calculated using PBE and HSE06 approximation and experimental	65
6.5	Chemical potentials at the upper limit of the constituent elements are used in the calculation of formation energies.	67
6.6	Electronic spin states and formation energies interception with the VBM of the selected defects using PBE	69
6.7	Thermodynamics charge TTLs and ionization energies for different defect calculated using PBE : V_N , V_{Al} , Al_N , C_N , $V_{Al}V_N$, and $C_N C_{Al}$	70
6.8	Selected charged defects and their corresponding spin states.	72
6.9	Zero phonon line energy for V_N^0	74
6.10	Zero phonon line energy for $V_{Al}^{0/-2}$	76
6.11	Zero phonon line energy for $Al_N^{+2/+1/0}$	78
6.12	Zero phonon line for C_N^0	81
A.1	Calculated values of the energy cutoff test for w-AlN	88
A.2	Calculated values of the energy cutoff test for w-AlN	89

Contents

Abstract	iii
List of figures	v
List of tables	viii
1 Introduction	1
Introduction	1
2 Background for defects in semiconductors	3
2.1 Introduction to crystalline materials	3
2.1.1 Bravais lattice	3
2.1.2 Reciprocal space	7
2.2 Cohesion energy and origin of band structure	8
2.3 Density of states (DOS) and Fermi-Dirac distribution	11
2.4 Semiconductor materials	14
2.4.1 Band structure	14
2.4.2 Intrinsic semiconductors and charge concentration	15
2.4.3 Doping	16
2.5 Point defects in semiconductor materials	17
2.5.1 Point defect concentration	18
2.5.2 Impact of point defects on semiconductor properties	19
2.5.3 Defect application in quantum technology (QT)	20
2.6 Wurtzite Aluminum Nitride (w-AlN)	21
2.6.1 Crystal structure and bulk properties of w-AlN	21
2.6.2 Defects in w-AlN as candidates for QT	22
3 Many-Body Quantum Mechanics in Crystalline Systems	25
3.1 Schrödinger equation	25
3.2 Periodic potential and Bloch theorem	27
3.3 Many-particle Schrödinger equation	28
3.4 Born-Oppenheimer approximation (BOA)	29
3.5 Variational principle in quantum mechanics	30
3.6 Hartree and Hartree-Fock approximation	31
3.6.1 Hartree approximation	31
3.6.2 Hartree-Fock approximation	33
3.7 Density Functional Theory (DFT)	34
3.7.1 The Hohenberg-Kohn theorems	34
3.7.2 The Kohn-Sham (KS) equations	36
3.7.3 Approximations to the exchange-correlation (XC) energy	38

3.8	Beyond Hartree–Fock theory	39
3.8.1	Many-body perturbation theory (MBPT)	39
3.8.2	Green’s Function Theory (GFT) and GW approximation (GW)	39
4	A brief overview of the implemented computational methods	41
4.1	Supercell approach and period boundary conditions	41
4.2	Implementation of the KS wave functions	42
4.3	Self-consistent field (SCF) method	43
4.4	Practical considerations	44
4.5	$\mathbf{G}_0\mathbf{W}_0$ calculations	45
5	Methodology	47
5.1	Convergence tests	47
5.2	Defect formation energies	48
5.2.1	Chemical potentials and limits	49
5.2.2	Finite size corrections in supercell calculations	51
5.2.3	Formation energy diagrams	51
5.2.4	Thermodynamics charge transition levels (CTLs)	52
5.3	KS eigenvalues and orbital localization factor (KSOLF)	53
5.4	Optical properties of defects: Zero phonon line (ZPL)	54
5.5	$\mathbf{G}_0\mathbf{W}_0$ calculations for the selected promising charged defects	56
6	Results and discussion	57
6.1	Numerical details	57
6.1.1	Unit cell convergence	58
6.1.2	Supercell convergence	61
6.2	Bulk properties and electronic structure of w-AlN	65
6.3	Defect analysis: native, impurity and complex	66
6.3.1	Literature study: Initial defect selection	67
6.3.2	Formation energy diagram and thermodynamic transition levels	67
6.3.3	Selected defect charge states	71
6.3.4	Electronic configuration of selected defect charge states	72
6.3.5	Further study of the promising charge defects using $\mathbf{G}_0\mathbf{W}_0$	82
7	Concluding remarks	83
7.1	Conclusions	83
7.2	Future work	83
Appendices		84
A	Further results and convergence test	87
A.1	Convergence tests: force, pressure	87
A.2	Convergence table	88
A.3	KS eigenvalue distribution and their corresponding orbital localization factor	90
A.3.1	PBE	90
A.3.2	HSE06	91
Bibliography		93

Chapter 1

Introduction

In the last century, quantum technologies (**QT**) have emerged as one of the most investigated fields within the natural sciences and technology due to the revolutionary potential of nowadays technologies. The **QT** is a large and growing field that including as main areas quantum computing (**QC**), quantum sensing and quantum communication. The idea behind these new technologies are to use the unique properties of quantum systems to develop devices. Among all **QT**, **QC** is perhaps the most researched, because it has the potential to influence in almost every single area of science and practical human problem. With the power of **QC** will likely become possible to model very complex physical systems, such as large molecules and even solid-state systems or to solve human problems like inverse reaction of molecules in the human body. These are just two examples, but there are many cases where using **QT** provides completely new capabilities. On the other hand, quantum sensing is linked to the development of **QC** and quantum communication and other emerging **QT**, it relies on extremely sensitive measurements of the properties of quantum systems. Furthermore, its applications extend to improving instruments for measuring temperature, radiation, pressure, and other variables in modern technology. While, quantum communication represents a more powerful and secure way to communicate, which is quite important for the future quantum computers [1–5].

The basis of quantum computer is given by the quantum bit or qubit represented for the quantum states $|0\rangle$ and $|1\rangle$. A qubit is the fundamental unit of quantum information, analogous to a classical bit in traditional computing. However, the difference comes in the behavior of both. The classical bit can be only in one state, either 0 or 1, at any given time. A qubit, on the other hand, can exist in multiple states simultaneously due to a property of quantum mechanics called superposition $|\psi\rangle = \alpha|0\rangle + \beta|1\rangle$.

Currently, it is possible to construct a qubit in different ways through available platforms. The most used and that have shown the best results with the **QC** of today are superconducting qubits. Other examples of promising qubit platforms include quantum dots, nuclear spin of molecules, electrons on liquid helium, and point defects in semiconductors [6–10]. All of these qubit platforms are based on the concept of creating a quantum two-level system, which can be initialized to generate a quantum superposition, manipulated to control specific quantum properties such as entanglement, superposition, and tunneling, and subsequently read out to produce the desired output. It is important to note that while two discrete levels are not strictly necessary, they are often the most suitable or convenient choice in many cases. The primary challenges with most qubit platforms are scalability and stability, both of which are particularly important for developing practical applications that harness the power of **QT**. Particularly, prolonged

stability is essential for maintaining the coherence time (superposition) of the qubit, which should be as long as possible to facilitate quantum gate operations and readout.

Existing quantum computers are not exempt from this issue, requiring very low temperatures to achieve long coherence times, leaving significative challenges in terms of fabrication and scalability. Therefore, alternative platforms are becoming increasingly interesting as they aim to avoid complications associated with very low temperatures. One of the most attractive options is the point defect platform, which has been demonstrated long quantum coherence time at room temperature while maintaining potential scalability [9, 11]. Additionally, a single photon emitter (**SPE**) has been measured on them [9, 12]. A **SPEs** or single-photon source (**SPS**) is a quantum system that emits exactly one photon at a time or features a measurable delay between the emissions of photons. This last property is highly useful for quantum communication protocols, which relies on **SPEs** [4]. To utilize point defects as a basis for **QT**, host materials with wideband gaps are preferred, as they typically have the ability to induce deep levels between the band edges that can be used to implement different **QT** applications. Some of the most promising candidates include diamond, silicon, silicon carbide, boron nitride, and aluminum nitride [13].

For this reason, this master thesis will explore various point defects in Wurtzite Aluminum Nitride (w-AlN) that can be compatible with quantum technology applications. w-AlN is a semiconductor material with a wideband gap composed of two common elements, aluminum and nitrogen, in which **SPEs** at room temperature have been measured, making it an effective material for technological fabrication and a high-quality candidate for **QT** [14–17]. No less important, it is a well-studied semiconductor in the photoelectronics industry [18, 19].

The defects to be explored include six types: three native defects, which are the nitrogen vacancy (V_N), aluminum vacancy (V_{Al}), and aluminum antisite (Al_N ; one impurity defect, carbon substitutional (C_N); and two complex defects, the divacancy ($V_{Al}V_N$) and the double substitutional carbon or carbon dimer (C_NC_{Al}). For all defects, we would study the spin electronic configuration and stability of the thermodynamic stable charge, which is calculated through defect formation energy theory. Furthermore, a deeper studied of electronic distribution would be carried out to reach a possible **SPE** and spin qubit center.

Calculation will be performed using first-principle calculation, particularity through density functional theory (**DFT**) and a bit of many-body permutation combine with Green's function theory (**GW**). **DFT** is a ground state theory that used the electronic density to determinate all electronic properties of the system. While **GW** is a theory beyond **DFT** that include excitation electronic transition.

Regarding the organization of this thesis, it will be divided into six chapters. The first chapter introduces the background on point defect applications in semiconductor materials. The second chapter describes many-body quantum interactions in crystalline systems. The third chapter expands on the methods used throughout the thesis to derive the results. Following that, a short fourth chapter provides an overview of the computational methods employed to perform the calculations. Finally, the last two chapters discuss the results and present the conclusions. After these chapters, there is an appendix that provides additional details of the result.

Chapter 2

Background for defects in semiconductors

This chapter introduces the background knowledge necessary to understand point defects in semiconductor materials. It will begin by discussing the mathematical framework of crystal systems, defining the Bravais lattice and its corresponding reciprocal space. Following this, the chapter will explore band theory in solids, emphasizing key properties such as the density of states (**DOS**) and charge concentration as they relate to the Fermi-Dirac distribution. A more extensive discussion of these properties in semiconductor materials will follow. Finally, the chapter will cover point defects in semiconductor materials, providing an overview of the specific materials and defects explored in this thesis.

2.1 Introduction to crystalline materials

The atoms in solid systems can be arranged in different forms: amorphous, crystalline, and polycrystalline. Amorphous materials are solids that do not exhibit any long-range ordering. In contrast, crystalline materials are solids in which the constituent atoms, ions, or molecules are arranged in a highly ordered structure, with this ordering or pattern extensively repeated throughout the entire system. On the other hand, polycrystalline materials consist of numerous small crystalline regions, each exhibiting a certain degree of ordering.

Normally, crystalline materials are the most interesting because their ordering gives rise to unique properties that can be utilized for technological applications, particularly in the case of semiconductors [20]. For further information, see [Section 2.4](#). Additionally, they have a much simpler description compared to the other two types, making a deeper understanding possible and enabling manipulation.

From now on, all discussions will be considered within the framework of crystalline materials, which form the main basis for the study presented in this thesis.

2.1.1 Bravais lattice

In crystalline materials or crystals, there is a very important concept called the lattice, or more formally, the Bravais lattice. This mathematical object tracks the periodicity of the crystal and facilitates an easier study of their properties, contributing to a deeper understanding.

Definition

The lattice is an ordered arrangement of point that can be generated by so-called lattice vector \mathbf{R} . For instance, in 3 dimension (**3D**) is defined as,

$$\mathbf{R} = n_1 \mathbf{a}_1 + n_2 \mathbf{a}_2 + n_3 \mathbf{a}_3 . \quad (2.1)$$

In **Equ.** (2.1), \mathbf{a}_i with $i = 1, 2, 3$ are called lattice vector or translation vectors, and n_i are arbitrary integers. The set of all n_i would create the lattice.

Having defined a lattice, we need a one more ingredient to make a crystal, and this is called basis. The basis is essentially the thing that is placed in the lattice, it can be an atom, molecules or more complex systems. For instance, **Figure. 2.1** shows a **2D** lattice with two basis atoms added to generate the crystal.

$$\mathbf{R} = n_1 \mathbf{a}_1 + n_2 \mathbf{a}_2 \implies \mathbf{R}_j = \mathbf{R} + x_j \mathbf{a}_1 + y_j \mathbf{a}_2 , \quad j = 1, 2 . \quad (2.2)$$

In **Equ.** (2.2), \mathbf{R}_j refers to the position of the j^{th} atom in the crystal, while $-1 \leq x_j, y_j \leq 1$ indicates the shift in position with respect to the lattice point \mathbf{R} .

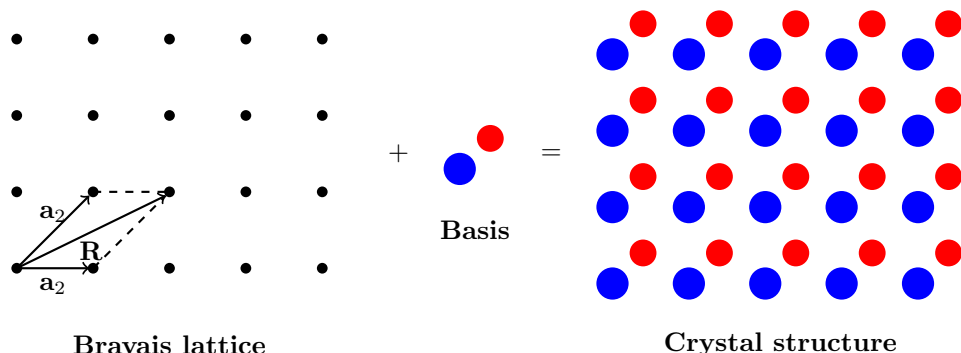


Figure 2.1: A two-dimensional Bravais lattice and the resulting crystal structure formed by adding a basis to each lattice point.

In the initial description, it may appear that a lattice can be constructed in an infinite number of ways; this impression arises because only translational properties, or more formally, translational symmetry, are considered. However, real crystals exhibit additional symmetry operations beyond simple translations, and the accepted lattice structures are constrained by these symmetries.

A symmetry operation in a crystal is a geometric transformation that leaves the entire structural arrangement of the lattice unchanged. For instance, translational symmetry allows the lattice to be shifted by a lattice vector \mathbf{R} without altering its structure. Similarly, rotational symmetry enables the lattice to be rotated by specific angles such as 60° , 90° , 120° , or 180° about certain axes without affecting the entire crystal configuration. Together, these symmetry operations, which may also include mirror reflections, inversion centers, screw axes, and glide planes, define the space group

of the crystal [21, 22]. These constraints significantly reduce the number of distinct lattice types possible and are fundamental to classifying crystalline materials.

Crystals can be classified into 17 and 230 symmetric space groups, encompassing all possible transformations that can be done, resulting in 10 and 32 different point groups of symmetric operations, leading to 5 and 14 distinct lattices in **2D** and **3D** crystals, respectively [21]. Where a point group describes all the symmetry operations that can be performed on a system without considering translational symmetry. Consequently, the different lattices are then classified in a subgroup called lattice system, for **2D** this is shown in **Table. 2.1**, with lattice parameters $\|\mathbf{a}_1\| = a$, $\|\mathbf{a}_2\| = b$ and where α is the angle between \mathbf{a}_1 and \mathbf{a}_2 ($\angle(\mathbf{a}_1, \mathbf{a}_2)$). For a **3D** crystal see **Figure. 2.2**, with $\|\mathbf{a}_1\| = a$, $\|\mathbf{a}_2\| = b$, $\|\mathbf{a}_3\| = c$ and $\alpha = \angle(\mathbf{a}_2, \mathbf{a}_3)$, $\beta = \angle(\mathbf{a}_1, \mathbf{a}_3)$, $\gamma = \angle(\mathbf{a}_1, \mathbf{a}_2)$. For both (**2D**) and (**3D**) cases, the number of Bravais lattices associated with each symmetric lattice system is shown. The tables are constructed based on **Refs. [22, 23]**

Table 2.1: Different 2D lattice systems, including the number of Bravais lattices and their corresponding geometric parameters.

Lattice System	Number of Bravais lattices	Geometric parameters
Tetragonal (Square)	1	$a = b, \alpha = 90^\circ$
Orthorhombic (Rectangular)	2	$a \neq b, \alpha = 90^\circ$
Hexagonal	1	$a = b, \alpha = 120^\circ$
Monoclinic (Oblique)	1	$a \neq b, \alpha \neq 90^\circ$

Table 2.2: Different 3D lattice systems, including the number of Bravais lattices and their corresponding geometric parameters.

Lattice system	Number of Bravais lattices	Geometric parameters
Cubic	3	$a = b = c$ $\alpha = \beta = \gamma = 90^\circ$
Tetragonal	2	$a = b \neq c$ $\alpha = \beta = \gamma = 90^\circ$
Orthorhombic	4	$a \neq b \neq c$ $\alpha = \beta = \gamma = 90^\circ$
Hexagonal	1	$a = b \neq c$ $\alpha = \beta = 90^\circ, \gamma = 120^\circ$

Trigonal	1	$a = b = c$ $\alpha = \beta = \gamma < 120 \neq 90^\circ$
Monoclinic	2	$a \neq b \neq c$ $\alpha = \gamma = 90^\circ, \beta \neq 90^\circ$
Triclinic	1	$a \neq b \neq c$ $\alpha \neq \beta \neq \gamma \neq 90^\circ$

For this thesis, the **3D** Hexagonal system is the most interest. Further details are given in **Section 2.6**.

Before moving on, we will discuss another import concept that comes from the lattice definition, which is the unit cell. The unit cell is defined in **2D** and **3D** as any area or volume that, when translated over all the vectors of the lattice would fill space without overlapping and leaving voids, respectively. In **Figure. 2.2** is a schematic for a **2D** Square lattice system. It is shown that there exist many ways to construct the unit cell: primitive (red and blue) or no primitive or conventional (green). The primitive unit cell is a unit cell which contain just one lattice point and conventional unit cell is the opposined contains more than one. Among the all possible primitive unit cells, there is a special one known as the Wigner-Seitz primitive unit cell (red), which is defined by the region that is closer to a given lattice point than to any other. This cell is constructed using the perpendicular lines drawn to the midpoints of the vectors connecting a central lattice point to its nearest neighbors ¹[23].

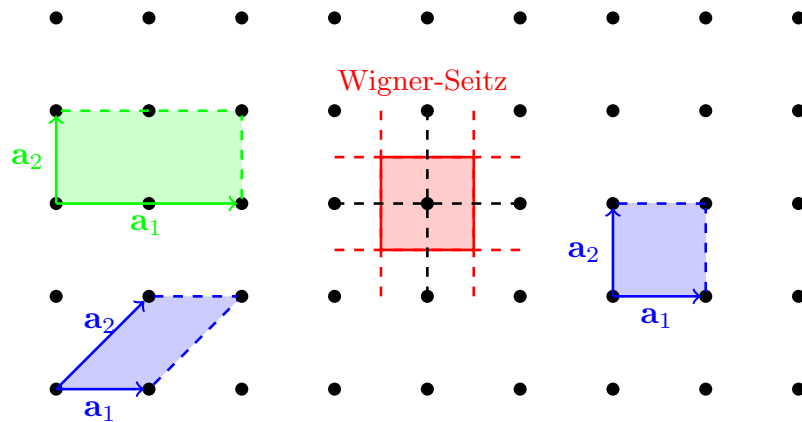


Figure 2.2: Illustration of various unit cell choices in a square 2D crystal system, representing the primitive unit cells (blue), the conventional unit cell (green), and the Wigner–Seitz cell (red).

¹The primitive Wigner-Seitz cell definition can be generalized to any unit cell, it has not to be strictly a primitive unit cell.

2.1.2 Reciprocal space

The physical concept and definition of the reciprocal vector arise naturally from X-ray diffraction theory, particularly in the context of Fourier analysis of X-ray scattering in a crystal. The full scattering theory in crystals is extensive and lies outside the scope of this thesis. Therefore, we will not go into great detail but will instead present a simple idea regarding the origin of this concept using the underlying principles of Fourier analysis. Either way, for a further discussion see Refs. [22–24].

Definition

The reciprocal space, or dual space, is mathematically defined such that each reciprocal lattice vector \mathbf{G} is perpendicular to the corresponding real-space lattice planes formed by each real vector \mathbf{R} (see Equ. (2.1)).

$$\mathbf{G} = m_1 \mathbf{b}_1 + m_2 \mathbf{b}_2 + m_3 \mathbf{b}_3 \implies \mathbf{G} \cdot \mathbf{R} = \mathbf{b}_i \cdot \mathbf{a}_i = 2\pi\delta_{ij}, \quad (2.3)$$

where \mathbf{G} is a reciprocal lattice vector, it shares the same periodicity as the crystal in reciprocal space. From this definition, it can be proven that the reciprocal vectors \mathbf{b}_i with $i = 1, 2, 3$ in Equ. (2.3) are given by

$$\mathbf{b}_1 = 2\pi \frac{\mathbf{a}_2 \times \mathbf{a}_3}{\mathbf{a}_1 \cdot \mathbf{a}_2 \times \mathbf{a}_3}; \mathbf{b}_2 = 2\pi \frac{\mathbf{a}_3 \times \mathbf{a}_1}{\mathbf{a}_1 \cdot \mathbf{a}_2 \times \mathbf{a}_3}; \mathbf{b}_3 = 2\pi \frac{\mathbf{a}_1 \times \mathbf{a}_2}{\mathbf{a}_1 \cdot \mathbf{a}_2 \times \mathbf{a}_3}. \quad (2.4)$$

In Equ. (2.4), the factor 2π arises from physical considerations rather than intrinsic mathematical necessity. Its presence is significant in a physical context, as the reciprocal lattice vectors are defined through Fourier analysis of the periodic real-space lattice with periodicity \mathbf{R} [22, 23].

In a crystal, the electron density must be periodic with periodicity \mathbf{R} (see Equ. (2.1)), which is directly related to the periodicity condition of the ionic positions in the lattice. Thus, it can be expanded in a generalized Fourier series

$$n(\mathbf{r}) = \sum_G n_{\mathbf{G}} e^{i\mathbf{G} \cdot \mathbf{r}} \implies n_{\mathbf{G}} = \frac{1}{V_{cell}} \int_{V_{cell}} n(\mathbf{r}) e^{-i\mathbf{G} \cdot \mathbf{r}} d\mathbf{r}. \quad (2.5)$$

In Equ. (2.5), V_{cell} is the volume of the selected cell [23], for a primitive unit cell this is defined as

$$V_{cell} = |\mathbf{a}_1 \cdot \mathbf{a}_2 \times \mathbf{a}_3|. \quad (2.6)$$

Since $n(\mathbf{r}) = n(\mathbf{r} + \mathbf{R})$, as

$$n(\mathbf{r} + \mathbf{R}) = \sum_G n_{\mathbf{G}} e^{i\mathbf{G} \cdot (\mathbf{r} + \mathbf{R})} = \sum_G e^{i\mathbf{G} \cdot \mathbf{R}} n_{\mathbf{G}} e^{i\mathbf{G} \cdot \mathbf{r}} = n(\mathbf{r}). \quad (2.7)$$

By simple inspection, The only way that Equ. (2.7) can be satisfied is when

$$e^{i\mathbf{G} \cdot \mathbf{R}} = 1 \implies \mathbf{G} \cdot \mathbf{R} = 2\pi. \quad (2.8)$$

The result in Equ. (2.8) relates to the definition of the reciprocal vector in Equ. (2.3) and directly shows that \mathbf{G} corresponds to the periodicity of the crystal in reciprocal-space [22, 23].

As in real-space, the concept of the unit cell can be constructed in reciprocal space, following the same definition. Moreover, the primitive Wigner-Seitz unit cell in reciprocal-space is specifically referred to as the first Brillouin zone (**BZ**). While the generalizations of the Wigner-Seitz unit cells are collectively called Brillouin zones **BZs**, which include the second, third, and so on. See further discussion in Refs. [22, Section 1.2][23, Chapter 1].

2.2 Cohesion energy and origin of band structure

The existence of solid materials in stable form is related with a fundamental quantity called the cohesion energy E_{coh} . The E_{coh} is the energy required to separate an atom or molecule, which constitutes the solid, into its isolated components at an infinite distance from each other. It is defined as

$$E_{coh} = E_{iso} - E_{solid}, \quad (2.9)$$

where E_{iso} is the system parts (atoms or molecules) as if they were isolated, while E_{solid} is related with the total energy of the solid. For stable solid materials, the cohesion energy described in Equ. (2.9) must be greater than zero ($E_{coh} > 0$), implying that the composite system is more stable and likely to form naturally. Conversely, if $E_{coh} < 0$, it indicates that the isolated components of the system are more energetically favorable or stable, and the system should spontaneously break apart. While a larger positive value for the cohesion energy would indicate a measure of how strong the bonding is between the component elements of the solid [22, Section 1.7].

The bonding values can be classified into ranges corresponding to various bonding types. These bonding types in a solid can be summarized as ionic, covalent, metallic, van der Waals, hydrogen, and combinations of these. Here, we will not discuss each all them, and rather say that each binding type gives specific properties to the crystal. For instance, in ionic bonding, electrons are transferred from one atom to another, creating a localized electron state that results in poor conductivity within the crystal. While in metallic bonding, electrons are delocalized, allowing them to move freely through the crystal structure, which makes metals good conductors. For further discussion, see Refs. [22, Section 1.7][23, Chapter 3][24, Chapter 2].

Origin of band structure

In the previous discussion, we introduced cohesive energy to explain why solid elements or molecules are more likely to bond and form more complex structures, without delving into the details of how microscopic bonding is formed or what changes in the system lead to the consideration of a large number of atoms (solid). To go further, we will introduce a simple concept to understand the microscopic behavior resulting from bonding elements or molecules, or larger numbers of them, to construct a solid.

A very intuitive way to think about it is through the linear combination of atomic orbitals (**LCAOs**). As the name suggests, this approach uses the isolated atomic electronic orbitals of the elements to construct molecular orbitals through a linear combination. For instance, Figure. 2.3 presents a schematic of the **LCAOs** approach for the simplest case of the hydrogen molecule. The simplicity of this arises from the fact that hydrogen atoms in their ground state contain only $1s$ orbitals with two possible spin configurations: $\psi_A^{(1s)}$ (up) and $\psi_B^{(1s)}$ (down). This leads to only two possible **LCAOs** for constructing the molecular hydrogen orbitals, known as bonding ($\psi_+ = \frac{1}{\sqrt{2}}(\psi_A^{(1s)} + \psi_B^{(1s)})$)

and antibonding ($\psi_- = \frac{1}{\sqrt{2}}(\psi_A^{(1s)} - \psi_B^{(1s)})$), where $\frac{1}{\sqrt{2}}$ serves as a normalization factor. These molecular orbitals have their own distinct wavefunction distributions (ψ_{\pm}), clearly different from the isolated component state ($\psi_{A,B}^{(1s)}$), this results in different molecular energy states that are split around the isolated ground state of the component elements. For further details, see Ref. [25, Chapter 8].

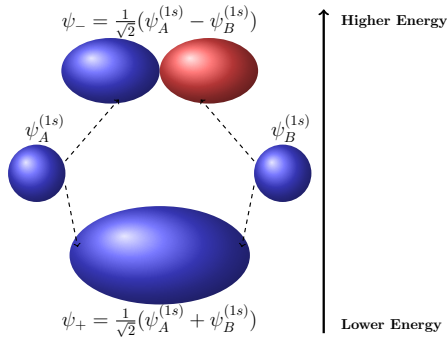


Figure 2.3: Schematic schematic representation of the **LCAOs** approach for the simplest case of the hydrogen molecule, illustrating bonding and antibonding molecular orbital formation.

The **LCAO** theory can be extended to systems with a large number of atoms, such as solids, where the complexity increases significantly due to the vast number of possible combinations between atomic orbitals. In the context of solids, this approach is commonly known as the “*Tight-Binding method*”. Here, this will not be discussed further and simply use the main idea presented above for the hydrogen molecule to explain the continuous energy (band) formation in solids. Further details, see Refs. [22, Chapter 3][26, Chapter 3].

In **Figure. 2.4**, the formation of bands in a solid is illustrated using the concept of **LCAOs**, transitioning from isolated atomic system ($N = 1$) to a large number of atoms (solid). It starts illustrating the energy levels for a isolated atomic with three orbitals, which can be associated with the highest occupied and lowest unoccupied atomic orbitals, where each one can occupied with a maximum of two electrons taking into account the Pauli exclusion principle [27]. Then, by adding one atom ($N = 2$), the creation of the molecular orbitals would split the isolated energy levels into two for each corresponding orbital, as in the simplest hydrogen molecule. By adding one more atom ($N = 3$), this would result in six different possible **LCAOs**, producing only three distinguishable splitting energy levels. If this processes continue, adding consecutively one more atom ($N = 4, 5, 6, 7$) the energy levels would split (3, 4, 5, 6, 7) indistinguishable energy configuration, corresponding with all possible **LCAOs**. Finally, for a very larger number of atoms, the solid is formed, creating a continuo of energy states called bands. These band can be fully occupied (filled), partial occupied when there are aviable unoccupied state, and fully unoccupied (unfilled). Among all the formed bands, there are two main ones of interest, which are the valence band (**VB**) and the conduction band (**CB**), because they are primarily responsible for the electronic response of the material. **VB** is the highest band in a solid that is fully or partial occupied by electrons at absolute zero temperature. While **CB** is the lowest energy band in a solid that is fully unoccupied or empty at absolute zero.

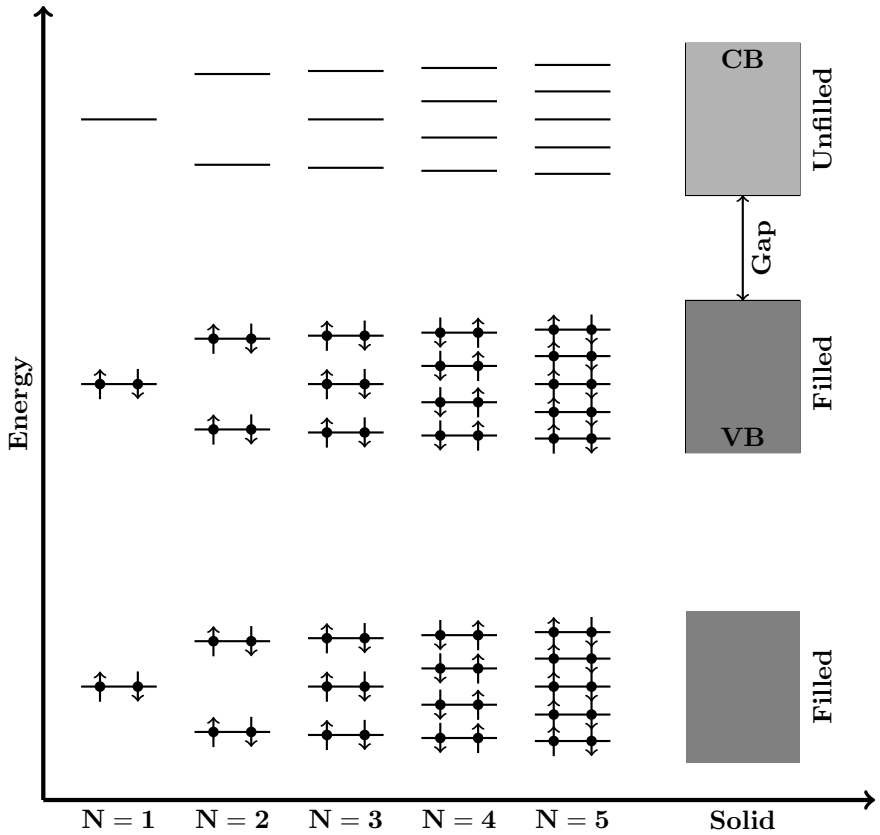


Figure 2.4: Illustration of band formation in solids through the **LCAOs** approach. The figure indicates the progression from an isolated atomic system ($N = 1$) to a large number of atoms (solid), showing the evolution of energy levels as two, three, four, five, and very large of atoms are brought together. It also represents the valence band (**VB**) and the conduction band (**CB**) in a solid.

Though in real crystals, the situation is more complex because the constituent atoms possess various orbitals ($\psi_{n,l,m}$), where n is the principal quantum number that determines the energy level ($(n = 1, 2, 3, \dots)$) and is associated with the size of the orbital. The quantum number l represents the orbital angular momentum ($(l = 0, 1, 2, \dots, n-1)$), which defines the shape of the orbital: $l = 0$ corresponds to s -orbitals, $l = 1$ to p -orbitals, $l = 2$ to d -orbitals, and $l = 3$ to f -orbitals. The magnetic quantum number m specifies the orientation of the orbital in space ($m = -l, \dots, 0, \dots, +l$). Them, the different **LCAOs** would become much more complicated because they must include interactions not only between the same orbitals, as in the hypothetical example used above, but also between distinct orbitals. Nevertheless, the underlying main idea explained earlier remains unchanged to explain bands formation in solid.

The theory of band structure in solids is extremely important for explaining the different electrical and thermal behaviors of materials. Therefore, the crystals are classified according to their band structure: conductors, semiconductors and insulators. In **Figure. 2.5**, the band structure for each of them is schematically represented. A conductor is a material with no gap between **VB** and **CB**, or where there exists a partially occupied **VB**. In both cases, electrons can be easily excited from the **VB** to the **CB** through an external electric field or by slightly increasing the temperature. While in a semiconductor and isolate material there is a gap between **VB** and **CB**,

which is defined as the energy gap E_g :

$$E_{gap} = E_{\text{CBM}} - E_{\text{VBM}}.$$

Here, E_{VBM} and E_{CBM} represents the valence band maximum (**VBM**) and the conduction band minimum (**CBM**), respectively. This E_{gap} causes that electrons cannot be easily excited using an electric field or by slightly increasing the temperature because there are no available states above the valence band (**VB**). Electrons would require additional energy equal to or greater than the energy band gap to jump to the conduction band (**CB**) in order to start moving freely and conduct electricity. Note: Historically, elements with a large band gap were considered insulators, while those with a small band gap were considered semiconductors. But most modern distinction between those are related with the conducting capacity (yes or not) under certain condition [22–24].

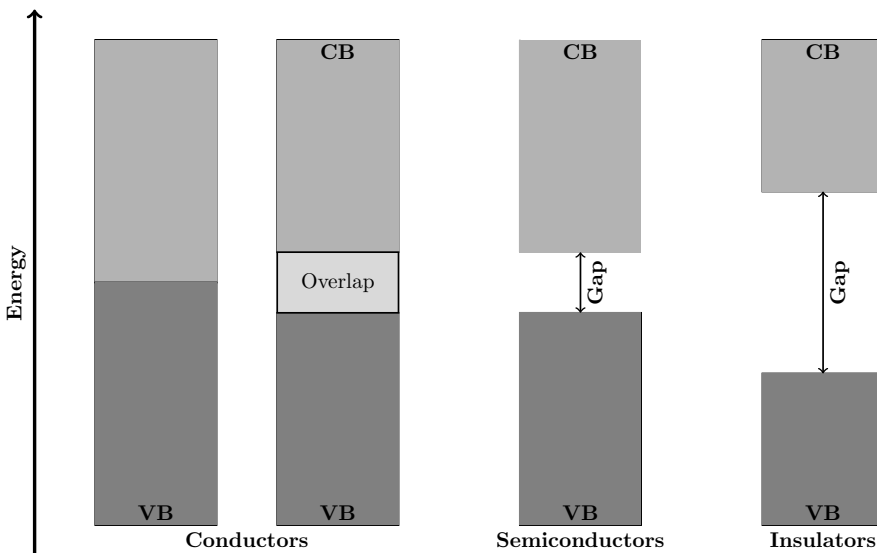


Figure 2.5: Classification of crystalline materials based on their band structure: conductors, semiconductors, and insulators.

2.3 Density of states (DOS) and Fermi-Dirac distribution

In this section, we will introduce the concept of the density of states (**DOS**) and its relation to the Fermi-Dirac distribution. This concept plays an important role in solid-state physics, allowing the calculation of quantities such as carrier concentration, which is an important parameter for technological applications in semiconductor materials.

To relate the last **Section 2.2** with **DOS** discussion, from the **Figure. 2.4** look like spacing between energy level is uniformed, which makes to expected that **DOS** would be ended up with a constant values. This was just an illustration because in the real crystal the different orbital would interact in distinct form, resulting **DOS** that is a function of energy.

Definition of DOS

The **DOS** describes the number of available states per unit energy range containing in the volume V

$$DOS(E) = \frac{g(E)}{V} \implies g = \frac{\Delta N}{\Delta E} = \frac{1}{\Delta E} \sum_i \delta(E - E(\mathbf{k}_i)) \quad (2.10)$$

or for continuos dispersion $g(E)$,

$$DOS(E) = \frac{g(E)}{V} \implies g(E) = \frac{\partial N(E)}{\partial E} \quad (2.11)$$

where $\Delta N = g(E)\Delta E$ is the number state in the energy range $E + \Delta E$ in the system with volume V

The **DOS Equs.** (2.10) and (2.11) essentially counting the number state in an energy interval. A very easy way to visualize it is through the simplest free electron problem in a box with periodic boundary condition equal to the box length L . Here, it would not discuss this approximation and just print out the resulting energy momentum dispersion. For further reading, see **Refs.** [20, Chapter 2][23, Chapter 6, 7][24, Chapter 6, 7]. It is given

$$E = \frac{\hbar^2 \mathbf{k}^2}{2m} = \frac{\hbar^2}{2m}(k_x^2 + k_y^2 + k_z^2) \implies k_i = n_i \frac{2\pi}{L}, i = x, y, z \quad (2.12)$$

where $\hbar\mathbf{k}$ is the electron momentum. In the figure **Figure.** 2.6 is schemed that relation dispersion, the red point. While, the black line shows continuos dispersion, when the dimension of the box is large enough ($L \rightarrow \infty$) that separation between state is indistinguishable. For a discrete case, it is possible to count directly the number state by moving the interval $E + \Delta E$ along of all energy range and multiplying by 2 (each energy level can be occupied by 2 electron), which is the numerical procedure **Equ.** (2.10). On the other hand, in the continuos is not able to count any longer the number state, therefore **Equ.** (2.10) would be transformed into an integral

$$g(E) = 2 \frac{V}{(2\pi)^3} \int d\mathbf{k} \delta(E - E(\mathbf{k})) \quad (2.13)$$

where $d\mathbf{k} = \frac{V}{(2\pi)^3}$ is an infinitesimal in the \mathbf{k} -space and $V = L^3$ is the volume of the box and the 2 comes again from the fact each state can be occupied for two electron [28, Chapter 2]. Then, replacing the relation dispersion **Equ.** (2.12) in to **Equ.** (2.13) and solving the integral, bring back to the variable E . It would find **DOS**²

$$g(E) = \frac{V}{2\pi^2} \left(\frac{2m}{\hbar^2} \right)^{3/2} E^{1/2} \implies DOS(E) = \frac{1}{2\pi^2} \left(\frac{2m}{\hbar^2} \right)^{3/2} E^{1/2}. \quad (2.14)$$

In semiconductor, the last result **Equ.** (2.14) is quite useful to make able to calculate the charged concentration under some consideration, it would bring back again in the next section (**Section 2.4**).

²For a complete proof of **DOS**, see **Refs.** [23, Chapter 6][26, Appemdix IV]

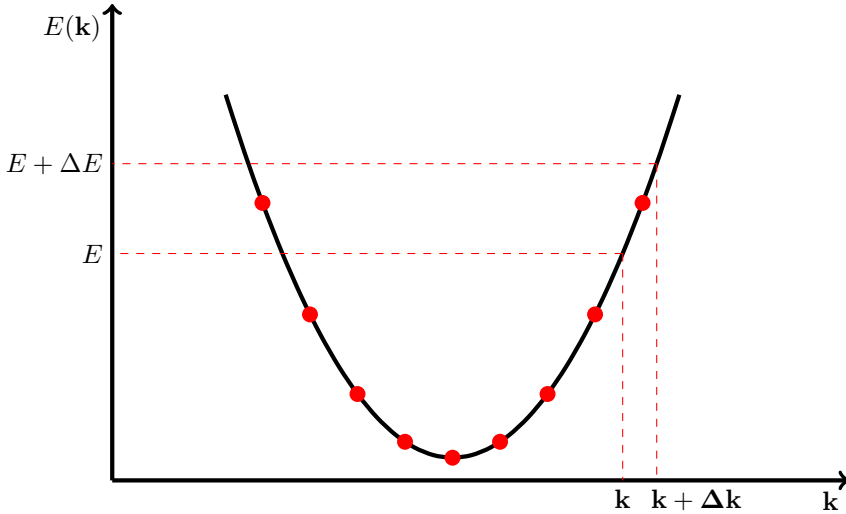


Figure 2.6: Energy dispersion for free electron problem in a big box, where for simplicity $\mathbf{k} = k_x$ and $k_y, k_z = 0$. This meaning moving only in the k_x direction

Fermi-Dirac distribution

In the later discussion, it would deal with the number of state or more precisely with **DOS**, but in any moment was mention how those states are populated. For simple intuition at zero temperature without any external potential is expected that all lower energies state would be occupied, filling from the lowest up to Fermi energy level (the highest occupied state at 0 [K]).

So now, what happened if the temperature increase?. If the temperature increase, the electrons can be excited to the next closer available energy level, leaving behind some vacant state or unoccupied. The problem now is how to accommodate those electrons at a finite temperature ($T > 0$) within a given number of available states. The solution is a classical problem in statistic mechanics, it is given by the so-called Fermi-Dirac probability distribution

$$f(E) = \frac{1}{e^{(E-\mu)/k_B T} + 1}. \quad (2.15)$$

The quantity μ is the chemical potential, which depends on the temperature. This parameter is chosen in a way that the total number of the electron have to be conserved to any temperature.

The Fermi-Dirac distribution **Equ.** (2.15) essentially gives the probability that one state with E is occupied for an electron at temperature T . At zero temperature, the Fermi-Dirac distribution has a discontinued behavior from value 1 occupied ($E < E_F$) to 0 unoccupied $E > E_F$ state, since $T \rightarrow 0 \implies E = \mu = E_F$, being E_F the Fermi energy. The last gives a more formal definition of E_F , it is the referent energy which has a probability $f(E_F) = \frac{1}{2}$ of being occupied at 0 [K]. Further reading and deduction **Refs.** [26, Appemdx V][29, 30].

These two piece together make able to calculate the electron concentration to any temperature in an interval of the energy $E + dE$, it needs to multiply the **DOS** by the probability of occupation of that state (Fermi-Dirac distribution)

$$dN = DOS(E)f(E)dE,$$

then the total electron concentration (charged concentration) can be calculated

$$N = \frac{1}{V} \int_{E_{lowest}}^{\infty} g(E) f(E) dE, \quad (2.16)$$

where E_{lowest} is the lowest available state. For instance, the **Equ.** (2.16) for the electron in a box result

$$N = \frac{1}{2\pi^2} \left(\frac{2m}{\hbar^2} \right)^{3/2} \int_{E_{lowest}}^{\infty} \frac{E^{1/2}}{e^{(E-\mu)/k_B T} + 1} dE. \quad (2.17)$$

2.4 Semiconductor materials

the **Section 2.2** is defined a semiconductor material. Here, it would explore in more detail some main interesting properties of the semiconductor. Exploring in more detail the band structure, charged concentration and doping properties.

2.4.1 Band structure

The electron energy would be dependent on the momenta of the electron, which is related directly to wavector \mathbf{k} as showed for a free electron in a big box **Section 2.3**. As expected in crystals, the energy dispersion relation is significantly more complex than in free-electron models.

Lucky, for semiconductors can be simplification under so-called parabolic approximation to further study electrical properties. The parabolic approximation essentially takes into account two fact. First fact, the electrons involve in excitation are those closer to the **VBM** and resulting excitation would be localized around the **CBM**. Second fact, for the majority semiconductor material the energy dispersion relation around **VMB** and **CBM** are commonly parabolic [20][26, Chapter 3].

In a semiconductor material are subdivide in two group due to band structure, direct and inderect ban gap semiconductor. Both are shown in the **Figure. 2.7**

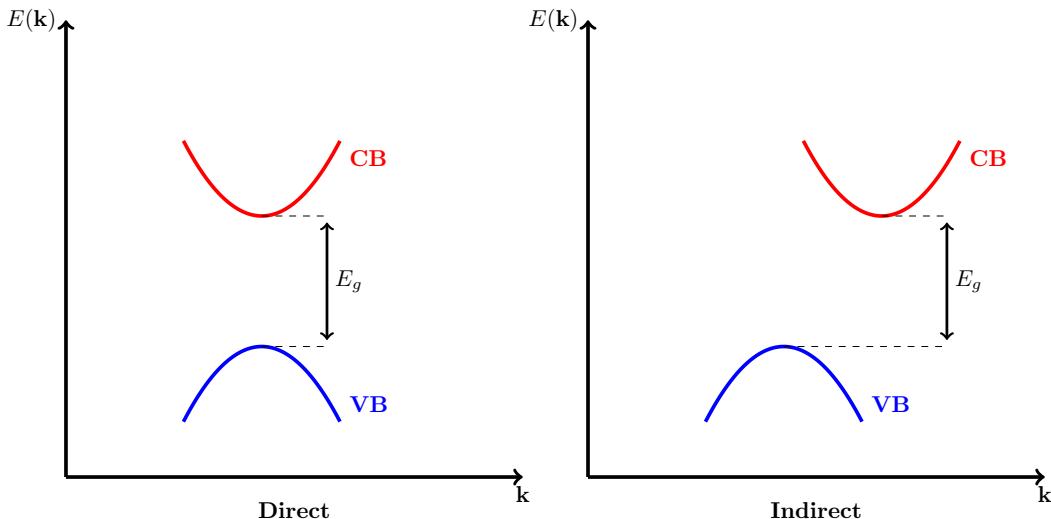


Figure 2.7: Schematic direct and indirect band gaps, from the fact that the **VBM** and **CBM** do not necessarily lie at the same wavector \mathbf{k} for all semiconductors.

A direct band gap semiconductors the **VBM** and the **CBM** lie at the same wavector \mathbf{k} , while indirect bad gap occurred to opposite, this distintion is relevanted for tecnological application. For instance, in a direct semiconductor, electrons can be excited directly from the **VB** to the **CB** by absorbing a photon with enought energy. In contrast, in an indirect semiconductor, this process must be assisted by a phonon interaction or may involve a more complex transition through defect-induced energy levels [20][23, Chapter 8][26, Chapter 3].

2.4.2 Intrinsic semiconductors and charge concentration

As has been mentioned, the electron distribution in the different available state would be depended on the temperature, more extrinsic of **DOS** and Fermi-Direct distribution. Under parabolic approximation, the result for the electron in a big box can be applied to find the charge concentration.

Before that, it is needed to define a new concept (**hole**). A **hole** as the name indicate is the hold that left an electron when is excited from **VM** to **CB**, see the red color in **VB** in the **Figure. 2.8**. The reason this concept is introduced is simple: it is easier to deal with the **hole** as an electron with a positive charge than with all the remaining electrons in the **VB** [23, 24].

Following with discussion, the energy dispersion within a parabolic approximation can be written for both **VB** and **CB**

$$E(\mathbf{k}) = E_0 + \frac{\hbar^2 \mathbf{k}^2}{2m^*}, \quad (2.18)$$

E_0 is a reference energy for **VBM** and **CBM**, and m^* is the effective mass. It can be defined using a semiclassical approximation over the **Equ. (2.18)** applying Newton Law

$$m^* = \hbar^2 \left(\frac{\partial^2 E(\mathbf{k})}{\partial k_i^2} \right)^{-1} \quad (2.19)$$

where k_i references to different crystallographic direction k_x, k_y, k_z . The definition of effective mass **Equ. (2.19)** either for hold m_h^* or electron m_e^* would depend on the curvature of the parabola for hole and electron, and each semiconductor material would have its own values for it in different crystallography direction ³[23]. An interesting thing to mention, this definition left a negative masses for the hole, which is the reason that they can be tried as electron with a positive charged.

³The effective mass can be physically interpreted as the apparent mass holes and electrons in a crystal, due to their interactions with the surrounding ions.

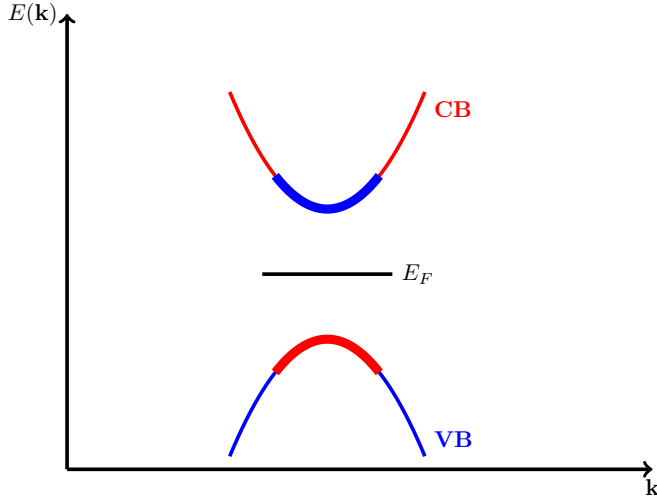


Figure 2.8: Illustration electron distribution in intrinsic semiconductor at temperature $T > 0$

Putting all these pieces together, the charged concentrations (**Equ.** (2.16)) holes (p) and electrons (n) in an intrinsic semiconductor can be written

$$p = \int_{-\infty}^{E_{\text{VBM}}} \text{DOS}(E) f_h(E) dE = \int_{-\infty}^{E_{\text{VBM}}} \text{DOS}(E) [1 - f(E)] dE, \quad (2.20)$$

$$n = \int_{E_{\text{CBM}}}^{\infty} \text{DOS}(E) f_e(E) dE = \int_{E_{\text{CBM}}}^{\infty} \text{DOS}(E) f(E) dE. \quad (2.21)$$

Being $f_h(E)$ and $f_e(E)$ the probability distribution for holes and electron respectively. If **Equs.** (2.20) and (2.4.2) are printed out the **DOS** and Fermi-Dirac distribution the resulting equation would not have analytic solution (**Equ.** (2.17)). Instead for intrinsic semiconductor a good approximation is done considering temperatures condition with a few $k_B T$ below the **VBM**

$$E - \mu \gg k_B T \implies f_h(E) = f_e(E) \approx e^{(E-\mu)/k_B T},$$

the resulting charge concentrations after solving the integrals are ⁴

$$n = N_e^{\text{eff}} e^{-(E_{\text{gap}} - \mu)/k_B T} \implies N_e^{\text{eff}} = \frac{1}{\sqrt{2}} \left(\frac{m_e^* k_B T}{\pi \hbar^2} \right)^{3/2} \quad (2.22)$$

and

$$p = N_h^{\text{eff}} e^{-\mu/k_B T} \implies N_h^{\text{eff}} = \frac{1}{\sqrt{2}} \left(\frac{m_h^* k_B T}{\pi \hbar^2} \right)^{3/2}. \quad (2.23)$$

2.4.3 Doping

The success of semiconductors is related to the flexibility in the high control of electrical properties. One of the most interesting techniques is doping. The doping effect is created by introducing the right impurities into the perfect crystal. These impurities introduce energy levels inside the gap close enough to the **VBM** or **CBM**, in such a way that they can be ionized with a few ($k_B T$) of energy by trapping an electron from

⁴For further details, see **Refs.** [23, 24, 28]

the valence band **VB** (acceptor), or donating an electron to the conduction band **CB** (donor), respectively. Those two concepts left **n-type** (acceptor) and **p-type** (donor) semiconductors.

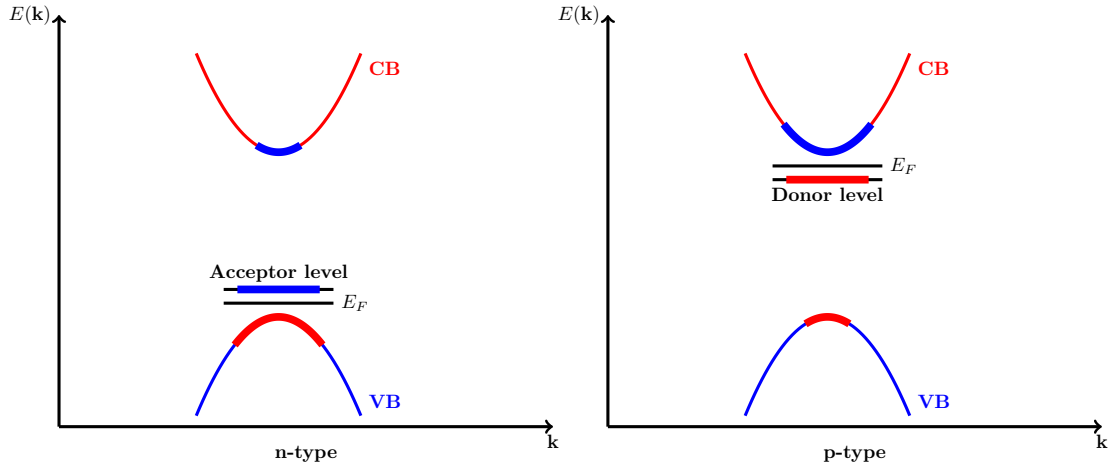


Figure 2.9: Illustration of **n-type** and **p-type** semiconductor at temperature $T > 0$

In the **Figure. 2.9** is schemed for both type of semiconductor at $T > 0$. As shown there, acceptor and donor states introduce an except of charge concentration holes and electron, respectively. For a doped defect, it illustrates the fermi level (chemical potential) shift from the middle of the gap **Figures. 2.8** and **2.9** in a way to conserve the charge total concentration and $T = 0$ [K] the probability to find a occupied stated there has to be 50%.

When a semiconductor is in thermal equilibrium, it is charged neutral. That can be expressed as a simple relation called charge neutralization condition,

$$p + N_d^+ = n + N_a^- \quad (2.24)$$

where the two new terms N_d and N_a are the donor and acceptor concentration, respectively.

2.5 Point defects in semiconductor materials

In real material the crystalline structure would not be perfect, specially when is increasing the temperature different imperfection could be appeared or introduce as the case doped semiconductors. Those imperfections can be divided into classes according to their dimensionality as: zero (point), one (linear), two (plane) and three (volume) dimensional defects. Each one has their own properties and consideration, thought the two last normally are considered an extension of the point and linear defect. Here, it would just discuss point defect which is the main interesting for this thesis. For further discussion, see **Refs. [20, 31, 32]**.

A point defect is a localized imperfection in a crystal, involving one or a few atoms, that alters the local arrangement without disrupting the overall long-range order of the material, it is illustrated with shaded circule in the **Figure. 2.10**. There is also schemed different point defects in a crystal with two composition elements A(blue) and B(red), the levels **1-4a** represent the simplest point defects, while the other two **1-2b** are complex

point defect. A complex point defect in general is any point defect that contain more than one simplest point defect.

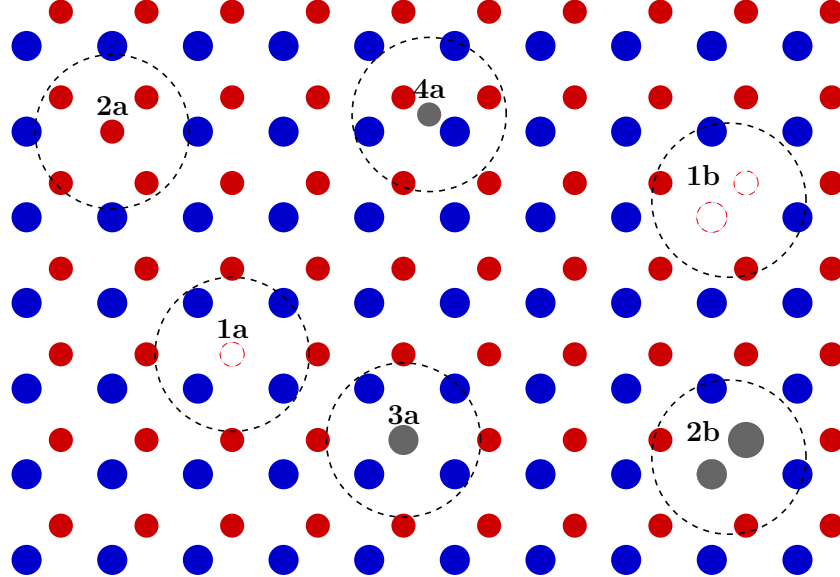


Figure 2.10: Illustration of different types of point defects in a binary material. Those labels with **(a)** are simples point defects, **(b)** are two example of complex defects

The **1a** is named vacancy defect (V_B), it originates by removing a one of the atoms from host material. **2a** is called antisite defect (B_A), it originates substituting one of the two specimen in the correspondent site of the other one. Then, **3a** is a substitutional defect (X_B), it originates including different elements (X) from the compound host martial (impurities). Finally, **4a** is an interstitial defect (X_i), creating by introducing an impurity or moving out the compound elements from correspondent position. To creat **1b** and **2b**, it just need to combine two of the after mention

$$V_A + V_B \leftrightarrow V_A V_B \quad X_A + Y_B \leftrightarrow X_A Y_B .$$

X and Y could represent any impurity elements.

2.5.1 Point defect concentration

As later was mention, when the temperature is increased some direct appear (intrinsic). The concentration of those can be calculated using statistic thermodynamic, it is determined by minimization of the Gibbs free energy change due to addition of the defect, ΔG [33, 34]. For an arrangement of N number of atoms belonging to each lattice point and n_d number of defects, ΔG is defined ⁵

$$\Delta G = n_d \Delta H - T \Delta S = n_d \Delta H - T(n_d \Delta S_{vib} + \Delta S_{conf}) , \quad (2.25)$$

where ΔH the enthalpy formation energy. ΔS the change in the entropy, it can be split in two part, ΔS_{vib} is the entropy terms due to the vibration of the atoms around the each defects and ΔS_{conf} is the configurational entropy related with how many ways to

⁵Further details [29, 30, 33, 34]

arrangement n_d in the $N + n_d$ available site [20, Chapter 7][32, Chapter 2]. This last is defined

$$\Delta S_{conf} = k_B \ln(\Omega) = k_B \ln \left[\frac{(N + n_d)!}{N! n_d!} \right], \quad (2.26)$$

for $n_d \ll N$ the (2.26) using the Stirling's approximation [29], it can be rewritten

$$\Delta S_{conf} \approx k_B [(N + n_d) \ln(N + n_d) - N \ln(N) - n_d \ln(n_d)].$$

Minimizing the Gibbs free energy (2.25) with respect to the number of defects n_d , resulting in

$$\frac{\partial \Delta G}{\partial n_d} = \Delta H - TS_{vib} - k_B T \ln \left[\frac{N + n_d}{n_d} \right] = 0, \quad (2.27)$$

solving for n_d in the (2.27), the defect concentration at temperature T is given

$$\frac{n_d}{N + n_d} = e^{\Delta S_{vib}/k_B T} e^{-\Delta H/k_B T}. \quad (2.28)$$

A interesting point to stant out, if in the equation **Equ.** (2.28) is not considered change in the pressure or volume and no high temperature (no phonon vibration), it can be rewritten

$$\frac{n_d}{N + n_d} = e^{-E^f/k_B T} \quad (2.29)$$

where E^f is the formation energy, which can be estimated directly from first-principles calculations under the assumption of low temperature. This implies that E^f can be approximated by the total energy result from **DFT** at $T = 0$ [K]. See further details in **Section 5.2**.

2.5.2 Impact of point defects on semiconductor properties

Point defects can be changed electronic properties of the semiconductor, particularly with high concentration. Normally, point defect introduce energy level inside the band gap (doping) which ones can due to unpairing atomic orbitals related with the defect [20, Chapter 7]. Either way, those state can be divided in shallow and deep levels. Shallow level is an introduce energy finding close to band gap edges **VB** and **CB**, they are commonly preferred or selected to create doping semiconductor discussed before. On the other hand, deep level generally are deeper in the band "far way" from gap ages, which less resonance with the **VB** and **CB** leaving a perfect candidate for robust **QT** application, especially when they are very well localized. In the **Figure. 2.11** are both illustated

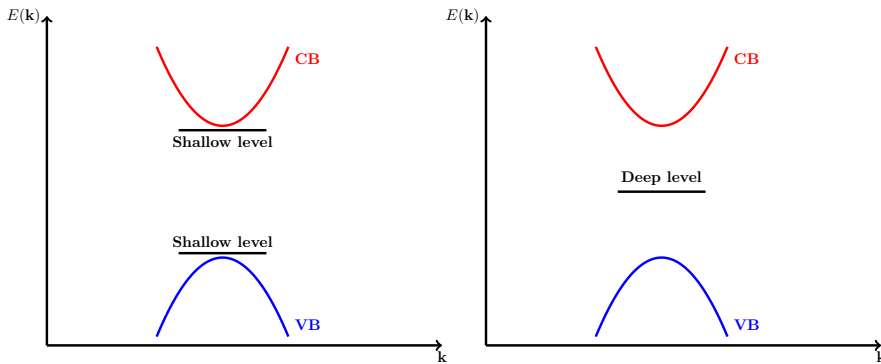


Figure 2.11: Illustration of a shallow and deep defect leves in semiconductors.

Point defect can exist in different charge, positive (+1, +2, +3, ...) gives up electrons to the **CB** (donor defects), and negative (-1, -2, -3, ...) trapping electrons from **VB** (acceptor defects). The ionization energies for each charge condition would be different, therefore each charge energy levels have different location in the gap. This behavior essentially results from distinct reconfiguration due to the loss or gain electrons [20, Chapter 7][34].

2.5.3 Defect application in quantum technology (QT)

As was mention, the **QT** have been one of the most study topic in the recently ages, showing notable advances that are promising in relation to current technologies. For **QT** essentially is understood as any quantum system that is possible to used in technological application, in which it has to be possible to control, manipulate and read out quantum effect, those quantum effects can be entanglement, superposition, and tunneling among others. This is a large and growing field that including as main areas **QC**, communication and sensing [1–5].

There are different platforms to create the suitable condition for **QT**, superconducting material, quantum well, trapped ions, photonic systems and point defects. Unfortunately, they all shared a common problem related with the coherence of the quantum system, it is related with the superposition condition when is destroyed then the quantum state disappear. This is related with any interaction of the quantum system with the surrounding environment that makes collapse the superposition state. Temperature may act as an initiator of these interaction phenomena; therefore, it is necessary to lower the temperature close to 0 [K] to sustain it, as in the case of superconducting qubits [35]. Here, no further discussion will be provided on the various platforms, except for point defects.

Deep defect levels have been shown a great advances to achieve suitable condition for **QT** application, since it have been proved long coherent time and high robust to make able to control, manipulate and read out quantum information. These behaviors come from those states can be considered as isolated state inside of crystal, specially when they are very well localized giving particular properties. In additionally, point defects have an easier scalability in semiconductor and higher controlling temperature than other platforms [18, 36]. A clear example is vacancy defect in diamond that has been found as spin qubit, single photon emitter and quantum sensing [11, 12, 37].

An ideal quantum system based on a point defect can be illustrated in **Figure. 2.12**. It consists of a two-level quantum system $|0\rangle$ and $|1\rangle$, which can be controlled and manipulated using photons. This may be initialized by hitting a photon, resulting in a quantum superposition state $|\psi\rangle = \alpha|0\rangle + \beta|1\rangle$. After, the states can be read out via photon emission (corresponding to $|0\rangle$) or no emission (corresponding to $|1\rangle$). If the photons emitted from the point defect are temporally separated, individually detectable with some time delay, and indistinguishable in frequency, the system functions as a single photon source (**SPS**) or emitter (**SPE**). Note: Real point defect in crystal would end up with bit more complex schemes but the main idea is mantained [11, 12].

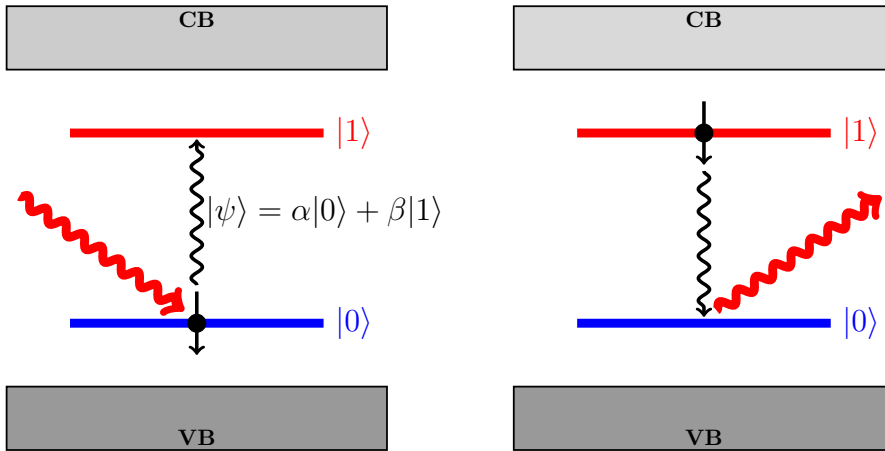


Figure 2.12: Illustration desired two-level quantum system in deep defect levels

In ordering to satisfy those condition, the transition should be considered under spin conservation since directly the electron can be excited (initialization) by hitting with photon. Thought, it would also need less possible external interaction with phonon or surrounding environment, which experimentally can measure by the very distinguishable sharp peak at zero phonon line **ZPL** in the the photoluminescence (**PL**) experiments.

2.6 Wurtzite Aluminum Nitride (w-AlN)

The w-AlN is a semiconductor material with a hexagonal Wurtzite crystal structure where each atom is bonded to 4 nearest neighbors in a tetrahedral geometry. It has been used for different technological application in the last decade, filter communication, sensor, ultrasonic, and optoelectronics devises among others [19, 38, 39].

In the last years, it has been explored as a new point defect platform material for **QT**. It has a wideband gap which makes suitable to isolate deep defect levels, while they could be controlled, initialized and read out optically. Moreover, in w-AlN have been measure **PSE** at room temperature, which gives a promising characteristic for the future technologies [14–17]. Here, the main objective would be explored different defect that may be compatible with **QT**, identifying or fitting potential **SPE** and spin qubit center.

2.6.1 Crystal structure and bulk properties of w-AlN

The w-AlN crystal structure is composed of 4 atoms, 2 Al and 2 N. They are distributed in a repeatedly 2 stacked Al-N bilayer AB, see in the **Figure. 2.13**. It also shows the primitive hexagonal lattice structure with respective lattice parameters $a = b = 3.110$ [Å] and $c = 4.980$ [Å] [40, 41], where the light gray are N and dark gray are Al toms. This matiral has a direct wide band gap 6.20 [eV] which makes poor conductor in its pure form [42]. Futher detail of the electrical propeties are all given in the **Chapter 6**.

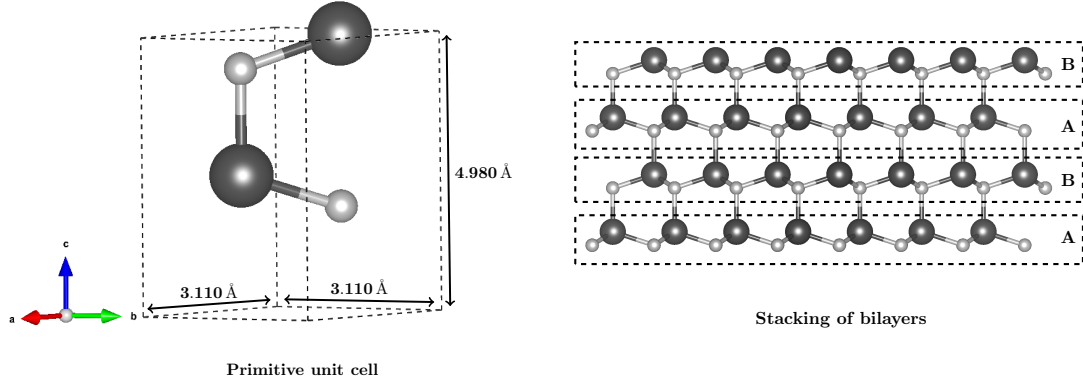


Figure 2.13: w-AlN primitive unit cell and stacing AB bilayers

The first **BZ** for a hexagonal lattice structure result in the same hexagonal symmetric as show in the **Figure. 2.14**. This also shows the path over the higher-symmetric points, where each point corresponds a position in the reciprocal space, $\Gamma = (0, 0, 0)$ which coincides with the **VBM** and **CBM** in w-AlN, $A = (0, 0, 1/2)$, $L = (1/2, 0, 1/2)$, $M = (1/2, 0, 0)$, $K = (2/3, 1/3, 0)$, $H = (2/3, 1/3, 1/2)$ [23].

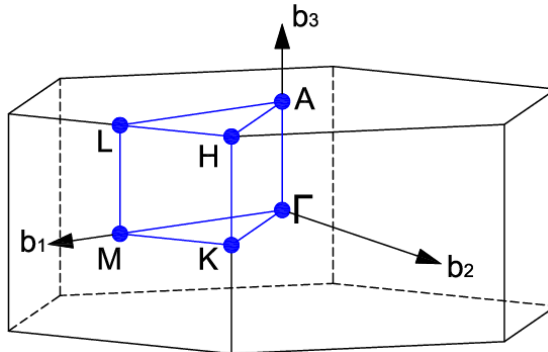


Figure 2.14: The first **BZ** for hexagonal structure and the higher-symmetric points Γ , A , L , M , K , and H

2.6.2 Defects in w-AlN as candidates for QT

Defect exploring select defects are chosen under under criterios: practicality, based on literature and comparison. Practically, some of these defects may appear by increasing the temperature (intrinsic defects). Based on literature, some have already been studied using first-principles methods and were identified as promising candidates for **QT**. Comparison with known defects in materials such as diamond and silicon, which exhibit desired properties like spin qubits and single-photon emission. In the **Figure. 2.15** is illustrated the select point defects, which are three native defects V_N , V_{Al} and Al_N , one impurity defect C_N , and two complex defects $V_{Al}V_N$, and $C_N C_{Al}$.

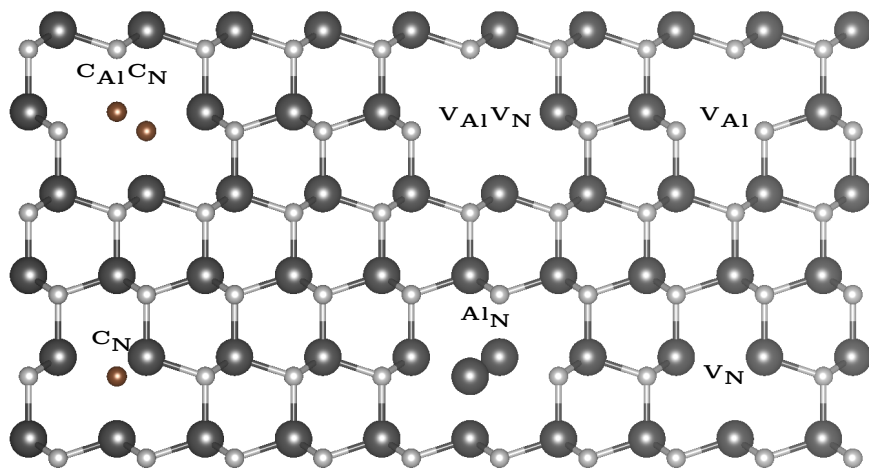


Figure 2.15: Illustration of the different selected point defects: V_N , V_{Al} , Al_N , C_N , $V_{Al}V_N$, and $C_{Al}C_N$

Further discussion on their properties such as: thermodynamic stable and transition charge states, single electron orbital localization, and details of some charged defect that may be compatible to used in **QT**. They are all given in the **Section 6.3**.

Chapter 3

Many-Body Quantum Mechanics in Crystalline Systems

In this chapter, it will be discussed the general Schrödinger equation (**SE**) and why the **SE** is needed, also some ideas of the “simplest” version in case of one particle. Then it will be a general description of periodic potential related with Bloch theorem. After, dealing with many-body particle **SE**. The last starts with a general description of the many-particle **SE**, goes on to explain some important considerations. The following parts are a way to approximate the many-particle **SE** to find a solution, by using the Born-Oppenheimer approximation (**BOA**), then describing the general variational principle. Finally, it discusses some of the most general approaches to finding a solution to the **SE**, that is, the Hartree and Hartree-Fock approximations, and the Density Functional Theory (**DFT**), which is the main method used in this thesis work. Additionally, the Many-body perturbation theory (**MBPT**) and Green’s function theory (**GFT**) methods are briefly discussed.

3.1 Schrödinger equation

Before quantum mechanics was developed, all explanations of natural phenomena were made in the context of classical mechanics. The latter made good predictions of macroscopic systems, such as the car in motion, by being able to predict the exact position and velocity of the car just by knowing the initial conditions.

On the other hand, classical mechanics failed, or more correctly, became insufficient to explain the microscopic behavior of matter, like atoms, molecules, nanocrystals and so on. Either way, it highlights an important point and perhaps the most significant aspect of classical mechanics: “*the least-action principle*” and the conservation laws derived from it, for more information see Goldstein [43]. Starting from these ideas and knowing the theory of wave behavior of matter from Louis de Broglie [44], Erwin Schrödinger published his wave theory of particles, introducing his famous “*Schrödinger equation*”¹, along with the interpretation of the norm of the wave function as a probability density, laying the foundations of a new physics: Quantum physics [48, 49].

The wave theory made possible the explanation of microscopic phenomena and their so-called quantized energy levels. One example is the quantized atomic state, see book

¹The **SE** was not the only formulation of quantum mechanics. Around the same time, Werner Heisenberg introduced his own formalism of quantum mechanics [45]. Later, the equivalence between these two approaches was established, and they became known as the Schrödinger and Heisenberg pictures. For further details, see [46, 47].

by Griffiths for further information [27]. However, it was not completed and in general speaking is called “*non relativistic Schrödinger equation*” since that does not include the relativistic effects of particles in motion. It was not until Klein-Gordon and Dirac equation, where one could finally put together quantum mechanics and special relativity [50, 51]. Moreover, Dirac generalized the **SE** by introducing the so-called **bra-ket** formalism², which will be used extensively in some parts of this thesis to take advantage of its compact notation. For further reading, see Sakurai Ref. [47].

The non-relativistic time-dependent **SE** in the coordinate representation is defined as

$$\hat{H}\Psi(\mathbf{r}, t) = i\hbar \frac{\partial\Psi(\mathbf{r}, t)}{\partial t}, \quad (3.1)$$

where \hat{H} is the Hamiltonian of the system, Ψ is the total wavefunction which contains all the information about the system [27, 47], i is the imaginary unit, \hbar is the reduced Planck constant, and t is time. It should be taken into account in this description that \hat{H} is an operator which represents the energy of the system, and the wavefunction is interpreted as a “*probability density*” — more precisely the wavefunction norm. For a complete deduction of the **SE** and further reading about operator and wavefunction interpretation, see Refs. [53, Chapter 1][27, 46, 47].

From **Equ.** (3.1), it is possible to find a time-independent version of the **SE** if we assume that the Hamiltonian does not depend on time explicitly. Then, the wavefunction can be expressed as a product of two parts: one dependent on the position and the other on time,

$$\Psi_\nu(\mathbf{r}, t) = \psi_\nu(\mathbf{r})\phi_\nu(t),$$

where ν symbolizes any discretization number. One example is the solution for the Hydrogen atom $\psi_{n,l,m}(\mathbf{r})$ where n, l, s represent ν [27]. Eventually we arrive to

$$\hat{H}\psi_\nu(\mathbf{r}) = E_\nu\psi_\nu(\mathbf{r}), \quad (3.2)$$

$$i\hbar \frac{\partial\phi_\nu(t)}{\partial t} = E_\nu\phi_\nu(t), \quad (3.3)$$

where the solution of **Equ.** (3.2) will be dependent on the Hamiltonian of the system, which could be quite complex, see **Section 3.3** where they take into account many-body interactions. On the other hand, **Equ.** (3.3) has a general solution

$$\phi_\nu(t) = e^{-iE_\nu t/\hbar}.$$

Then, the total solution of the wavefunction can be written as

$$\Psi_\nu(\mathbf{r}, t) = \sum_\nu c_\nu \psi_\nu(\mathbf{r})\phi_\nu(t) = \sum_\nu c_\nu \psi_\nu(\mathbf{r})e^{-iE_\nu t/\hbar}, \quad (3.4)$$

where c_ν is a constant which is found by the normalization condition of the wavefunction [27, 47].

²Within this generalization lies the so-called interaction picture, which represents a mixture of the Schrödinger and Heisenberg formulations and is more suitable for working with time-dependent perturbation **SE** [46, 47]. Furthermore, there are currently several more general approaches to quantum mechanics, with one of the most famous being Richard Feynman’s path integral formulation [47, 52].

3.2 Periodic potential and Bloch theorem

In the **Chapter 2** is introduced the basis ideas of crystalline system, it was mentioned and maybe the most important thing in these systems is their arrangement ordered. This simplified the mathematical treatment considerably and made possible a physical understanding of the microscopic behavior of the system. One very important property that left in a crystal the potential energy must be periodic, which implies that the Hamiltonian must be periodic as well, with the periodicity of the lattice \mathbf{R} . see **Equ.** (2.1).

Supposing it applies a translation operation $\hat{T}_{\mathbf{R}}$ to the crystalline system, by periodicity properties of Hamiltonian

$$\hat{T}_{\mathbf{R}} \hat{H}(\mathbf{r}) \Psi(\mathbf{r}) = E \Psi(\mathbf{r}) = \hat{H}(\mathbf{r} + \mathbf{R}) \Psi(\mathbf{r} + \mathbf{R}) = \hat{H}(\mathbf{r}) \hat{T}_{\mathbf{R}} \Psi(\mathbf{r}). \quad (3.5)$$

The result from the **Equ.** (3.5) meaning that $\hat{T}_{\mathbf{R}}$ commute with \hat{H} which means that they can be expanded in the same bases [22, 27], resulting in

$$\begin{aligned} \hat{H} \Psi(\mathbf{r}) &= E \Psi(\mathbf{r}) \\ \hat{T}_{\mathbf{R}} \Psi(\mathbf{r}) &= C(\mathbf{R}) \Psi(\mathbf{r}) \end{aligned} \quad (3.6)$$

where $C(\mathbf{R})$ has to be some constant which will depend on applied translation \mathbf{R} . Again due to the periodic conditions of the potential energy make electronic density of the system $n(\mathbf{r}) = \|\Psi(\mathbf{r})\|^2$ period,

$$\hat{T}_{\mathbf{R}} n(\mathbf{r}) = \|C(\mathbf{R})\|^2 n(\mathbf{r}) \implies \|C(\mathbf{R})\|^2 = 1 \quad (3.7)$$

in view to satisfy **Equ.** (3.7), it can be proved that $C(\mathbf{R})$ is given

$$C(\mathbf{R}) = e^{i\mathbf{k}\cdot\mathbf{R}} \quad (3.8)$$

where \mathbf{k} is a real wave vector [22]. It is proportional to the electron momentum when referenced to the electronic part in the solid. Then the wavefunction can be rewritten

$$\Psi(\mathbf{r} + \mathbf{R}) = e^{i\mathbf{k}\cdot\mathbf{R}} \Psi(\mathbf{r}), \quad (3.9)$$

multiplying $e^{-i\mathbf{k}\cdot(\mathbf{r}+\mathbf{R})}$ both sides **Equ.** (3.9),

$$e^{-i\mathbf{k}\cdot(\mathbf{r}+\mathbf{R})} \Psi(\mathbf{r} + \mathbf{R}) = e^{-i\mathbf{k}\cdot\mathbf{r}} \Psi(\mathbf{r}) = u_{\mathbf{k}}(\mathbf{r}) = u_{\mathbf{k}}(\mathbf{r} + \mathbf{R}) \quad (3.10)$$

where is defined $u_{\mathbf{k}}(\mathbf{r})$ which has the lattice periodicity. Finally, rearranging the **Equ.** (3.10) result in the common form of the Bloch theorem ³

$$\Psi_{\mathbf{k}}(\mathbf{r}) = e^{i\mathbf{k}\cdot\mathbf{r}} u_{\mathbf{k}}(\mathbf{r}). \quad (3.11)$$

The very powerful and very interesting thing of the result in the **Equ.** (3.11) to determine the wavefunction it would just need to find $u_{\mathbf{k}}(\mathbf{r})$ in a determinate region (primitive unit cell) instead of the full crystal and then mapping into the full crystal multiply by the corresponding plane wave $e^{-i\mathbf{k}\cdot\mathbf{r}}$ phase. Note: The last statement is “shifted” in **DFT** to the select cell, it can be referred to the supercell approach when dealing with point defect. Further discussion supercell approach related with DFT **Section 4.1**.

³The **Equ.** (3.11) is equivalent to **Equ.** (3.9) is just a more fancy and practical way to write it. They are called Bloch functions.

3.3 Many-particle Schrödinger equation

In solid materials, to make us able to calculate bulk properties, it is necessary to deal with the many-body **SE**, where the Hamiltonian includes different interactions and kinetic energies for both electrons and nuclei.

The many-body time-independent **SE** takes the same form as **Equ.** (3.2), i.e.

$$\hat{H}_{en} \Psi_{\nu}^{en}(\mathbf{r}, \mathbf{R}) = E_{\nu}^{en} \Psi_{\nu}^{en}(\mathbf{r}, \mathbf{R}). \quad (3.12)$$

Here, e and n refer to electrons and nuclei, respectively, \hat{H}_{en} is the total Hamiltonian which contains all the interactions and kinetic energies of the system, the many-particle wavefunction $\Psi_{\nu}^{en}(\mathbf{r}, \mathbf{R}) \equiv \Psi_{\nu}^{en}(\mathbf{r}_1, \mathbf{r}_2, \dots, \mathbf{r}_{N_e}, \mathbf{R}_1, \mathbf{R}_2, \dots, \mathbf{R}_j, \dots, \mathbf{R}_{N_n})$ which depends on the position of all electrons (\mathbf{r}_j) and nuclei (\mathbf{R}_j), and E_{ν}^{en} is the total energy for both electrons and nuclei.

If we from **Equ.** (3.12) print explicitly all terms for the Hamiltonian, we get

$$\begin{aligned} \hat{H}_{en} &= \hat{T}_e + \hat{T}_n + \hat{V}_{ee} + \hat{V}_{nn} + \hat{V}_{en} \\ &= - \sum_j^{N_e} \frac{\hbar^2}{2m_e} \nabla_j^2 - \sum_{\alpha}^{N_n} \frac{\hbar^2}{2M_{\alpha}} \nabla_{\alpha}^2 \\ &\quad + \frac{1}{4\pi\epsilon_0} \sum_{j < j'}^{N_e} \frac{q^2}{\|\mathbf{r}_j - \mathbf{r}_{j'}\|} + \frac{1}{4\pi\epsilon_0} \sum_{\alpha < \alpha'}^{N_n} \frac{q^2 Z_{\alpha} Z_{\alpha'}}{\|\mathbf{R}_{\alpha} - \mathbf{R}_{\alpha'}\|} - \frac{1}{4\pi\epsilon_0} \sum_{j, \alpha}^{N_e, N_n} \frac{q^2 Z_{\alpha}}{\|\mathbf{r}_j - \mathbf{R}_{\alpha}\|}, \end{aligned} \quad (3.13)$$

where \hat{T}_e is the sum of the kinetic energies of the j^{th} up to the number of electrons N_e , and \hat{T}_n is the sum of the total of the α^{th} up to the number of nuclei N_n . The last tree terms are the Coulomb interaction. The first is the sum with respect to electron-electron interactions, the second is the nucleus-nucleus interaction, and the third is the sum with respect to electron-nucleus interactions. In the first and second Coulomb terms, there is a constraint in the sum $j < j'$ and $\alpha < \alpha'$. This is a way to avoid self-interaction, which means that the electrons and cores cannot interact with themselves ($j \neq j'$ and $\alpha \neq \alpha'$), but as well to fix interaction terms so that they are not counted twice. Z_{α} is the atomic number of the α^{th} nucleus with charge q .

The Hamiltonian looks quite complicated **Equ.** (3.13), meaning that **Equ.** (3.12) has no trivial solution. For a few problems it is possible to find a solution when the number of electrons and nuclei are typically smaller than four [54, Chater 4]. One example is the Helium atom and its isoelectronic ions [55]. The principal problem comes by growing dimensionally (D_{term}) of the system. $D_{\text{term}} = 3(N_e + N_n)$, which are coupled non-linear differential equations. For more complexity the interaction term (C_{term}) between electron-electron, core-core and electron-core is also growing fast, $C_{\text{term}} = \frac{N(N-1)}{2}$, and the correlation term of the wavefunction turns out to be highly complex as well and difficult to model. To solve the **SE** in such a complex and high-dimensional space becomes exponentially more complex. This is a big general problem in modeling of differential equations, the so-called “curse of dimensionality”, see Ref. [56] for overview.

Because of these complications, it becomes necessary to make some approximations when dealing with the many-particle **SE**. One of the most commonly used is the **BOA** which leaves a better stating point to be able to find a solution. However, this alone is not enough to solve “realistic” problems. Normally it is required to make more approximations, for example Hartree and Hartree-Fock approximations, **FCI**, **MBPT** and **GFT**. One of the most widely used is **DFT** which will be mainly used in this thesis.

3.4 Born-Oppenheimer approximation (BOA)

In the many-particle **SE** (Section 3.3) was discussed difficult to dealing it. The most commonly approximation used as first step to try to make easier to find a solution is the **BOA**. The **BOA** assumed that the wave functions of electrons and nuclei can be treated separately, the reason is the nucleus are much heavier than electron. For instance, the mass of one proton is $m_p/m_e \approx 1833$ times bigger than electron, this mass difference make nucleus move much slower than electrons [57]. It can be interpreted that electron respond is “instantaneous” with respect to change in the position of the nucleus, this make sense to separate the dynamic of the total wavefunction $\Psi_\nu^{en}(\mathbf{r}, \mathbf{R}) = \Psi_\nu^e(\mathbf{r}, \mathbf{R})\Phi_\nu^n(\mathbf{R})$ but taking into account the electronic wave function will depend on the nucleus position as parametric term [22, Section 2.5].

Within **BOA** nucleus are assumed at fixed in determined position, while the electron move around them feeling their electrostatic potential due to the nuclei configuration and the interaction with other electrons, see further explanation which use as example the Hydrogen molecule [25, Chapter 10]. It leads to a Hamiltonian for the electrons in the field generated by a static configuration of nuclei; On the other hand, leaves a nuclei Hamiltonian which depend on the average energy in regard to the electrons and nucleus interaction [58, Section 2.1.2]. Another important consideration in this procedure is the nucleus Hamiltonian can be treated as a classical description [54, Section 4.2]. It is also a normal assumption in many algorithms, like the case of *The Vienna Ab initio Simulation Package (VASP)*.

The Hamiltonian **Equ.** (3.13) can be written using the **BOA**, as sum of electronic plus nuclei part $\hat{H}_{en} = \hat{H}_e + \hat{H}_n$, where the **SE** for the \hat{H}_e part becomes

$$\left\{ \hat{T}_e + \hat{V}_{ee} + \hat{V}_{en} \right\} \Psi_\nu^e(\mathbf{r}, \mathbf{R}) = E_\nu(\mathbf{R}) \Psi_\nu^e(\mathbf{r}, \mathbf{R}), \quad (3.14)$$

and the **SE** for the \hat{H}_n is

$$\left\{ \hat{T}_n + \hat{V}_{nn} + E_\nu(\mathbf{R}) \right\} \Phi_\nu^n(\mathbf{R}) = E_\nu^{en} \Phi_\nu^n(\mathbf{R}), \quad (3.15)$$

these two equations are coupling by the total electronic energy $E_\nu(\mathbf{R})$, which becomes to act in the **Equ.** (3.15) as potential energy. A good way to estimate the total energy is setting \hat{T}_n to zero and just calculating the electrostatic potential of the nuclei-nuclei interaction \hat{V}_{nn} by giving a determinate configuration and then adding it to $E_\nu(\mathbf{R})$. This means that the total energies of the system can be calculated very “easily” after solving **Equ.** (3.14) [59, Section 3.1].

In the **Equ.** (3.15) the total energy of the electrons, together with the electronic nuclei-nuclei repulsion interaction, constitute the total potential energy of the nucleus $E_p(\mathbf{R}) = \hat{V}_{nn} + E(\mathbf{R})$. It has its own name, defining as the potential energy surface (**PES**), in the **Figure.** 3.1 show a schematic how it can look,

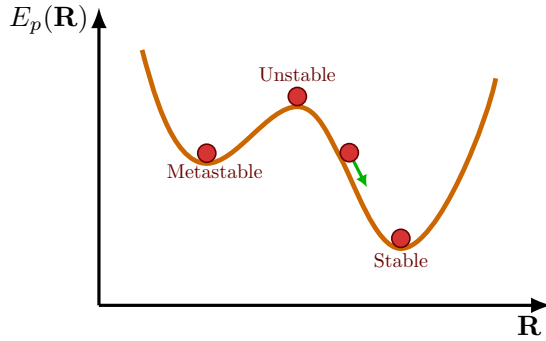


Figure 3.1: Schematic representation of the PES which show one metastable state local minimum, unstable state, and the stable state global minimum.

Where \mathbf{R} is the fixed position of all nuclei in different configuration, when it makes any calculation, is always expected to be in the global minimum (stable state). Therefore, it is very important to minimize that the PES leaves the most stable state \mathbf{o} in terms of the energies with the less possible energies. It processes is related as well with the lattice structure of the material, so the optimization of the position of the atoms must be considered in the optimization of the lattice parameter ⁴. For further information on this idea related with DFT, see Ref. [60, Chapter 2 and 3].

3.5 Variational principle in quantum mechanics

The variational principle is a general strategic to solve the SE, in general the method provides a way to approximate the ground state in a system, see this referent further and some example [27, 47]. The main idea behind this method is a minimization of the energy functional $E[\tilde{\Psi}]$ as a function of some trial wave function $\tilde{\Psi}$, this method is based in an import theorem *Variation Principle* which is not difficult to prove, here it will be use the result. It says any trial wave function will result in a ground state energy is equal or greater than the exact ground state E_0 . See the proof Ref. [58, Section 1.3].

$$E[\tilde{\Psi}] = \langle \tilde{\Psi} | \hat{H} | \tilde{\Psi} \rangle \geq \langle \Psi_0 | \hat{H} | \Psi_0 \rangle = E_0. \quad (3.16)$$

The **Equ.** (3.16) gives import information, the smallest will be the energies better $\tilde{\Psi}$ and equally hold when it is made a full minimization of the $E[\tilde{\Psi}]$ with respect to the wave function $\tilde{\Psi}$, that meaning the exact ground state is found [61, Section 1.2].

In formal world, it will need to find the extreme of the energy functional or stationary points, but guaranteeing the normalization condition of wave function. It can be done by the so-called *Lagrange's method of undetermined multipliers* which is defined

$$\mathcal{L}(\tilde{\Psi}, E) = \langle \tilde{\Psi} | \hat{H} | \tilde{\Psi} \rangle - E(\langle \tilde{\Psi} | \tilde{\Psi} \rangle - 1), \quad (3.17)$$

E in the **Equ.** (3.17) is known as Lagrange multiplier [61, Section 1.2]. A very import point to take into account when it is trying to solve, coming in the fact that $|\tilde{\Psi}\rangle$ is

⁴The final state after an ion minimization is very sensitive to the initial condition, For instance, suppose that the system is found in the unstable state depending on such initial condition, it can fall in the metastable state instead of the real satble state

unknown, so the normally proceeded to estimate it is expanding in an any normalized eigenbasis $|\tilde{\Psi}\rangle = \sum_k c_k |\Psi_k\rangle$ and then the problem is translated to find the unknown coefficient c_k

$$\mathcal{L}(c_1, c_2, \dots, c_N, E) = \sum_{ij} c_i c_j H_{ij} - E \sum_i (c_i^2 - 1), \quad (3.18)$$

where in the **Equ.** (3.18) $H_{ij} = \langle \Psi_i | \hat{H} | \Psi_j \rangle$, and it is assumed the normalized condition $\sum_k |c_k|^2 = 1$. The normalized condition links to the fact these coefficients are not independent at all, and by chosen c_1, c_2, \dots, c_{N-1} arbitrary c_N will be determined. Then the coefficients and the Lagrange multiplier can be found by taking

$$\frac{\partial \mathcal{L}}{\partial c_k} = 0 \quad \text{whit} \quad k = 1, 2, \dots, N, \quad (3.19)$$

applying **Equ.** (3.19) in **Equ.** (3.18) leaves a very well-known mathematical problem, the general eigenvalue problem, which is solved by digitalizing the matrix H_{ij} . For further and completed steps read **Ref.** [58, Section 1.3].

$$\sum_j H_{ij} c_j = E c_i, \quad (3.20)$$

solving **Equ.** (3.20) is found the coefficient (eigenvector) and the energies (eigenvalues). The lowest eigenvalue will be the ground state energy of the system, and the ground wave function is expanded in these coefficients.

3.6 Hartree and Hartree-Fock approximation

In the **Section 3.5** was described general proceeded to solution of a **SE**, but It says almost anything about the form of the wave function in special dealing many-particles system (more or equal two electrons). The thing is when is dealing with just one electron thinking in to decompose the wave function as a linear combination of any normalized eigenbasis where is any of them just depend on one particle position, because it just on electron very coherent. If now thinking in the most easy many-particle example two electrons it does not make sense anymore the last idea in such a simple way, because the eigenbasis should be reflected dependency of the two electron. It is here where the Hartree and Hartree-Fock approximation comes to save this behavior.

Hartree and Hartree-Fock approximation can be thought as first step to achieve that the wave function represent to complicate many-particle system as **Equ.** (3.14) in the “simplest” ways to estimate the ground state by minimization the problem to effective single particle **SE** [58, Section 2.2][54].

3.6.1 Hartree approximation

The Hartree approximation use as base the single uncorrelated wave function to estimate the ground state of a many-body system. It means the wave function $\Psi(\mathbf{r})$ can be written as the product of the single wave function $\psi_j(\mathbf{r}_j)$ [62–64].

$$\Psi_H(\mathbf{r}) = \psi_1(\mathbf{r}_1) \psi_2(\mathbf{r}_2) \dots \psi_j(\mathbf{r}_j) \dots \psi_{N_e}(\mathbf{r}_{N_e}). \quad (3.21)$$

It is used this trial wave function **Equ.** (3.21) to calculate the expectation value of many-body system using the electronic Hamiltonian, result in

$$\begin{aligned} E[\Psi_H] &\equiv \langle \Psi_H | \hat{H}_e | \Psi_H \rangle = \langle \Psi_H | \hat{T}_e | \Psi_H \rangle + \langle \Psi_H | \hat{V}_{ee} | \Psi_H \rangle + \langle \Psi_H | \hat{V}_{en} | \Psi_H \rangle \quad (3.22) \\ &= \sum_j^{N_e} \int \psi_j^*(\mathbf{r}) \left(-\frac{\hbar^2}{2m_e} \nabla^2 \right) \psi_j(\mathbf{r}) d\mathbf{r} + \frac{q^2}{4\pi\epsilon_0} \left\{ \frac{1}{2} \int \int \frac{n(\mathbf{r})n(\mathbf{r}')}{\|\mathbf{r} - \mathbf{r}'\|} d\mathbf{r} d\mathbf{r}' \right. \\ &\quad \left. - \frac{1}{2} \sum_j^{N_e} \int \int \frac{\|\psi_j(\mathbf{r})\|^2 \|\psi_j(\mathbf{r}')\|^2}{\|\mathbf{r} - \mathbf{r}'\|} d\mathbf{r} d\mathbf{r}' - \sum_\alpha \int \frac{Z_\alpha n(\mathbf{r})}{\|\mathbf{r} - \mathbf{R}_\alpha\|} d\mathbf{r} \right\}, \end{aligned}$$

where it has been defined the density function,

$$n(\mathbf{r}) = \sum_j^{N_e} \|\psi_j(\mathbf{r})\|^2. \quad (3.23)$$

The first term in the **Equ.** (3.22) is the kinetic energy of the electron. The second terms come from the electron-electron interaction. The third arise to cancel the self-interaction of the electron (the single orbitals $\psi_i(\mathbf{r}) \neq \psi_j(\mathbf{r}')$), and it is known as self-interaction energy term. The last term is electron-nucleus interaction energy.

By minimization of the energy functional $E[\Psi] \equiv E[\psi_1, \psi_2, \dots, \psi_{N_e}]$ in **Equ.** (3.22) respect to the complex conjugate wave function $\psi_i^*(\mathbf{r})$ using the Lagrange multiplier with normalization constrain,

$$\mathcal{L}[\Psi_H, E] = E[\Psi_H] - \sum_j^{N_e} \varepsilon_j \left(\int \psi_j(\mathbf{r})^* \psi_j(\mathbf{r}) d\mathbf{r} - \delta_{jj} \right)$$

with $\mathcal{L}[\Psi_H, E] \equiv \mathcal{L}[\Psi_H, \varepsilon_1, \varepsilon_2, \dots, \varepsilon_{N_e}]$, then

$$\frac{\delta \mathcal{L}[\Psi_H, E]}{\delta \psi_j^*(\mathbf{r})} = 0 \text{ with } j = 1, 2, \dots, N_e,$$

it is obtained the very well-known Hartree equation,

$$\left\{ -\frac{\hbar^2}{2m_e} \nabla^2 + \frac{q^2}{4\pi\epsilon_0} \left[\int \frac{n(\mathbf{r}')}{\|\mathbf{r} - \mathbf{r}'\|} d\mathbf{r}' - \int \frac{\|\psi_j(\mathbf{r}')\|^2}{\|\mathbf{r} - \mathbf{r}'\|} d\mathbf{r}' - \sum_\alpha \frac{Z_\alpha}{\|\mathbf{r} - \mathbf{R}_\alpha\|} \right] \right\} \psi_j(\mathbf{r}) = \varepsilon_j \psi_j(\mathbf{r}) \quad (3.24)$$

ε_j is the single energies corresponding to each $\psi_j(\mathbf{r})$ orbital. For further details about functional derivate and step, see the **Refs.** [22, 61, 63, 65]. Note: The result above is applied directly to **Equ.** (3.14) but is not limited to this. It can be generalized for any external potential $U_{ext} \neq \hat{V}_{en}$, see **Ref.** [63].

The **Equ.** (3.24) look like more as single particle **SE** within an effective potential $V_{eff}^H(\mathbf{r})$ feeling by the electron in $\psi_j(\mathbf{r})$ orbital,

$$\left[-\frac{\hbar^2}{2m_e} \nabla^2 + V_{eff}^H(\mathbf{r}) \right] \psi_j(\mathbf{r}) = \varepsilon_j \psi_j(\mathbf{r}) \quad (3.25)$$

where $V_{eff}^H(\mathbf{r})$ is defined,

$$V_{eff}^H(\mathbf{r}) = \frac{q^2}{4\pi\epsilon_0} \left[\int \frac{n(\mathbf{r}')}{\|\mathbf{r} - \mathbf{r}'\|} d\mathbf{r}' - \int \frac{\|\psi_j(\mathbf{r}')\|^2}{\|\mathbf{r} - \mathbf{r}'\|} d\mathbf{r}' - \sum_\alpha \frac{Z_\alpha}{\|\mathbf{r} - \mathbf{R}_\alpha\|} \right], \quad (3.26)$$

in the **Equ.** (3.26) the first term correspond to Hartree potential

$$V_H(\mathbf{r}) = \frac{q^2}{4\pi\epsilon_0} \int \frac{n(\mathbf{r}')}{\|\mathbf{r} - \mathbf{r}'\|} d\mathbf{r}', \quad (3.27)$$

which represents “mean-field” electrostatic Coulomb potential that an electron feels due to the presence of other electrons [63].

Since in **Equ.** (3.22) is not really know the single true ψ_j , the next step in general is considered to expand the single wave function in any normalized eigenbasis $\psi_j(\mathbf{r}) = c_{j\lambda}\psi_\lambda(\mathbf{r})$ and the problem again becomes in to find the $c_{i\lambda}$ as **Equ.** (3.19), for further reading **Refs.** [54, 66, 67].

By solving **Equ.** (3.24), it can find the ground state energy $E[\Psi]$ and wave function $\Psi_H(\mathbf{r})$. Furthermore, it is necessary to mention the **Equ.** (3.24) has to be resolved in so-called “self-consistent-field method” since the self-dependence of ψ_j in **Equ.** (3.26) [68]. For further information **Refs.** [54, 55, 58].

An import point to mention in this representation the spin is not taken into account, the more completed description would be $\chi_j(\mathbf{x}) \equiv \chi_j(\mathbf{r}, \mathbf{s}) = \psi_j(\mathbf{r})\alpha(\mathbf{s})$ for spin up and $\chi_j(\mathbf{x}) \equiv \chi_j(\mathbf{r}, \mathbf{s}) = \psi_j(\mathbf{r})\beta(\mathbf{s})$ for spin down. Luckily, within the Hartree approximation since electrons are not correlated, the spin can be included to consider the fact that each orbital can be accommodated two electrons, which leaves a total the $N_e/2$ orbitals and does not change anything in **Equ.** (3.24). On the other hand, in the Hartree-Fock approximation to consider the antisymmetric property of the wave function should be taken more care, because the electron with parallel spin will be correlated, known as exchange correlation [58].

3.6.2 Hartree-Fock approximation

The Hartree-Fock approximation a difference to the Hartree to incorporate the antisymmetric properties of the electron and the fact the electron are indistinguishable [27, 47].

$$\hat{P}_{ij}\Psi(\dots, \mathbf{r}_i, \mathbf{s}_i, \dots, \mathbf{r}_j, \mathbf{s}_j, \dots) = -\Psi(\dots, \mathbf{r}_j, \mathbf{s}_j, \dots, \mathbf{r}_i, \mathbf{s}_i, \dots), \quad (3.28)$$

where **Equ.** (3.28) represent the fact the wave function must be antisymmetric with respect to exchange of particle, and \hat{P}_{ij} is known exchange operator. Putting these two facts together, the Hartre-Fock wave function can be written as Slater determinant [58, 62, 69, 70].

$$\Psi_{HF}(\mathbf{x}) = \frac{1}{\sqrt{N_e!}} \begin{vmatrix} \chi_1(\mathbf{x}_1) & \chi_1(\mathbf{x}_2) & \dots & \chi_1(\mathbf{x}_{N_e}) \\ \chi_2(\mathbf{x}_1) & \chi_2(\mathbf{x}_2) & \dots & \chi_2(\mathbf{x}_{N_e}) \\ \vdots & \vdots & \ddots & \vdots \\ \chi_{N_e}(\mathbf{x}_1) & \chi_{N_e}(\mathbf{x}_2) & \dots & \chi_{N_e}(\mathbf{x}_{N_e}) \end{vmatrix} \quad (3.29)$$

where $\Psi_{HF}(\mathbf{x}) \equiv \psi(\mathbf{r}_1, \mathbf{s}_1, \mathbf{r}_2, \mathbf{s}_2, \dots, \mathbf{r}_{N_e}, \mathbf{s}_{N_e})$ contains spin and position of the particles. By properties of the determinant at move two columns will be change the sign of the determinant saving the antisymmetric properties of the electrons, and the Paulin principle exclusion by two columns are equal the determinant is zero [27].

The process to find the ground state using the Hatree-Fock trial wave function **Equ.** (3.29) is analogous to that of the Hartre, this time has to be more care because the wave function is a determinant with depend on spin and position of the particle.

See further information in Refs. [63, 67, 71][54, Chater 4]. One comment more with respect to different approximation Hartree and Hartree-Fock to the wave function, the Hartree-Fock print out the exact exchange energy term [63, 71], which translates to a better approximation to the ground state.

3.7 Density Functional Theory (DFT)

The **DFT** method provides an alternative approach to approximating the ground state of a many-electron system by replacing the complex many-electron wave function with the electron density as the central variable, it makes significantly reducing computational complexity, because instead dealing with $3N$ freedom like Hartree and Hartree-Fock the system is reduced to 3 freedom. For further information, see Refs. [63, 72].

The bases of the **DFT** are sustained in two theorem bases called Hohenberg-Kohn theorem [73]. From these, it is possible to construct the “exact” ground state energy as function of the density, which is build using single Kohn-Sham (**KS**) orbitals by solution of the **KS** equations [63, 74, 75][76, Chapter 1].

3.7.1 The Hohenberg-Kohn theorems

In this part, the two Hohenberg-Kohn theorems will be presented and demonstrated, along with a simple explanation of why they are needed. It starts with Theorem I, which establishes the unique correspondence of the electron density, followed by Theorem II, which incorporates the variational principle to find the global minimum of the energy density functional [61].

Theorem I

For any external potential $V_{ext}(\mathbf{r})$, there exists a unique corresponding ground state density $n_0(\mathbf{r})$, and this contains all the information about the system.

The proof of this theorem is made for contradiction, It assumes two different external potentials called them $V_{ext}(\mathbf{r})$ and $V'_{ext}(\mathbf{r})$ where $V_{ext}(\mathbf{r}) \neq V'_{ext}(\mathbf{r}) + \text{constant}$, with the same ground density function and end up with that statements can not be true, which meaning for each external potential will exist a unique correspondence density function.

It would part the fact that each external potential will have its own Hamiltonian and wavefunction,

$$\hat{H} = \hat{T} + \hat{V}_{ee} + \hat{V}_{ext}, \quad (3.30)$$

$$\hat{H}' = \hat{T} + \hat{V}_{ee} + \hat{V}'_{ext}. \quad (3.31)$$

Using the Variational Principe on **Equs.** (3.30) and (3.31)

$$\begin{aligned} E_0 &< \langle \Psi' | \hat{H} | \Psi' \rangle = \langle \Psi' | \hat{T} + \hat{V}_{ee} + \hat{V}'_{ext} + (\hat{V}_{ext} - \hat{V}'_{ext}) | \Psi' \rangle \\ &= \langle \Psi' | \hat{H}' | \Psi' \rangle + \int [V_{ext}(\mathbf{r}) - V'_{ext}(\mathbf{r})] n(\mathbf{r}) d\mathbf{r}, \end{aligned} \quad (3.32)$$

doing the same step for the \hat{H}'

$$\begin{aligned} E'_0 &< \langle \Psi | \hat{H}' | \Psi \rangle = \langle \Psi | \hat{T} + \hat{V}_{ee} + \hat{V}_{ext} - (\hat{V}_{ext} - \hat{V}'_{ext}) | \Psi \rangle \\ &= \langle \Psi | \hat{H} | \Psi \rangle - \int [V_{ext}(\mathbf{r}) - V'_{ext}(\mathbf{r})] n(\mathbf{r}) d\mathbf{r}, \end{aligned} \quad (3.33)$$

where it is used the fact $V'_{ext}(\mathbf{r})$ and $V_{ext}(\mathbf{r})$ produce the same density $n(\mathbf{r})$ in the **Equs.** (3.32) and (3.33), and considering that $|\Psi\rangle$ and $|\Psi'\rangle$ are constrained to represent their respective ground states, then

$$E_0 < E'_0 + \int [V_{ext}(\mathbf{r}) - V'_{ext}(\mathbf{r})] n_0(\mathbf{r}) d\mathbf{r}, \quad (3.34)$$

$$E'_0 < E_0 - \int [V_{ext}(\mathbf{r}) - V'_{ext}(\mathbf{r})] n_0(\mathbf{r}) d\mathbf{r}, \quad (3.35)$$

adding **Equs.** (3.34) and (3.35) result,

$$E_0 + E'_0 < E'_0 + E_0. \quad (3.36)$$

Equ. (3.36) is contradictory, as a quantity cannot be strictly less than itself.

The first theorem is necessary to guarantee the possibility that some different wave function will not have the same ground density function, and then the ground state density functional has all the information of the system since the $n_0(\mathbf{r})$ is known, implying that the ground state wave function is known [61][53, Chapter 4]. Note: First, the last proof does not consider the fact that the ground state can be degenerate for complete demonstration, see **Refs.** [74, 77]. Second, the external potential referred could be represented just the nuclei-electron interaction \hat{V}_{en} , it is not limited to this [61].

Theorem II

For any external potential, the functional density of the true ground state $n_0(\mathbf{r})$ and energy $E[n_0]$ can be obtained by minimizing the functional energy $E[n]$ with respect to the electron density $n(\mathbf{r})$.

The proof is in some sense the same as the variational principle [58, Section 1.3] instead considering the energy functional dependent $\Psi(\mathbf{r})$, it is used implying the last theorem $\Psi[n]$. This result that total energy would be a functional of the density function $E[n]$, in consequence the other candidates too,

$$E[n] = T[n] + U_{ee}[n] + U_{ext}[n] \quad (3.37)$$

$$= F[n] + U_{ext}[n] \quad (3.38)$$

$$= F[n] + \int V_{ext}(\mathbf{r}) n(\mathbf{r}) d\mathbf{r}.$$

The functional $F[n]$ is called the universal functional because it is valid for any number of electrons and any external potential. However, its exact form is not known. In practice, approximations are required to calculate $E[n]$, as discussed in **Section 3.7.3**.

Applying the variational principle on **Equ.** (3.37), result in,

$$E_0 \leq \langle \tilde{\Psi}[\tilde{n}] | \hat{H} | \tilde{\Psi}[\tilde{n}] \rangle = E[\tilde{\Psi}[\tilde{n}]] \implies E_0 \leq E[\tilde{n}], \quad (3.39)$$

The equality holds in the case of a full minimization of $E[\tilde{n}]$ with respect to $\tilde{n}(\mathbf{r})$ in the **Equ.** (3.39). This argument follows from the variational principle, which implies that minimizing $E[\tilde{\Psi}[\tilde{n}]]$ yields the true ground state $|\Psi_0\rangle$, corresponding to the density $n_0(\mathbf{r})$. Moreover, it has to be a bidirectional relationship $|\Psi_0\rangle \Leftrightarrow n_0(\mathbf{r})$ [63, 74].

As before, the minimization process is carried out by the Lagrange multipliers under the constraint that the density integrate over all space has to be equal to the number of electrons,

$$\int_V n(\mathbf{r}) d\mathbf{r} = N_e \implies \mathcal{L}[\tilde{n}, \mu] = E[\tilde{n}] - \mu \left(\int \tilde{n}(\mathbf{r}) d\mathbf{r} - N_e \right). \quad (3.40)$$

Then, by minimized the energy functional **Equ.** (3.40) with respect to the density function result,

$$\mu = \frac{\delta E[\tilde{n}]}{\delta \tilde{n}} = \frac{\delta F[\tilde{n}]}{\delta \tilde{n}} + V_{ext}(\mathbf{r}), \quad (3.41)$$

where μ is the Lagrange multiplier applied to enforce the condition that the electron number remains constant. In addition, it carries a physical interpretation as the chemical potential of the electron [61, 63], meaning that μ corresponds to the energy required to add or remove an electron from the system.

The second theorem has the same meaning as the variation theorem, it would be guaranteed after the full minimization of the energy functional **Equ.** (3.41), it will end up with the exact ground state and energy.

3.7.2 The Kohn-Sham (KS) equations

In **Section 3.7.1**, the general concept of **DFT** and its foundations are discussed. Nevertheless, these two theorems do not provide any information about the specific form of the density or the method to determine it. A widely used approach for calculating the density function, and consequently deriving all ground state properties of the system, is the **KS** method [78, 79].

The **KS** method is based on the premise that the density function of the true system can be constructed from a system of non-interacting particles, commonly referred to as the **KS** system [63, 74]. The last give a way to construct the density function using auxiliary Hartree wavefunction approximation **Equ.** (3.21),

$$\Psi_H(\mathbf{r}) = \psi_1^{KS}(\mathbf{r}_1), \psi_2^{KS}(\mathbf{r}_2) \dots \psi_j^{KS}(\mathbf{r}_j) \dots \psi_{N_e}^{KS}(\mathbf{r}_{N_e})$$

where $\psi_j^{KS}(\mathbf{r})$ is called the single particle **KS** wavefuction. Then, the density function is found as the **Equ.** (3.23),

$$n(\mathbf{r}) = \sum_j^{N_e} \left\| \psi_j^{KS}(\mathbf{r}) \right\|^2. \quad (3.42)$$

The best thing here, even if the single particle **KS** wavefuction is not exact $\psi_j^{KS}(\mathbf{r}_j)$, they will end up with the exact density. Therefore, with the exact ground state energy [72, 79].

The trick in the **KS** theory is rewritten the unknown term in the energy functional **Equ.** (3.37), by terms that can be calculated using no interacting single **KS** wavefunction,

$$\begin{aligned} E[n] &= F[n] + U_{en}[n] \\ &= T_H[n] + U_H[n] + U_{en}[n] + \left(T[n] - T_H[n] + U_{ee}[n] - U_{ee}[n] \right) \\ &= T_H[n] + U_H[n] + U_{en}[n] + U_{XC}[n] \end{aligned} \quad (3.43)$$

where the two first term in the equation **Equ.** (3.43) kinetic and potential Hartre energy and the third therm is the nuclei-electron interaction **Equ.** (3.22),

$$T[n] = \sum_j^{N_e} \int \psi_j^{*KS}(\mathbf{r}) \left(-\frac{\hbar^2}{2m_e} \nabla^2 \right) \psi_j^{KS}(\mathbf{r}) d\mathbf{r}, \quad (3.44)$$

$$U_H[n] = \frac{q^2}{4\pi\epsilon_0} \frac{1}{2} \int \int \frac{n(\mathbf{r})n(\mathbf{r}')}{\|\mathbf{r} - \mathbf{r}'\|} d\mathbf{r} d\mathbf{r}', \quad (3.45)$$

$$U_{en}[n] = \int V_{en}(\mathbf{r})n(\mathbf{r}) d\mathbf{r}, \quad (3.46)$$

and the last remaining term is called the exchange-correlation energy

$$U_{XC}[n] = \Delta T[n] + \Delta U[n] = T[n] - T_H[n] + U_{ee}[n] - U_{ee}[n]. \quad (3.47)$$

The exchange-correlation (**XC**) energy is unknown, it would take into account all the interaction that is not included in the other three terms **Equs.** (3.44), (3.45) and (3.46) as the self-interaction energy that appears in the Hartree energy **Equ.** (3.22).

Applying the functional derivate to carry out the minimization process with respect to density function, the **Equ.** (3.43) result

$$\mu = \frac{\delta E[n]}{\delta n} = \frac{\delta T_H[n]}{\delta n} + V_H(r) + V_{en}(r) + V_{XC}(r), \quad (3.48)$$

the second and third terms are known, they are respectively the Hartree potential and electron-nuclei potential interaction. On the other hand, the fourth term $V_{XC}(r)$ is call the **XC** potential. The **XC** potential is defined by analogy to the two before mention terms as

$$V_{XC}(r) = \frac{\delta U_{XC}[n]}{\delta n}. \quad (3.49)$$

Since the definition of the density function **Equ.** (3.42) which depend directly on single wavefunctions $E[n] \equiv E[\psi_1^{\text{KS}}, \psi_2^{\text{KS}}, \dots, \psi_{N_e}^{\text{KS}}]$, it is possible to minimize the energy functional with respect to the single **KS** wave function instead of the density. The hold process is equivalent to the Hartre theory **Section 3.6**,

$$\mathcal{L}[\Psi_H, E] = E[n] - \sum_j^{N_e} \varepsilon_j^{\text{KS}} \left(\int \psi_j(\mathbf{r})^* \psi_j^{\text{KS}}(\mathbf{r}) d\mathbf{r} - \delta_{jj} \right) \quad (3.50)$$

by performing the minimization in the **Equ.** (3.50) with repect $\psi_j^{\text{KS}}(\mathbf{r})$, it will end up with the **KS** equation

$$\left[-\frac{\hbar^2}{2m_e} \nabla^2 + V_{eff}^{\text{KS}}(\mathbf{r}) \right] \psi_j^{\text{KS}}(\mathbf{r}) = \varepsilon_j^{\text{KS}} \psi_j^{\text{KS}}(\mathbf{r}) \quad (3.51)$$

where $V_{eff}^{\text{KS}}(\mathbf{r})$ is called the **KS** effective potential, and is defined

$$\begin{aligned} V_{eff}^{\text{KS}}(\mathbf{r}) &= V_H(r) + V_{en}(r) + V_{XC}(r) \\ &= \frac{q^2}{4\pi\epsilon_0} \int \frac{n(\mathbf{r}')}{\|\mathbf{r} - \mathbf{r}'\|} d\mathbf{r}' - \sum_\alpha \frac{Z_\alpha}{\|\mathbf{r} - \mathbf{R}\|} + \frac{\delta U_{XC}[n]}{\delta n}. \end{aligned} \quad (3.52)$$

In the **Equ.** (3.51), the solution $\varepsilon_j^{\text{KS}}$ and $\psi_j^{\text{KS}}(\mathbf{r})$ are refers as **KS** eigenvalues and orbitals respectively.

To find the total energy of the system, it is needed to multiply by $\psi_j^{\text{KS}}(\mathbf{r})$ summing over number of occupied states (**occ**) after integrating over volume in the equation **Equ.** (3.51),

$$T_H[n] + 2U_H[n] + U_{en}[n] + \int V_{XC}[n]n(\mathbf{r}) d\mathbf{r} = \sum_j^{\text{occ}} \varepsilon_j \quad (3.53)$$

by combining **Equ.** (3.53) and **Equ.** (3.43), the total energy result

$$\begin{aligned} E[n] &= \sum_j^{\text{occ}} \varepsilon_j - U_H[n] + E_{XC}[n] - \int V_{XC}(\mathbf{r})n(\mathbf{r}) d\mathbf{r} \\ &= \sum_j^{\text{occ}} \varepsilon_j - \frac{q^2}{4\pi\epsilon_0} \frac{1}{2} \int \int \frac{n(\mathbf{r})n(\mathbf{r}')}{\|\mathbf{r} - \mathbf{r}'\|} d\mathbf{r} d\mathbf{r}' + E_{XC}[n] - \int V_{XC}(\mathbf{r})n(\mathbf{r}) d\mathbf{r}. \end{aligned} \quad (3.54)$$

The **KS** eigenvalues and eigenfunction are found by solving the **Equ.** (3.51). It is solved in the exact same manner as in the Hartree and Hartree-Fock theories, using the self-consistent-field (**SCF**) method since the Hartree potential and the **XC** depend on the density. The steps to find the ground state energy is started with a guess to the density, construct the effective **KS** potential **Equ.** (3.52) and solving the **KS** equation **Equ.** (3.51). These orbitals are then used to calculate a new density **Equ.** (3.42), and the cycle is repeated until some convergence criterion [63][59, Chater 7][54, Chater 5]. Further discussion, see **Section 3.7.3**.

There is an import thing that has to be mention, the Hartree and Hartree-Fock thorie look very similar to **DFT**, but the phylosophy of these are different. The two first as names indicate, they are just approximations to the ground state energy of the many-body symten, while **DFT** would give the “exact” ground state. Even though, the **KS** solution $\varepsilon_j^{\text{KS}}$ and $\psi_j^{\text{KS}}(\mathbf{r})$ are not the true if the **XC** energy is exact.

3.7.3 Approximations to the exchange-correlation (XC) energy

The **KS** result guarantee that the exact ground state of the Many-Body system can be found my the full minimization of the energy functional. Even thought, the **KS** orbitals are not the true single electronic orbital of the system, if the **XC** energy function is still exact. As has been mentioned before, in practice some approximation to **XC** part has to be done, since it is in general an unknown quantity [63]. Here, it would briefly introduce the 3 main approximations, but there are more and each one has its own advantaged and disadvantaged. Further reading, see **Refs.** [53, 59, 75, 76].

Local density approximation

The local density approximation **LDA** is the most simples one is based in the uniform electron gas **UEG** [78]. it is referenced as an **XC** energy potential that just depend on local position of the electron density $n(\mathbf{r})$ at the position \mathbf{r} . It is defined as

$$E_{XC}^{\text{LDA}}[n] = \int \varepsilon_{XC}^{\text{HEG}}[n(\mathbf{r})] n(\mathbf{r}) d\mathbf{r}, \quad (3.55)$$

where $\varepsilon_{XC}^{\text{HEG}}[n(\mathbf{r})]$ is **XC** energy of the **UEG** with density $n[\mathbf{r}]$. This aproxiatmion condider a unifom distributed electron gas, resulting a constante density $n(\mathbf{r}) = N_e/V_{cell}$. The explicit expression for $\varepsilon_{XC}^{\text{HEG}}[n(\mathbf{r})]$ can be written down

$$\begin{aligned} \varepsilon_{XC}^{\text{HEG}}[n(\mathbf{r})] &= \varepsilon_X^{\text{HEG}} + \varepsilon_C^{\text{HEG}} \\ &= -\frac{1}{4} \left(\frac{3n(\mathbf{r})}{\pi} \right)^{1/3} + \begin{cases} A \ln r_s + B + Cr_s \ln r_s + Dr_s, & r_s < 1 \\ \frac{\gamma}{1+\beta_1 \sqrt{r_s} + \beta_2 r_s}, & r_s \geq 1 \end{cases} \end{aligned} \quad (3.56)$$

where r_s is the Wigner–Seitz radius which is related with the density by

$$r_s = \left(\frac{3}{4\pi n(\mathbf{r})} \right)^{1/3}.$$

The term E_C^{HEG} is just interpolation approximation formula to compense the self-interteration and other out term. But exciting different form to make this interpolated. For further detail, see **Refs.** [54, 78, 80].

Generalized-gradient approximation

The Generalized Gradient Approximation (**GGA**) represents a significant improvement over the **LDA**. While **LDA** assumes a locally uniform electron gas and depends uniquely on the electron density $n(\mathbf{r})$, **GGA** improves accuracy by incorporating variation of the density through its gradient $\nabla n(\mathbf{r})$ [54]. Physically, It captures how the electronic density changed in a region, allowing it to better represent inhomogeneities present in real materials in cases where the electron density vary rapidly such as molecules, surfaces, and atoms. The general expression can be written as

$$E_{XC}^{\text{GGA}}[n] = \int \varepsilon_{XC}^{\text{HEG}}[n(\mathbf{r}), \nabla n(\mathbf{r})] n(\mathbf{r}) d\mathbf{r}. \quad (3.57)$$

GGA by taking into account the gradient of the density is transformed in a more complicated object, leaving different “fitting” parameters. This opens the creation of several **GGAs** approximation under certain condition. Here, it would use one of the most known the Perdew, Burke and Ernzerhof **PBE** [81].

Hybrid functionals

It is very well-known that **GGAs** has problem to describe the band gap. There is an inclination to underestimate it. While pure Hartree-Fock theory tends to overestimate the band gap even though it includes exact exchange. This is because it neglects electron correlation, leading to an underestimation of screening in the electron-electron interaction and thus an increased electron-electron repulsion. So hybrid functional appear as alternative way to compensate this two behavior, including some part of the exact exchange energy from the Hartee-Fock theory [82][83]. Here, it would consider where only the short-range exchange is mixed

$$E_{XC}^{\text{hybrid}} = a E_X^{\text{HF,SR}}(\omega) + (1 - a) E_X^{\text{GGA,SR}}(\omega) + E_X^{\text{GGA,LR}}(\omega) + E_C^{\text{GGA}}, \quad (3.58)$$

where a is the mixing parameter for **HSE06** which would be used in this thesis is $a = 0.25$ [84], and ω is the range-separation parameter controlling the division between short-range **SR** and long-range **LR** contributions. This split Coulomb operator into **SR** and **LR** parts using the error function

$$\frac{1}{r} = \underbrace{\frac{\text{erfc}(\omega r)}{r}}_{\text{SR}} + \underbrace{\frac{\text{erf}(\omega r)}{r}}_{\text{LR}}. \quad (3.59)$$

This separation allows for an efficient treatment of exchange, improving accuracy in systems where long-range screening or localization plays a key role, such as semiconductors and insulators.

3.8 Beyond Hartree–Fock theory

The last sections below is discussed the basis idea to approximate the ground state of the many-body fermions, here it will be introduced two more general approach to find the ground state of the many-body system the **MBPT** and **GFT**.

3.8.1 Many-body perturbation theory (MBPT)

3.8.2 Green's Function Theory (GFT) and GW approximation (GW)

Chapter 4

A brief overview of the implemented computational methods

In the last chapter (**Chapter 3**) was introduced the theoretical background to solve Many-Body problem in crystalline system, without mention so much details about their implementation. In this chapter would be a brief overview of the computation implementation, particularly focus on **KS** method in related with point defect. It would start by introducing the supercell approach and the periodic boundary condition **PBC**. Then, the implementation of the **KS** equation together with **SCF** procedures. Finally, a short discussion of the practical test to consider to performed **DFT** calculation.

4.1 Supercell approach and period boundary conditions

The supercell approach is the primary method used to calculate point defects under periodic boundary conditions (**PBC**), with the supercell being an extension of the primitive unit cell generated by a translation matrix operation. This method is a computation efficient way to calculated point defect properties, giving result comparable with experiments [85]. On the other, the **PBE** are a mathematical “trick” used in simulations to mimic an infinite crystal using a finite sized cell or supercell, repeating infinite times a slab (cell or supercell) in the **3-2-1D**, see on **Figure. 4.1**. The **PBC** mathematically can be written as

$$\Psi(\mathbf{r} + \mathbf{L}) = \Psi(\mathbf{r}) \implies e^{i\mathbf{k}\cdot\mathbf{L}} = 1 \implies \mathbf{k} \cdot \mathbf{L} = 2\pi n; n \in \mathbb{Z}, \quad (4.1)$$

where the quantization of the reciprocal space **Equ.** (4.1) comes directly from apply the Block theorem (**Section 3.2**) over **PBC**¹. This result bring out the fact the sampling or mesh to perform any calculation in the reciprocal space would be discreted and inversely proportional to supercell size **L**.

In the **Figure. 4.1** is also shown the point defect repetition (red points) due to **PBC** applies on supercell (blue color), which would result in self-defect artificial interaction which has to be removed, see **Section 5.2.2**.

¹**PBC** play another important role in the study of point defects, because without them, Bloch theorem cannot be applied, as the potential is no longer periodic.

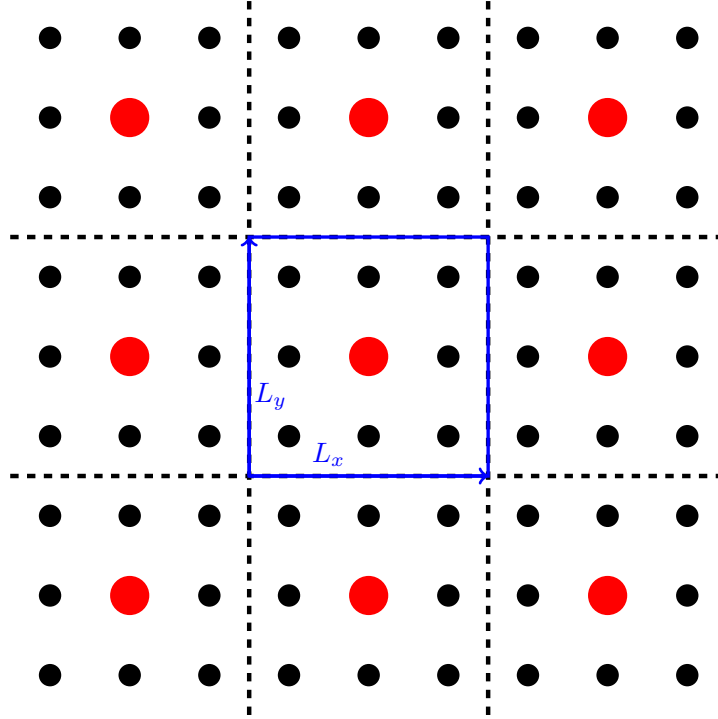


Figure 4.1: Illustration of the supercell approach for a point defect using PBC

4.2 Implementation of the **KS** wave functions

In the **Equ.** (3.51) is clear that **KS** orbitals are unknown, the general procedure fin a solution again by expanding these in a finite set orthonormalized eigenbasis². Since, they are in a periodic effective potential, an appropriate choice for the basis would be those with a Block functions structure **Equ.** (3.11). In Block function structure $u_{\mathbf{k}}(\mathbf{r})$ is a periodic function, which means that should be expanded in a bases set of periodic function to maintain its periodicity. Then the wave function can be written as

$$\psi_{\mathbf{k}}^{\text{KS}}(\mathbf{r}) = e^{i\mathbf{k}\cdot\mathbf{r}} u_{\mathbf{k}}(\mathbf{r}) = \sum_{\mathbf{G}} c_{\mathbf{G}}^{\mathbf{k}} f_{\mathbf{G}}(\mathbf{r}) e^{i\mathbf{k}\cdot\mathbf{r}} \implies u_{\mathbf{k}}(\mathbf{r}) = \sum_{\mathbf{G}} c_{\mathbf{G}}^{\mathbf{k}} f_{\mathbf{G}}(\mathbf{r}). \quad (4.2)$$

The last thinking can be done with the effective periodic potential. The easiest way to expand them, it is using plane wave. Then the **Equ.** (4.2) is transformed in³

$$\psi_{n\mathbf{k}}^{\text{KS}}(\mathbf{r}) = \sum_{\mathbf{G}} c_{\mathbf{G}}^{\mathbf{k}} e^{i(\mathbf{G}+\mathbf{k})\cdot\mathbf{r}}; \mathbf{k} \in \text{First } \mathbf{BZ} \quad (4.3)$$

²Theoretically, the basis set should be infinite, but for practical computational implementation, it must be truncated.

³In the **Equ.** (4.3) have been used the fact $\psi_{\mathbf{k}+\mathbf{G}}^{\text{KS}}(\mathbf{r}) = \psi_{\mathbf{k}}^{\text{KS}}(\mathbf{r}) \equiv \psi_{n\mathbf{k}}^{\text{KS}}(\mathbf{r})$ with \mathbf{k} in the first **BZ** and n makes referenced to each respective band. For further detais, see Refs. [22, Chapter 2][24, Chapter 6].

and the effective **KS** potential

$$V_{eff}^{KS}(\mathbf{r}) = \sum_{\mathbf{G}} V_{\mathbf{G}} e^{i\mathbf{G}\cdot\mathbf{r}} \implies V_{\mathbf{G}} = \frac{1}{V_{cell}} \int_{V_{cell}} V_{eff}^{KS}(\mathbf{r}) e^{i\mathbf{G}\cdot\mathbf{r}} d\mathbf{r}. \quad (4.4)$$

Applying **Equs.** (4.3) and (4.4) into **Equ.** (3.51), the **KS** equation can be rewritten in the reciprocal space as

$$\left[\frac{\hbar^2}{2m} (\mathbf{G} + \mathbf{k})^2 \right] c_{\mathbf{G}}^{\mathbf{k}} + \sum_{\mathbf{G}'} V_{\mathbf{G}-\mathbf{G}'} c_{\mathbf{G}'}^{\mathbf{k}} = \varepsilon_{n\mathbf{k}}^{KS} c_{\mathbf{G}}^{\mathbf{k}}, \quad (4.5)$$

solving the generalized eigenvalue problem **Equ.** (4.5), it would end up with the **KS** eigenvector $c_{\mathbf{G}}^{\mathbf{k}}$ and eigenvalues $\varepsilon_{n\mathbf{k}}^{KS}$ relate to each \mathbf{k} wavevector ⁴ [22, Chapter 2].

This approach is effective considering only the valence electrons of the system, which are the electrons in the outermost shell of the atoms. While, for the core electrons (internal shells) would not be efficiently or treatable, since the electrons closer to the nuclei have very rapidly oscillation wavefunction. It is not easy to capture for the plane, needing a huge set of plane wave, which is not efficient or allow computational.

To deal with rapidly oscillation of the core electron is through Pseudopotential methods. A Pseudopotential method replace the real potential near the nucleus with a smooth, leaving a screening potential (pseudopotential) that gives the same result for valence electrons. For further reading, see **Refs.** [22, Chapter 2][59, Chapter 11–17][54, Chapter 6]. Here, it would use a method called Projector Augmented-Wave **PAW** [86], which is a more sophisticated method that combines efficiently the idea of pseudopotential with the plane wave [87–91].

4.3 Self-consistent field (SCF) method

As was brief early discussed, the **KS** has to be solved within **SCF** method because the effective potential $V_{eff}^{KS}(\mathbf{r})$ depends on density $n(\mathbf{r})$, it depends on single **KS** orbitals $\psi_{n\mathbf{k}}^{KS}(\mathbf{r})$, which turn in dependents directly of the form $V_{eff}^{KS}(\mathbf{r})$.

The processes would start with an initial guess for the ionic configuration and the electronic density $n_0(\mathbf{r})$ to then construct the effective potential $V_{eff}^{KS}(\mathbf{r})$. Once the effective potential is known, the **KS** equation can solve, leaving a set of new **KS** single orbitals through which it is calculated a new density $n(\mathbf{r})$ that is used to find a new effective potential to solve again **KS** equation. After, the old and new densities are compared along with the total energy. These steps are repeated until some convergence criterion for the total energy different between the old and new density, where the energies, forces, pressure, and other properties are given as output for the given atomic configuration. Then, a new quantity is checked, checking if the total force $F_{total} = \sum_{N_\alpha} F_\alpha$ with F_α the force that feels by the atom α is sufficiently small ($F_{total} \approx 0$) or satisfied some small criterion, resulting final outputs: atomics configuration, energy, forces, pressure, and the other poetries. If this test fails, a new configuration is suggested and the full process have to be repeated. The full Flowchart is shown in the **Figure.** 4.2.

⁴The **Equ.** (4.5) is esentially a Fourier transform from the real to reciprocal space (frequency space)

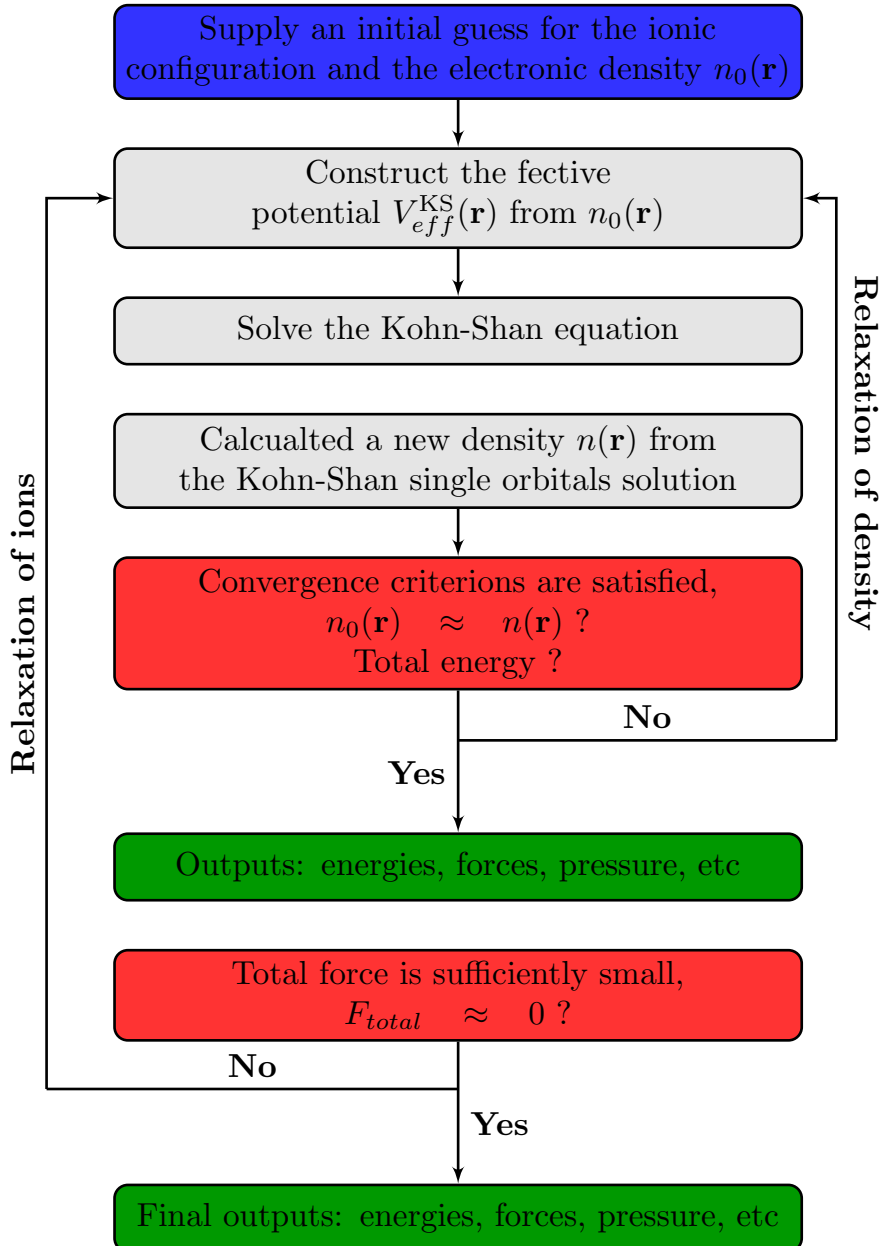


Figure 4.2: Flowchart of the SCF KS method

4.4 Practical considerations

In **DFT** calculations, one should always perform convergence tests on all related parameters. In practice, this task can be challenging due to the large number of parameters involved. Therefore, convergence tests are usually carried out only for the most relevant ones. Convergence tests are crucial for reducing unnecessary computational cost while maintaining desired accuracy, identifying suitable values for key parameters.

For every new material has to be found optimal energy cutoff (E_{cut}). The E_{cut} is the maximum kinetic energy allowed for the plane waves \mathbf{G} used to expand the single **KS** orbitals (**Equ.** (4.3)) for each wavevector \mathbf{k} . Thus, the size of the basis set is defined by

including only the plane waves with kinetic energy less than or equal to this value

$$|\mathbf{G} + \mathbf{k}| \leq \mathbf{G}_{cut} \implies E_{cut} = \frac{\hbar^2 \mathbf{G}_{cut}^2}{2m_e}. \quad (4.6)$$

The **Equ.** (4.6) leaves different set of wavevectors \mathbf{G} to expand each **KS** orbital for different value of \mathbf{k} in the reciprocal space.

This convergence test may be carried out by varying E_{cut} over a certain range and calculating the total energy for each corresponding value. Alternatively, it can also be performed using relative energy energies between two similar structures instead of total energy directly. Normally, the latter is the most interesting, because it can be related to measurable physical quantities, which are the ultimate objective [60, Chapter 3]. Futher details are giving in the **Section 5.1**.

Another important test is the number of k-points used to sample the reciprocal space, or more accurately, the number of k-points per volume (k-point density). The reason is simple, for many physical quantities would need to perform an integration over the first **BZ** because the **KS** equations are solved independently for each k-point. As a result, an accurate integration over the first **BZ** is required and significantive portion of the work reduces to computing integrals of the form

$$g = \frac{1}{V_{BZ}} \int_{BZ} g(\mathbf{k}) d\mathbf{k}, \quad (4.7)$$

being V_{BZ} the volume for the first **BZ**. In order to reduce unnecessary computational time to solve equations like **Equ.** (4.5) and **Equ.** (4.7), a suitable value for k-points denisty would be crucial. Moreover, since much of the computational effort in **DFT** comes from these two, an efficient way to sample the reciprocal space is also needed. This is done using a Monkhorst-Pack (**MP**) k-point mesh, it is a method that utilizes the symmetric properties of the material to generate the k-point mesh that decreases the number of k-points that need to be evaluated. For intance, A **MP** k-point mesh would have (N_1, N_2, N_3) , with being N_i the number k-ponts to sample the **BZ** along each direction of the reciprocal vector $(\mathbf{b}_1, \mathbf{b}_2, \mathbf{b}_3)$, which have a related k-points density giving by $N_i = \text{intreger}(\|\mathbf{b}_i\| \times \mathbf{k}\text{-points density})$ [60, Chapter 3].

4.5 $\mathbf{G}_0\mathbf{W}_0$ calculations

Chapter 5

Methodology

In this chapter would introduce the different method used in this thesis, it is mainly divided in fifth part. The first part is concerning to the convergence treatment to perform the convergence test for the unit and supercell calculation. The second is related to the theoretical framework of the formation energy apply to defect, it is discussed the chemical potential limit and their relation with the experimental ground condition, the different correction error consideration for accuracy result, then the construction of the formation energy diagram for a target defect and their thermodynamic charge transition levels (**CTLs**). The third part is regarded to the **KS** eigenvalue spectrum and their orbital localization, explaining a way to consider excite state through **KS** spectrum and the importance of localization for **QT** application. Finally, the last part takes into account the optical properties of point defect, mostly the **ZPL** energy, which is a very important quantity for this thesis.

5.1 Convergence tests

Here, it considers the different convergence: unit cell and supercell. For the convergence testes are always considered the relative energy between different configuration instead a total energy since the relative energy tends to converge more rapidly [60, Chapter 3]. For each one, it is explained below the idea how is performed the test. Concerning the energy convergence of the unit cell is performed by considering two different structure calcualtion without ionic relaxation, the first which just will call reference structure ($E^{tot}[ref]$) which is the relax unit cell and similar structure ($E^{tot}[dis]$) which one atom is slight displacement away from its reference position. This displacement has to be small to be sure that two structures have similar configuration of atoms and make able to compare.

The relative energies E_i^{rel} are calculated between both,

$$E_i^{rel} = E_i^{tot}[dis] - E_i^{tot}[ref] \quad (5.1)$$

where subindex i represents the total energy values corresponding to different cutoff values of the convergence targeted parameter, as: energy cutoffs or k-points, respectively. Since the structures are similar, it is reasonable to expect that this systematic numerical error is also similar for both. This means that the energy difference between the two structure **Equ.** (5.1) can be expected to cancel out at least a portion of this systematic numeric error, leading to calculated energy differences that are more accurate and faster convergence than the total energies [60].

To consider the stability of convergence, it calculates the absolute value of the relative energy difference $|\Delta E|$ of the consecutive E_i^{rel} ,

$$|\Delta E| = |E_{i+1}^{rel} - E_i^{rel}| \quad (5.2)$$

where $|\Delta E|$ gives information about how well converge the targeted parameter. In the best of cases tends to be zero for larger consecutive value, since the larger cutoff values more precision and less computation error it would appear. The last argument is true when is considered very similar structure, meaning it has similar numeric error.

Regarding the supercell convergence, it is performed similar way. This time is considered the relative energy without defect ($E^{tot}[\text{Bulk}]$) and with defect X ($E^{tot}[\text{X}]$),

$$E_i^{rel} = E_i^{tot}[\text{X}] - E_i^{tot}[\text{Bulk}] \quad (5.3)$$

where i has the same meaning as before. Here, it is taken into account the stability of the target convergence parameter using **Equ.** (5.2) with relative energy **Equ.** (5.3).

5.2 Defect formation energies

Defects in crystalline materials typically occur at very low concentrations, on the order of $10^{14} - 10^{18} [\text{cm}^{-3}]$. Due to their low concentration, they can be interpreted as isolated defects within the crystalline material. This makes the study of isolated or point defects particularly interesting using first-principles calculations. They can be modeled using the supercell approximation under **PBC**, which aims to realistically simulate a material by infinitely repeating a finite-sized supercell (see **Section 4.1**).

The started point to analyze point defect in semiconductor material for quantum application is always finding the most likely stable charge structures or thermodynamic stable related with each defect, a key quantity to allow calculating it is the formation energy [9, 92]. The formation energy determines different thermodynamics stable charge state as function of the Fermi energy, which is crucial to know accessibility of the ground state for each charge defects and their transition energy levels. No less important, it is determinate concentration of the defect expected in thermodynamic equilibrium [9, 93]. The formation energies formalism is based in the thermodynamic Gran potential approach, it allows considering open system which may possible energy and particle interchange with an external reservoir. For further information about thermodynamic perspective **Ref.** [94].

The formation energy of a defect X in charge state q is defined as ¹

$$E^f[\text{X}^q] = E^{tot}[\text{X}^q] - E^{tot}[\text{Bulk}] - \sum_i n_i \mu_i + qu_e + E^{corr}[\text{X}^q] \quad (5.4)$$

where $E^{tot}[\text{X}^q]$ is the total energy of the supercell containing the defect X in charge state q and $E^{tot}[\text{Bulk}]$ total energy of the supercell without any defect. μ_i is the chemical potential related with each species, either added ($n_i > 0$) or removed ($n_i < 0$) from the supercell to reservoir for the atoms involved to create the defect. The term μ_e is the energy of the reservoir for electron exchange or electron chemical potential which is normally referenced as the energy of the higher occupied state or energy of the valence band maximum (E_{VBM}) ($u_e = E_F + E_{\text{VBM}}$), where E_F is the fermi energy. The term

¹The formation energy theory has been done following primary **Refs.** [9, 93, 95–97], within supercell approach [85]

proportional to μ_e accounts for the electrons, either added ($q < 0$) or removed ($q > 0$) from the bulk of the defect supercell. The last remaining term counts the finite charge error correction since the self interaction of charge defect with their periodic images and shift in the alignment referent potential since the charge defect, further discussion **Section 5.2.2**.

The chemical potential values in the **Equ.** (5.4) always depend on their implicit reference, for electronic structure calculations, chemical potentials normally are referenced with the total energy of the elementary phases of the atomic reservoir at $T = 0$ [K], varying the chemical potential within their boundaries condition given by the stability of the different stable phases [95]. They can be connected to the first-principles calculations with the experimental growth conditions. further discussion **Section 5.2.1**

5.2.1 Chemical potentials and limits

The conditions used during experimentation to create defects play a crucial role in determining the pertinent reservoirs. In contrast, adjusting the chemical potentials in the computations allows for the exploration of various experimental scenarios. In the broader framework, chemical potentials are treated as variables; nevertheless, they are constrained by specific limits dictated by the presence or emergence of secondary phases. When impurities are present, their chemical potentials are subject to similar bounds, imposed by the formation of stable phases with the elements of the host material, or among each other.

The chemical potential of the one system are linked by the stability phase it. For instance, a binary system composes A_xB_y has to follow

$$x\mu_A + y\mu_B = \mu_{A_xB_y} \quad (5.5)$$

The boundaries of the chemical potentials are set by the formation of the separated phase of the composed system or different stable phases, in such a way that the most stable condition is A_xB_y . Otherwise, it can not be possible to grow because its component system will be more stable and this should be collapse are one of them,

$$\mu_A \leq \mu(A, \text{Bulk}) \quad (5.6)$$

$$\mu_B \leq \mu(B, \text{Bulk}), \quad (5.7)$$

$$\nu\mu_A + \lambda\mu_B \leq \mu_{A_\nu B_\lambda} \quad (5.8)$$

when in the system is considered impurities (X), the chemical potential of these have to be into count and their boundaries. They are related with the elementarily chemical potential phases of the element. For instance, the chemical potential of the most stable

$$\mu_X \leq \mu(X, \text{Bulk}). \quad (5.9)$$

In electronic structure calculations, the numeric value of chemical potentials of species $\mu(A, \text{Bulk})$, $\mu(B, \text{Bulk})$ and $\mu(X, \text{Bulk})$ can be referenced to the total energy of the elementary phases at $T = 0$ [K]. By considering the relative energy with respect to the bulk,

$$\Delta\mu_A = \mu_A - \mu(A, \text{Bulk}) \quad (5.10)$$

$$\Delta\mu_B = \mu_B - \mu(B, \text{Bulk}) \quad (5.11)$$

$$\Delta\mu_{A_xB_y} = \mu_{A_xB_y} - x\mu(A, \text{Bulk}) - y\mu(B, \text{Bulk}) = \Delta G^f[A_xB_y] \equiv E^f[A_xB_y] \quad (5.12)$$

where $\Delta G^f[A_xB_y]$ is the formation free Gibbs enthalpy energy and for this particular case is equal to formation energy $E^f[A_xB_y]$, from the **Equs.** (5.5), (5.10), (5.11) and (5.12) is found

$$E^f[A_xB_y] = x\Delta\mu_A + y\Delta\mu_B \quad (5.13)$$

where the **Equ.** (5.13) is equivalent **Equ.** (5.5) without consider any referent condition.

Chemical potential limits

In this point it is considered two extreme possible conditions, these are so-called rich and poor condition. The rich condition makes referent that the concentration of the spice in question is height, while poor-condition makes referee to low consecration. For instance, the vacancy of spicies A in the binary compost A_xB_y under limit A-rich condition would cost larger energy since the external reservoir already has a high concentration of the species in question. On the other hand, in the A-poor condition where the reservoir has a lower concentration of A species, removal the species A from A_xB_y and placing it in this reservoir should be energetically cheaper. Therefore, A vacancy formation is more favorable under A-poor conditions.

A-rich condition

In the case of A-rich condition, the chemical potential of the species A is set to the upper limit $\mu_A = \mu(A, \text{Bulk})$, then the **Equ.** (5.13) becomes to be,

$$E^f[A_xB_y] = y\Delta\mu_B \implies \mathbf{A\text{-rich}}$$

the relative chemical potential of species B has to be in the lower limit (B-poor condition),

$$\mu_B = \frac{E^f[A_xB_y]}{y} + \mu(B, \text{Bulk}) \implies \mathbf{B\text{-poor}} \quad (5.14)$$

considering the **Equs.** (5.7) and (5.14) is found the boundaries for the chemical potential of the species B

$$\frac{E^f[A_xB_y]}{y} + \mu(B, \text{Bulk}) \leq \mu_B \leq \mu(B, \text{Bulk}). \quad (5.15)$$

B-rich condition

In the case of A-rich condition, the chemical potential of the species B is set to the upper limit $\mu_B = \mu(B, \text{Bulk})$, so

$$E^f[A_xB_y] = x\Delta\mu_A \implies \mathbf{B\text{-rich}}$$

the relative chemical potential of species A has to be in the lower limit (A-poor condition),

$$\mu_A = \frac{E^f[A_xB_y]}{x} + \mu(A, \text{Bulk}) \implies \mathbf{A\text{-poor}} \quad (5.16)$$

considering the **Equs.** (5.6) and (5.16) is found the boundaries for the chemical potential of the species A

$$\frac{E^f[A_xB_y]}{x} + \mu(A, \text{Bulk}) \leq \mu_A \leq \mu(A, \text{Bulk}). \quad (5.17)$$

For the boundary condition μ_A and μ_B , they have also to satisfy the constraint since the different stable phases **Equ.** (5.8). On the other hand, for the impurities have to respect the **Equ.** (5.9).

5.2.2 Finite size corrections in supercell calculations

The **PBC** play an important role when it tries to simulate real material with essentially infinite of atoms. It brings a problem when are considered point charge defect, since the periodic repeating of the supercell would be appeared periodic point defect imagines they can interact with each other leaving an artificial interaction which is consequence of the large Coulomb range interaction [85, 98]. Another aspect to include point charge defect, the energy potential reference is shift with respect to isolated defect truly point charge due to **PBC** charge interaction with the background charge of the bulk [99, 100]. Such as errors have to be correct through finite-size correction in the **Equ.** (5.4) really make able to compare the first-principle calculation with the experiment result.

There are different proposed schemes to achieve these corrections, for further reading **Refs.** [98, 99]. Here, it would introduce the basis idea of the method used which comes from the approach taken by Freysoldt, Neugebauer, and Van de Walle (**FNV**), see further reading in **Refs.** [98, 101, 102]. The finite-size error correction in the **FNV** scheme can be writing,

$$E_{\text{FNV}}^{\text{corr}} = E^{\text{lat}} - q\Delta V_{q/0} \quad (5.18)$$

in the **Equ.** (5.18), E^{lat} is desired correction corresponds to the difference between the electrostatic energies of the isolated and periodic defect charge distributions

$$E^{\text{lat}} = \frac{\alpha q^2}{2\epsilon L},$$

where q is the target charge model, α is the Madelung constant, L is the dimension of the supercell and ϵ is the macroscopic dielectric constant [99, 102]. Then is later improved by Makov and Payne deriving the correction term with the L^{-3} order [103]. While $\Delta V_{q/0}$ is referenced to the potential alignment term is obtained by comparing the potential from the model charge to the potential difference between charged and neutral

$$\Delta V_{q/0} = (V_q^{\text{DFT}} - V_0^{\text{DFT}})|_{\text{far}} - V_q^{\text{model}}|_{\text{far}},$$

being the two first terms the electrostatic potential with charge defect and neutral, respectively ². While, the last remain term V_q^{model} is the electrostatic potential of the Gaussian charge model, all far away of the point defect. For further detail, see the **Refs.** [98, 99, 102].

The last description as mention considers the macroscopic dielectric constant, for anisotropic material this scheme became to have problem. It makes necessary a reconstruction by consider the microscopy dielectric tensor instead of the constants value, see **Ref.** [99]. Therefore, here it used the packages **PYDEFECT** which contemplate the last mention to calculate the finite-error correction formation energy [104, 105].

5.2.3 Formation energy diagrams

Formation energy diagram is reference as a construction plot where are printed out all defect formation point charge energy for the different consider charge **Figure.** 5.1a. In a way to simplify this process is conveniently rewritten **Equ.** (5.4) in a more compact form,

$$E^f[\text{X}^q](\mu_e) = E_0^f[\text{X}^q, \mu_i] + q(E_F + E_{\text{VBM}}) \quad (5.19)$$

²If the reference energy is taken as bulk, the V_0^{DFT} has to be switched for the bulk electrostatic potential ($V_{\text{Bulk}}^{\text{DFT}}$) [99]

where $E_0^f[X^q, \mu_i]$ combine all therm in the **Equ.** (5.4) except that contain the electron chemical potential. Setting the chemical potential and the error charge correction associated with a target charge q , **Equ.** (5.19) is transformed in a simple linear equation with slop q and $E_0^f[X^q, \mu_i]$ being the fromation energy value when the chemical potential is located at energy zero ($u_e = 0$) or intersection at E_{VBM} . While, E_F is a varieble taking in the intervale $0 \leq E_F \leq E_{gap}$.

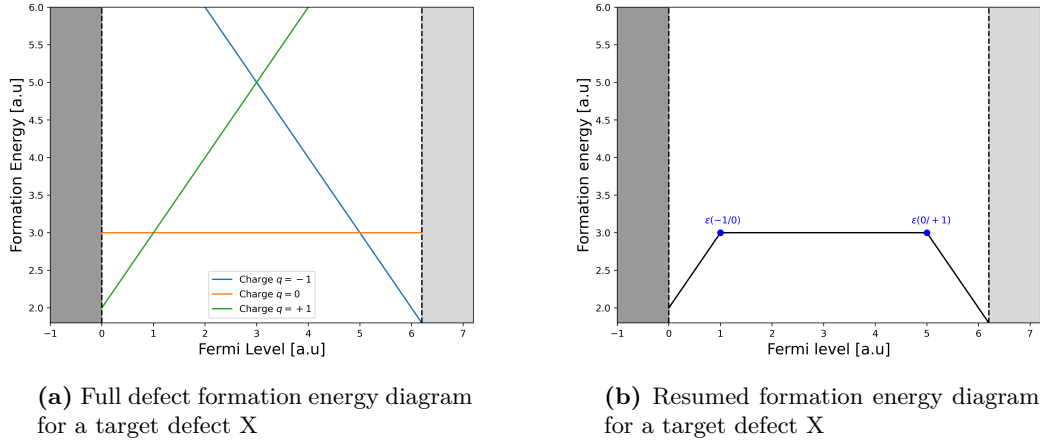


Figure 5.1: Formation energy diagram for a defect X consider 3 different charge states, (a) it is a full formation energy diagram, (b) resumed formation energy diagram

In the literature is normally using the way in the **Figure.** 5.1b, since it has all interesting physics. The different between those are simple, **Figure.** 5.1b cut off the unnecessary part or more precisely thermodynamic less favorable which meaning with a larger formation energy for a target defect in a determinate charge state. Note: In the figure **Equ.** (5.19) the dark and light gray fill represented the **VB** and **CB**, left and right respectively.

5.2.4 Thermodynamics charge transition levels (CTLs)

As was mention early, the formation energy determinate **CTLs** which is crucial in the study of the point defect calculations to know the region where a determinate charge state is in thermodynamic equilibria condition over a fermi region, it can visualize in the **Figure.** 5.1b with blue color point. For instance, in the context of quantum information, they define the Fermi level regions over which specific charge states and spin configurations are stable [9, 95]. The **TTL** between charged q and q' ($\epsilon(q/q')$) reference to **VBM** is defined as the intersections between formation energy of charges q and q' for a target defect X

$$\epsilon(q/q') = \frac{E_0^f[X^{q'}, \mu_i] - E_0^f[X^q, \mu_i]}{q - q'} - E_{VBM}. \quad (5.20)$$

The **CTLs** can estimate ionization energies, to change the system with charge state q to desire charge state [95]. No less important, It can directly observe in experiments such as in deep level transient spectroscopy (**DLTS**) [106].

5.3 KS eigenvalues and orbital localization factor (KSOLF)

In relation with the **Section 5.2** is normally taken into account the **KS** eigenvalues and localization factor (**KSOLF**). As was mention, the **KS** eigenvalues come from the solution of the **KS** equation **Equ.** (3.51), it could give an inside of the single orbital related with each electron in the ground state³. From **KS** eigenvalue spectrum **Figure.** 5.2a can be obtained the occupancies of the single **KS** orbitals, they can be used to study the spin vertical **TTSs** (**VTTLs**) and **ZPL** by doing a constrained-occupation calculation, which it essentially as name indicate constrained ground state to single determinant excite state [107, 108]. For instance, in the **Figure.** 5.2a makes able to excite a single electron for both spin channel by descoping the higher occupied **KS** orbital (red) into the lower unoccupied **KS** orbital (blue). For further information regarding **VTTLs** and **ZPL**, see the **Section 5.4**.

While from **KSOLF** spectrum **Figures.** 5.2b and 5.2c can be obtained the localization of such as orbital, this information is vital to know the robustness related with the interesting **KS** state created for the defect. Understanding robustness, how effective could be electronic transition. The later can be interpreted computational or either experimental. Computationally, it would reference how feasible to calculate the above mention transition, for this example it would be because the interesting states are very well localized **Figures.** 5.2c and 5.2b (yellow and green). Experimental, it could indicate that defect induced states can be excited by hitting the point defect with a photon of sufficient energy.

In practice, the unlocalized state can be easier interacted with the background bulk electron of the material than localized state, which makes these states normally depressing for use in **QT** application as: quantum qubit and color centers. On the other hand, the localized state has a well localized charge density surrounding the defect. This gives it its own isolated properties, making it interact less with the background bulk charge. [36, 109, 110].

As shown in the **Figure.** 5.2, the **KSOLF** is printed using two approaches. In the first or indirect approach, considering the ion orbital wights (**IOWs**) apport for determinate atoms to the total **DOS** for each band at the respective k-point, these atoms are always chosen inside a radius a bit larger than bonding between first neighbors related to point defect to guarantee only that atoms around the defect are taken into account. For instance, the radius chosen in this thesis is equal to 2.0 [Å] for w-AlN. In comparison with the second or direct approach call inverse participation rates (**IPRs**), **IPR** is considered directly the single wavefunction distribution for each orbital state as,

$$\text{IPRs} \equiv \text{IPR}_{nk} = \frac{\sum_i \left\| \psi_{nk,i}^{\text{KS}}(\mathbf{r}) \right\|^4}{\left\| \sum_i \left\| \psi_{nk,i}^{\text{KS}}(\mathbf{r}) \right\|^2 \right\|^2} \quad (5.21)$$

where $\psi_{nk,i}^{\text{KS}}(\mathbf{r})$ makes reference to the specific single **KS** orbital expanded on **PW** basis i at specific n and k energy band and k-point, respectively. The code implementation **VaspDefAnalysis** can be found **Ref.** [111].

³For a correct description of the single orbital wavefunction it is necessary to use more appropriated methods as: **MBPT** and **GW**. Thought, the **KS** orbitals are auxiliary mathematical constructs to reproduce the correct electron density. They could not necessarily correspond to real physical and can not be interpreted single wavefunction orbital as: Hartree, Hartree-Fock or beyond **FCI**, **MBPT** and **GW**

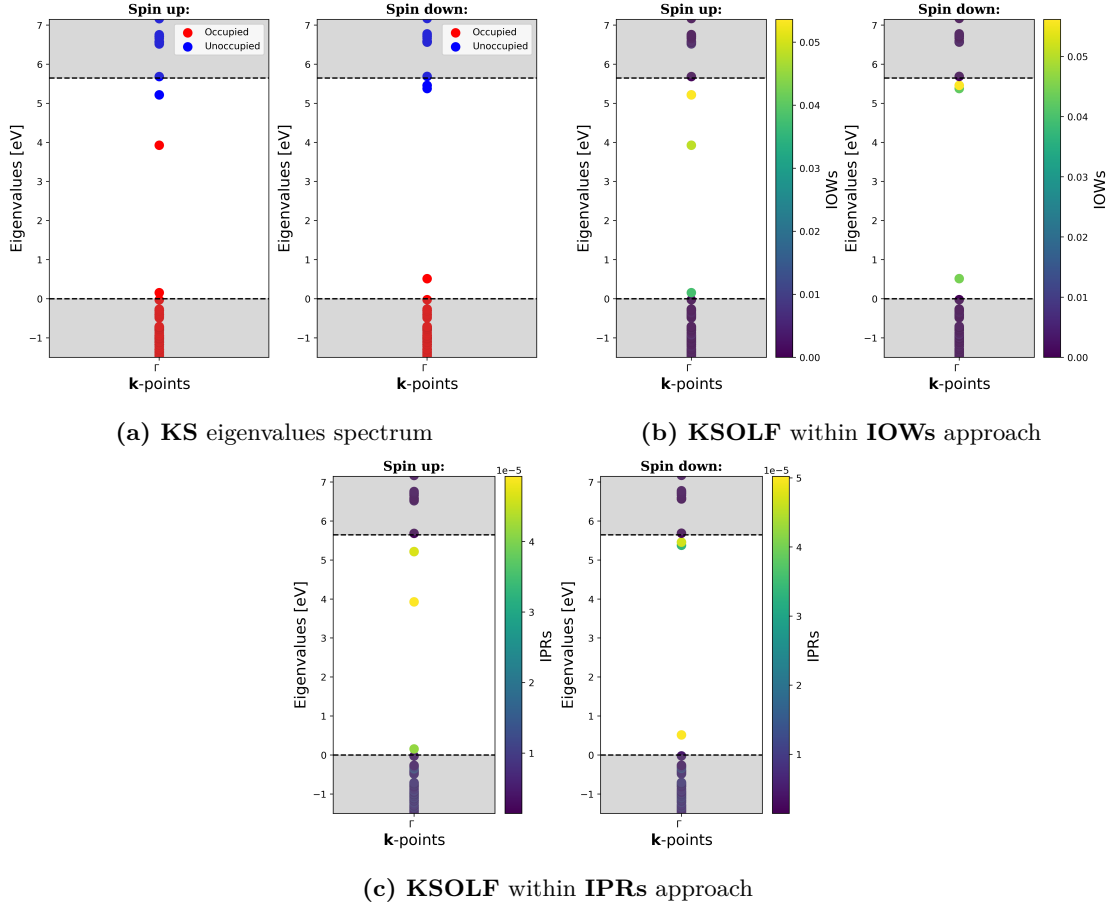


Figure 5.2: Spectrum, (a) **KS** eigenvalues, (b) **KSOLF** related with each **KS** orbitals using a Γ point. Note: The fill up gray region bottom and on top again represents the **VB** and **CB**, respectively.

5.4 Optical properties of defects: Zero phonon line (ZPL)

The optical properties of defect are referenced to experimental observation: absorption and emission energy. The first is the energy required to excite the system from ground state. The second term is the energy emitted for the system after a relaxation from excited to ground state. Both without any ion relaxation consideration as shown in the **Figure**. 5.3 with red arrow and commonly called **VTTLs**. These energies in defect in solid can be estimated by consider so-called one dimension configuration coordinate diagram **1D-CCD** which are represented through full figure.

1D-CCDs are a way to consider the coupling between a lattice vibration (phonon) and electronic state. They are based over the idea that based large number of vibrational modes of the full system with different frequencies contributing to the phonon line shape can be replaced by a single effective mode [109, 112]. As shown in the figure **Figure**. 5.3, they are defined under quantities: **Q** describing a configuration coordinate, and $E(\mathbf{Q})$ is the total **PSE** which behaves like a harmonic spring within harmonic approximation for both related configuration **Q** around ground \mathbf{R}^g and excited \mathbf{R}^e ($\mathbf{Q}_{\{g,e\}}\{\Delta\mathbf{R}_i\}$),

$$E_{\{g,e\}}(\mathbf{Q}) = E_{\{g,e\}} + \Omega_{\{g,e\}}(\mathbf{Q} - \mathbf{Q}_{\{g,e\}}\{\Delta\mathbf{R}_i\})^2 \implies (\Delta Q)^2 = \sum_{\alpha,i} m_\alpha (R_{\{\alpha,i\}}^e - R_{\{\alpha,i\}}^g)^2$$

where α is count for the number nucleus and $i = x, y, z$. $\Omega_{\{g,e\}}$ are the effective frequencies, they can be obtained by mapping the potential energy surface around the respective equilibrium geometries along the path that linearly interpolates between the two geometries \mathbf{R}^g and excited \mathbf{R}^e [95, 112]. For further overview and discussion of different approximation to calculated CCDs Refs. [112–114].

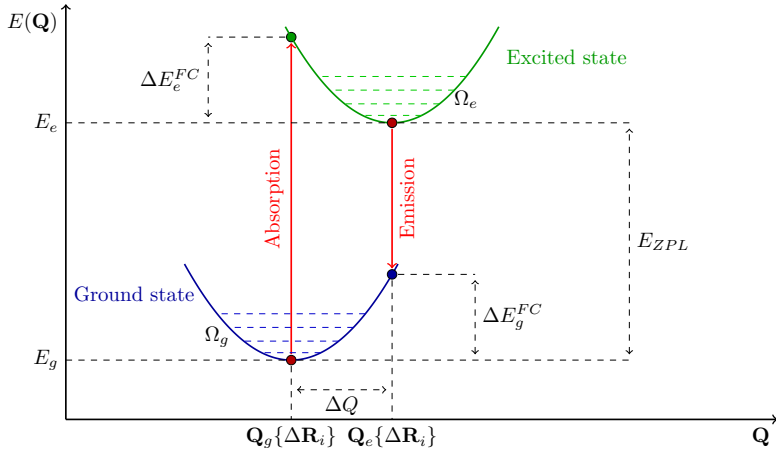


Figure 5.3: Configuration coordination diagram of a defect X under harmonic approximation for the ground and excited state.

The **VTTLs** are considered in the so-called classical Franck-Condon approximation, it assumes that the electron excitation occurred very rapidly that the nuclei does not have time to relax [112], they are defined

$$\begin{aligned} E_{abs} &= E_{\{e\}}(\mathbf{Q}_g) - E_{\{g\}}(\mathbf{Q}_g) \\ E_{emi} &= E_{\{g\}}(\mathbf{Q}_e) - E_{\{e\}}(\mathbf{Q}_e) \end{aligned}$$

with E_{abs} and E_{ems} being the absorption and emission energies, while $E_{g,e}^{FC}$ are the Franck-Condon shifts

$$\Delta E_{g,e}^{FC} = E_{abs,emi} - E_{ZPL},$$

they are the losing energy needed to do relaxation of the structure to each minimum state energy. The term E_{ZPL} is energy transition without any phonon interaction or the zero phonon line **ZPL**, it occurs when there is no vibration excite state available and the electron can be directly excite between minimum of ground and excite state the red points in the **Figure. 5.3**. It is defined

$$E_{ZPL} = E_e - E_g. \quad (5.22)$$

The **ZPL** energy **Equ. (5.22)** is normally the most attractive for quantum application since is pure electronic transition, it makes more isolated system a perturbation from the lattice that is crucial to maintain the quantum coherence. Another import thing that has to be mention, these transition energies E_{abs}, E_{emi} and E_{ZPL} can be directly measure through **PL** experiment [115, 116]. Moreover, The **ZPL** in **PL** experiment is usually very well-defined at low temperature with a pronounced peak, since missing phonon vibration.

Actually in **PL** and later mention **DLTS** experiments can not really give all information about the origin of the emissions (peaks), when they are analysis first principal calculation play a role vital to be able to identify them with a specific charged

defect. This is done, fitting the peak position with the energy result from the first principal calculation. Here, **DFT** becomes to be import since it have been demonstrated great agreement with the experiment, especially within **XC** approximation beyond **PBE** [106, 115, 116]. The previous one is necessary to be achievable realistic **QT**.

5.5 $\mathbf{G}_0\mathbf{W}_0$ calculations for the selected promising charged defects

Chapter 6

Results and discussion

This chapter presents the convergence tests and results for different calculations. The first section will start with the details of numerical convergence, which give support to perform different calculations. The second section emphasizes w-AlN bulk properties such as structural parameters, microscopic dielectric tensors, density of states (**DOS**), and band structure. The final section examines the different defects investigated: native, impurities and complex. Furthermore, it makes an analysis of **KS** eigenvalue distributions and their orbital localization factor to select some promising defect charge states for **QT** applications. Then, going further on selected charged defects, we calculated **ZPL** values and compared them with both the theoretical literature and experimental **PL** emission spectra. Lastly, we perform a **G₀W₀** calculation to the most promising defect candidate to better estimate electronic structure and compare with that obtained using **DFT**.

6.1 Numerical details

The resource utilized is **VASP** [117–119] on the high-performance supercomputer *SAGA*. We use **DFT** with two different **XC** functionals (**PBE** and **HSE06**) and **G₀W₀** methods within the **PAW** pseudopotential approximation, which are implemented in **VASP** to perform all calculations [86–90].

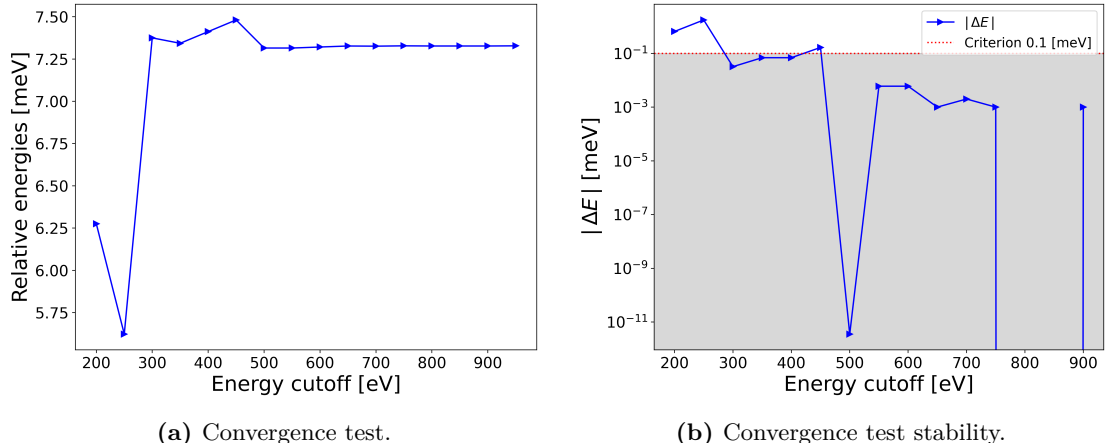
For the calculations in this work, the electronic density convergence criterion is set to 1.0×10^{-6} [eV] in all calculations. On the other hand, the ionic convergence criterion is evaluated based on the total forces acting on the ions (EDIFFG in INCAR) is set differently between different calculations depending on the purpose. For the unit cell relaxation, the ionic convergence criterion is evaluated based on the total forces acting on the ions (EDIFFG in INCAR) is set to 0.005 [eV/Å] to obtain better structural parameters. For supercells calculation using **PBE**, EDIFFG is set to 0.02 [eV/Å], and for **HSE06** it is set to 0.03 [eV/Å]. The difference in ionic convergence values in the supercell comes from the fact that larger systems would be more demanding computationally and would depend on **XC** functional used as well. For instance, for the w-AlN system with 532 atoms, the CPU time used is approximately 1332 times larger than that of a system with 4 atoms using **PBE** with the same **k**-point sampling. Similarly, for a system with 4 atoms using **HSE06**, the CPU time is approximately 240 times larger than that of **PBE** with a **k**-point density = 4.0. Therefore, higher threshold values for ionic relaxation for the supercell through different **XC** functional approximations are used for faster convergence and to save computational time.

Regarding to the convergence tests in this work on w-AlN, they primarily focus on the convergence of total energy, as it serves as the reference quantity for obtaining the results. Nevertheless, total pressure and forces are also considered (see **Figure. A.1** and **Figure. A.2**). These are done for the principal parameters discussed in **Section 4.4**, and they are evaluated for both cases: unit cell and supercell. Additionally, we consider a supercell size convergence test to find the most suitable supercell for the defect calculations.

6.1.1 Unit cell convergence

The unit cell convergence is tested in two parts by following the process described in **Section 5.1**. The first part is testing the energy cutoff with respect to the total energy. It considers two different structures to calculate the relative energy: a reference structure ($E^{tot}[ref]$) which is the relaxed unit cell, and a similar structure ($E^{tot}[dis]$) in which one atom is slightly displaced away from its reference position by 0.01 Å.

The results of the convergence tests and their numerical values are shown in **Figure. 6.2** and **Table. 6.1**, respectively. An energy cutoff of 500 [eV] is found suitable under the consideration of the energy differences $\Delta E \leq 0.1$ [meV], marked by red underline color in **Table. 6.1**. In **Figure. 6.1b**, one can notice that convergence is reached for some smaller values on the gray region above the red line. However, since we want accurate calculations for the bulk properties, these values are not chosen because the energy cutoff of 450 [eV], marked by gray underline color in **Table. 6.1** does not converge under the tiny convergence value utilized. No less important, We also observe that the selected value is the smallest one with higher stability, as shown in **Figure. 6.1**.



(a) Convergence test.

(b) Convergence test stability.

Figure 6.1: Energy cutoff convergence test for the w-AlN unit cell, (a) convergence test respects to the relative energy between reference ($E^{tot}[ref]$) and displacement ($E^{tot}[dis]$) cell ($E_i^{rel} = E_i^{tot}[dis] - E_i^{tot}[ref]$)), (b) convergence test stability evaluate through the relative energies difference between successive values ($\Delta E = E_{i+1}^{rel} - E_i^{rel}$). In the figure, the red horizontal line marks the convergence criterion. Points below this line, located in the gray region, represent cutoff values that meet the convergence condition relative to the previous step.

Table 6.1: Calculated total energy, relative energy (E^{rel}) between reference ($E^{tot}[ref]$) and displacement ($E^{tot}[dis]$) cell, and differences between successive relative energy from the energy cutoff convergence test for w-AlN unit cell, using an energy cutoff range from 200 to 950. In the table, the gray line indicates a value that does not meet the convergence criterion, representing possible instability at lower cutoff values, while the red line marks the selected convergence value.

E_{cut} [eV]	$E^{tot}[ref]$ [eV]	$E^{tot}[dis]$ [eV]	E^{rel} [meV]	$ \Delta E $ [meV]
200	-30.179	-30.172	6.276	0.653
250	-29.736	-29.731	5.623	1.752
300	-29.752	-29.744	7.375	0.032
350	-29.755	-29.748	7.343	0.069
400	-29.782	-29.775	7.412	0.069
450	-29.789	-29.781	7.481	0.166
500	<u>-29.781</u>	<u>-29.774</u>	<u>7.315</u>	<u>0.000</u>
550	-29.780	-29.773	7.315	0.006
600	-29.783	-29.776	7.321	0.006
650	-29.787	-29.779	7.327	0.001
700	-29.789	-29.782	7.326	0.002
750	-29.791	-29.783	7.328	0.001
800	-29.792	-29.784	7.327	0.000
850	-29.792	-29.785	7.327	0.000
900	-29.792	-29.785	7.327	0.001
950	-29.792	-29.785	7.328	—

After determining the optimal energy cutoff, a convergence test for the \mathbf{k} -point density is performed using the established energy cutoff (500 [eV]). The convergence test results are shown in **Figure. 6.2** and **Table. 6.2**, presenting the behavior of total energy as a function of \mathbf{k} -point density and the calculated values, respectively. A \mathbf{k} -points density = 1, equivalent to the Γ point, is under the same criterion for the energy cutoff ($\Delta E \leq 0.1$ [meV]) found to be suitable, as indicated by the blue underline color in **Table. 6.2**. Since the unit cell calculation contains only a few atoms (4), which can be manageable computationally with larger \mathbf{k} -point sampling, the unit cell calculations are performed with a larger \mathbf{k} -point density (-point density = 4), equivalent to a $9 \times 9 \times 6$ \mathbf{k} -point grid centered around the Γ point to guarantee better results for the bulk properties and because this contains more precision than just Γ point, as shown in **Figure. 6.2**. This is also indicated by the red underline color in **Table. 6.2**.

Table 6.2: Calculated total energy, relative energy (E^{rel}) between reference ($E^{tot}[ref]$) and displacement ($E^{tot}[dis]$) cell, and differences between successive relative energy values from the \mathbf{k} -points density test for w-AlN unit cell, using a \mathbf{k} -points range from 1 to 10. In the table, the blue lines indicate the lowest values that meet the convergence criterion, while the red line marks the selected convergence value.

\mathbf{k} -points density	$E^{tot}[ref]$ [eV]	$E^{tot}[dis]$ [eV]	E^{rel} [meV]	$ \Delta E $ [meV]
1	-29.596	-29.588	7.346	0.028
2	-29.773	-29.766	7.318	0.002
3	-29.781	-29.773	7.316	0.001
4	-29.781	-29.774	7.315	0.000
5	-29.781	-29.774	7.315	0.000
6	-29.781	-29.774	7.315	0.000
7	-29.781	-29.774	7.315	0.000
8	-29.781	-29.774	7.315	0.000
9	-29.781	-29.774	7.315	0.000
10	-29.781	-29.774	7.315	—

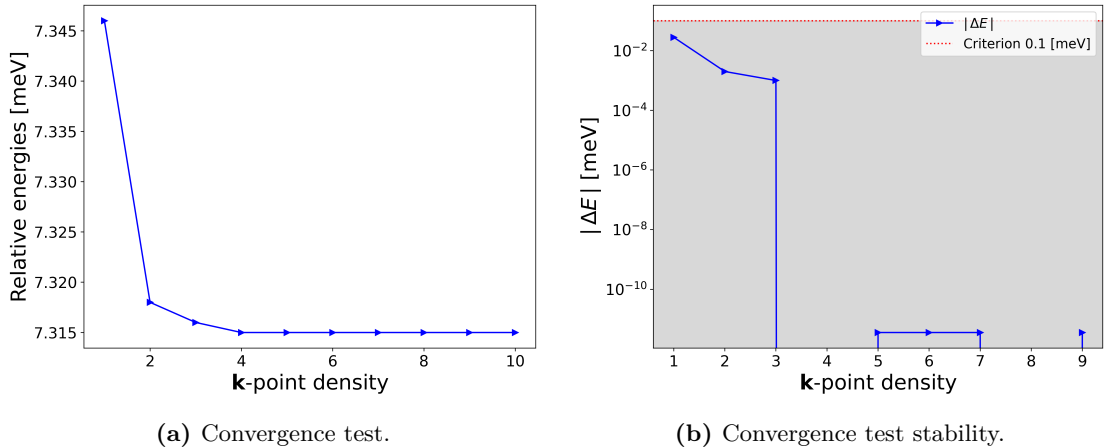


Figure 6.2: \mathbf{k} -points density convergence test for w-AlN unit cell, (a) convergence test respects to the relative energy between reference ($E^{tot}[ref]$) and displacement ($E^{tot}[dis]$) cell ($E_i^{rel} = E_i^{tot}[dis] - E_i^{tot}[ref]$), (b) convergence test stability evaluate through the relative energies difference between successive relative energy values ($\Delta E = E_{i+1}^{rel} - E_i^{rel}$). In the table, the red horizontal line marks the convergence criterion. Points below this line, located in the gray region, represent cutoff values that meet the convergence condition relative to the previous step.

6.1.2 Supercell convergence

For supercell, we first performed a size convergence test to find the appropriate size to used for the defect calculations. It is done by considering a large enough supercell to avoid the self-interaction between repeated defect images due to the periodic boundary conditions, while still being computationally feasible. Moreover, to mitigate self-interaction effects, all supercells are constructed to be as close to a cubic shape as possible, thus utilizing symmetry to minimize artificial self-interaction [120]. After this, we performed convergence tests for energy cutoff and \mathbf{k} -point for the converged supercell size.

The full supercell convergence test (size, energy encut, \mathbf{k} -points) is performed in similar way to the unit cell. In this case, the relative energy is calculated using the difference between total energy of the supercell without defect or perfect supercell ($E^{tot}[\text{Bulk}]$), and the supercell with a nitrogen vacancy defect ($E^{tot}[\mathbf{V}_N]$), following the steps explained in **Section 5.1**. Concerning the size test, it is carried out by investigating different supercell sizes. These are created starting from relaxing the primitive cell and then applying a matrix translation $i \times j \times k$ in each direction of the primitive vector. From the results of the supercell size test, we find that the most suitable supercell sizes are given by the translation matrix $5 \times 5 \times 3$ and $6 \times 6 \times 3$, presented in red color in **Table. 6.3**, which are both converged to under the $\Delta E \leq 4.0$ [meV] criterion, see **Figure. 6.3**.

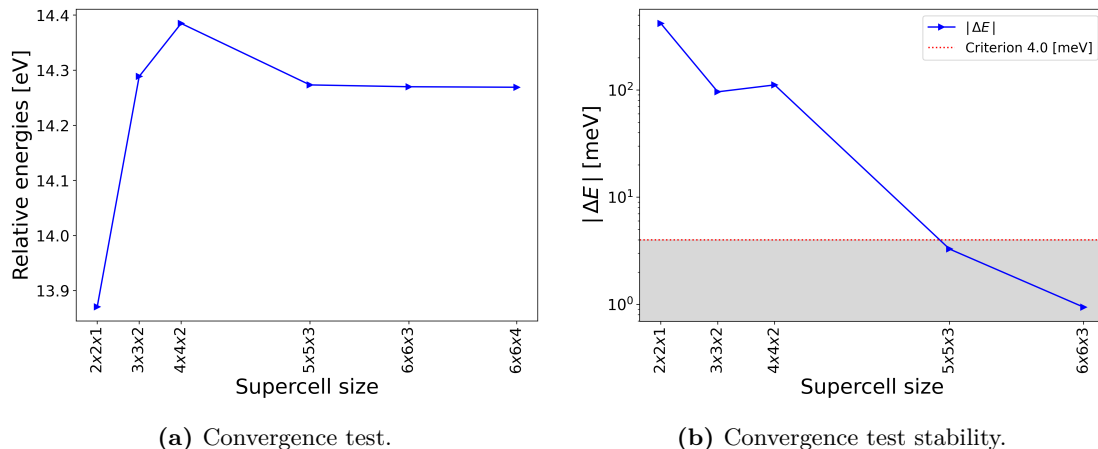


Figure 6.3: Supercell size convergence test for w-AlN, (a) convergence test respects to the relative energy between perfect ($E^{tot}[\text{ref}]$) and with nitrogen vacancy defect ($E^{tot}[\text{dis}]$) supercell ($E_i^{rel} = E_i^{tot}[\mathbf{V}_N] - E_i^{tot}[\text{Bulk}]$), (b) convergence test stability evaluated through the relative energies difference between successive values ($\Delta E = E_{i+1}^{rel} - E_i^{rel}$). In the figure, the red horizontal line marks the convergence criterion. Points below this line, located in the gray region, represent cutoff values that meet the convergence condition relative to the previous step.

Table 6.3: Calculated total energy, relative energy (E^{rel}) between perfect ($E^{tot}[\text{Bulk}]$) and with nitrogen vacancy defect ($E^{tot}[\mathbf{V}_N]$) supercell, and differences between successive relative energy from the size convergence test for w-AlN supercell. In the table, the red lines mark the selected convergence values.

Size	N	$E^{tot}[\text{Bulk}]$ [eV]	$E^{tot}[\mathbf{V}_N]$ [eV]	E^{rel} [eV]	$ \Delta E $ [eV]
$2 \times 2 \times 1$	16	-119.054	-105.183	13.871	0.418
$3 \times 3 \times 2$	72	-535.751	-521.462	14.289	0.096
$4 \times 4 \times 2$	128	-952.435	-938.050	14.385	0.112
$5 \times 5 \times 3$	300	-2232.302	-2218.029	14.273	0.003
$6 \times 6 \times 3$	432	-3214.543	-3200.272	14.270	0.001
$6 \times 6 \times 4$	576	-4286.069	-4271.800	14.269	

Furthermore, since we are particularly interested in the deeper analysis of the **KS** eigenvalue distribution and their corresponding orbital localization factors, the selected supercell sizes are also tested in relation to these factors. This analysis is conducted for both **XC** functionals (**PBE** and **HSE06**). The orbital localization factors for the **KS** eigenvalue distribution are presented in **Figure. 6.5** and **Figure. 6.5** for **PBE** and **HSE06**, respectively. The localization factors are represented by the color bar, with yellow/green indicating localized states, which have effective localization factors three times or more larger than the delocalized states in purple, which have the lowest localization factor.

We begin by analyzing the results from the **PBE** calculations, noting that considerable **KS** states are missing, while some have shifted from their energy positions around and in between the **VBM** and **CBM**, when transitioning from a $6 \times 6 \times 3$ to a $5 \times 5 \times 3$ supercell (see **Figure. 6.4**). Where this behavior may represent some missing electronic interaction, along with an artificial self-defect interaction. Next, we analyze the **HSE06** calculations, which yield similar results for both supercell sizes concerning to the **KS** distribution. Similarly, no considerable missing states are observed around the **VBM** and **CBM** as seen in the **PBE** results (see **Figure. 6.5**). This outcome is somewhat expected because **HSE06** incorporates more accurate physical interactions by accounting a part of the exact **XC** functional. The last observation reinforces the previous argument made for **PBE** to explain this behavior while also highlighting that the effect is primarily due to some missing of physical interaction rather than an artificial self-defect interaction for the two consider supercell sizes. Moreover, by comparing **Figure. 6.4b** and **Figure. 6.5b**, we find that for the **PBE** calculations, it is necessary to choose a larger supercell ($6 \times 6 \times 3$) to achieve more accurate representations of individual **KS** states. In contrast, for **HSE06**, a smaller supercell ($5 \times 5 \times 3$) properly captures the behavior of the **KS** eigenvalue distribution. This is particularly beneficial, as **HSE06** is significantly more computationally expensive than **PBE**.

The above result is quite important because it highlights the need to choose a larger supercell for the **PBE** functional compared to **HSE06** in order to capture similar results. Additionally, it provides certainty that the **KS** localized states located between the band edges are correctly captured for the chosen supercell sizes. This is particularly crucial to be able to estimate correctly the electronic excitation transition between these states. Additionally, a correct description of the single **KS** state would lead to a more accurate ground state total energy.

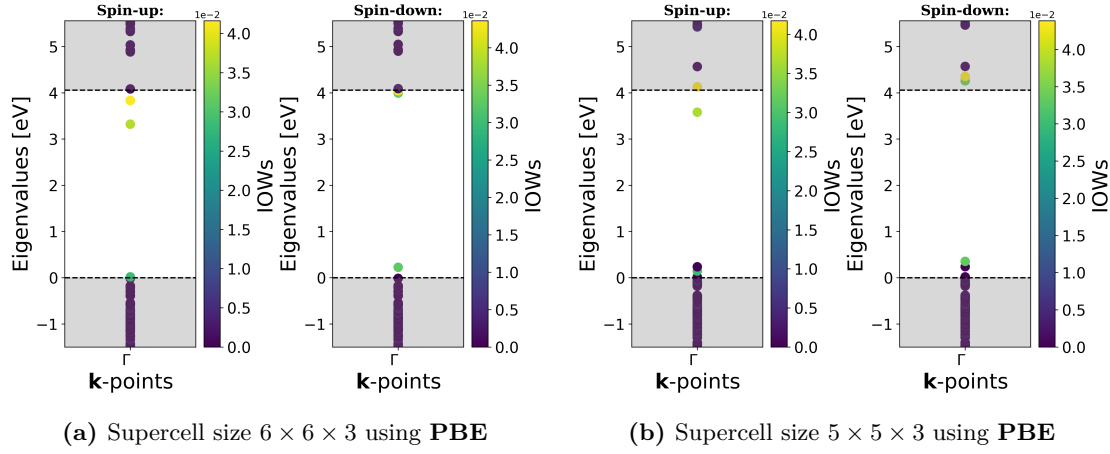


Figure 6.4: Orbital localization factors of the KS eigenvalue distribution for the neutral nitrogen vacancy (V_N^0), calculated using **PBE** at the Γ -point: (a) for a supercell size of $6 \times 6 \times 3$, and (b) for a supercell size of $5 \times 5 \times 3$. In the figure, the orbital localization factors are represented by the color bar, with yellow/green indicating localized states and purple indicating delocalized states.

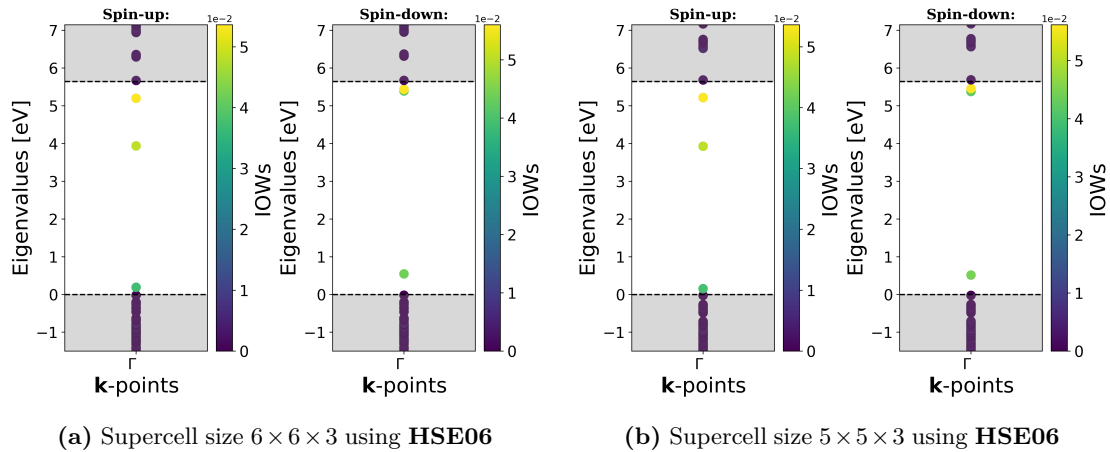


Figure 6.5: Orbital localization factors of the KS eigenvalue distribution for the neutral nitrogen vacancy (V_N^0), calculated using **HSE06** at the Γ -point: (a) for a supercell size of $6 \times 6 \times 3$, and (b) for a supercell size of $5 \times 5 \times 3$. In the figure, the orbital localization factors are represented by the color bar, with yellow/green indicating localized states and purple indicating delocalized states.

For the energy cutoff and \mathbf{k} -point density, the total energy as function of energy cutoff and \mathbf{k} -point density results are shown in **Figure. 6.6** and **Figure. 6.7**, respectively. While the calculated data can be found in **Appendix A** (**Table. A.1** and **Table. A.2**). First, the energy cutoff results are analyzed. They exhibit an apparent convergence value for an energy cutoff of 500 [eV] (see **Figure. 6.6a**). However, with further examination, we find significant fluctuations across all energy cutoff values (see **Figure. 6.6b**), with only two values (500 and 550 [eV]) reaching the convergence criterion, which is the same as that used for the size convergence test ($\Delta E \leq 4.0$ [meV]). While we do not have a precise explanation for this behavior, it may be related to the differences in numerical error for

the total energy arising from the supercell without the defect ($E^{tot}[\text{bulk}]$) and with the defect ($E^{tot}[\mathbf{V}_N]$), which do not cancel out, leading to notable fluctuations.

By taking into account the last results, we decide to choose different values of 520 and 500 [eV] for each functional, **PBE** and **HSE06**, respectively. These values are selected from a range of convergence values (500 – 550) [eV]. For **PBE**, a slightly larger value is chosen because it is less computationally demanding than **HSE06**. Furthermore, it is well known that a greater number of plane waves should, in theory, yield more accurate results.

Finally, the \mathbf{k} -point density results are discussed. It shows good convergence for a \mathbf{k} -point density equal to or greater than two (see **Figure. 6.7a**), along with perfect stability, as higher density values yield a smaller energy difference, which is the ideal numerical expectation (see **Figure. 6.7b**). Therefore, we decide to use a \mathbf{k} -point density = 2 for **PBE** calculations, which corresponds to a $2 \times 2 \times 2$ \mathbf{k} -point grid centered around the Γ point. On the other hand, for **HSE06**, we select the smallest \mathbf{k} -point density (\mathbf{k} -point density = 1), equivalent to the Γ point. This decision is supported by two reasons. The first reason is related to the fact mentioned earlier and also through the full supercell convergence discussion that **HSE06** is more computationally demanding. Moreover, as the size and number of \mathbf{k} -point samples increase, this factor rises drastically. For example, when transitioning from a \mathbf{k} -point density of 1 to 2 for a simpler **PBE** calculation, the CPU time is approximately 4 times larger for the same size supercell. The second reason is that the numerical accuracy when only using the Γ point (\mathbf{k} -point density = 1) is not drastically larger (see **Figure. 6.6b**); it is around 10 [meV], which is an acceptable value for a large supercell using **HSE06**.

For the $\mathbf{G}_0\mathbf{W}_0$ calculations, a smaller supercell of $4 \times 4 \times 2$ with only Γ point \mathbf{k} -point sampling was chosen, and ionic relaxation is not considered. As mentioned before, the $\mathbf{G}_0\mathbf{W}_0$ just a one-shot electronic relaxation, since **GW** is extremely more computationally expensive in comparison with **DFT**.

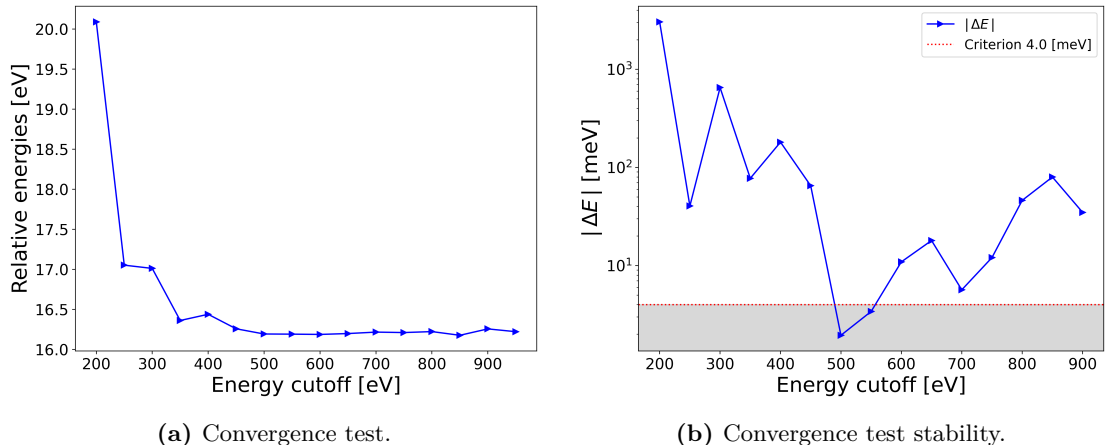


Figure 6.6: Energy cutoff convergence test for w-AlN supercell, (a) convergence test respects to the relative energy between perfect ($E^{tot}[\text{ref}]$) and with nitrogen vacancy defect ($E^{tot}[\text{dis}]$) supercell ($E_i^{\text{rel}} = E_i^{\text{tot}}[\mathbf{V}_N] - E_i^{\text{tot}}[\text{Bulk}]$), (b) convergence test stability evaluated through the relative energies difference between successive values ($\Delta E = E_{i+1}^{\text{rel}} - E_i^{\text{rel}}$). In the figure, the red horizontal line marks the convergence criterion. Points below this line, located in the gray region, represent cutoff values that meet the convergence condition relative to the previous step.

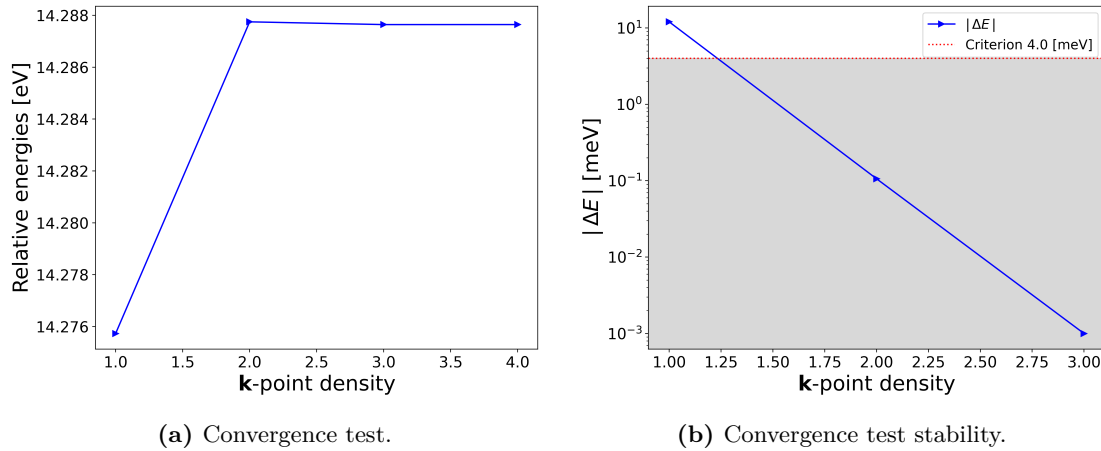


Figure 6.7: \mathbf{k} -point density convergence test for w-AlN supercell, (a) convergence test respects to the relative energy between perfect ($E^{tot}[ref]$) and with nitrogen vacancy defect ($E^{tot}[dis]$) supercell ($E_i^{rel} = E_i^{tot}[\mathbf{V}_N] - E_i^{tot}[\text{Bulk}]$), (b) convergence test stability evaluated through the relative energies difference between successive values ($\Delta E = E_{i+1}^{rel} - E_i^{rel}$). In the figure, the red horizontal line marks the convergence criterion. Points below this line, located in the gray region, represent cutoff values that meet the convergence condition relative to the previous step.

6.2 Bulk properties and electronic structure of w-AlN

As mentioned earlier, to determine the structural parameters and bulk properties of the w-AlN, the convergence criterion for electronic density relaxation is set to EDIFF = 1.0×10^{-6} , eV, while the ion total force relaxation is set to EDIFFG = -0.005 , eV/Å. An energy cutoff of 500 [eV] and \mathbf{k} -point density of 4.0 are also utilized in the calculations. The **Table. 6.4** shows the experimental lattice structure parameter at room temperature 300 [K] and that found herein using **PBE** and **HSE06**. **PBE** overestimates the lattice parameter with a relative error around 0.5% and 0.7% for a and c , respectively, while **HSE06** underestimates the lattice parameter with a smaller relative error of 0.2% for both. Moreover, one must keep in mind that **DFT** is considered a 0 [K] calculation, and increasing the temperature would normally cause a small stretch of the lattice parameter. Thus, the **HSE06** result could fit very well the experimental data by extrapolating to higher temperature.

Table 6.4: Bulk properties of w-AlN calculated using PBE and HSE06 approximation and experimental result at room temperature 300 [K]. See the Ref. [121] for band gap values calculated through several first-principles methods

Method	a [Å]	c [Å]	Volume [Å ³]	E_{gap} [eV]
Experimental	3.110 ^[40, 41]	4.980 ^[40, 41]	41.714	6.015 ^[122] -6.040 ^[123] -6.200 ^[42]
PBE	3.128	5.016	42.527	4.056
HSE06	3.103	4.968	41.446	5.644

In **Table**. 6.4, the experimental from literature and theoretically calculated band gap energies (E_{gap}) are presented as well. Here, the theoretical band gaps are estimated by calculating the difference in energy between the highest occupied and lowest unoccupied **KS** orbital. The two **DFT** methods (**PBE** and **HSE06**) underestimate the band gap compared to experiment around 34% and 9%, respectively. This underestimation of band gap, it is a very well known problem in **DFT** calculation, which is called as the band gap problem. This common problem comes from the missing of some physics interaction in the **XC** functional approximation and the no cancel out Hartree self-energy interaction [124–129]. Whereas, the **HSE06** includes a portion of the exact Hartree-Fock exchange to considerably reduce the self-energy interaction, making this more accurate [127]. Either way, the two methods agree with the experiment in confirming that w-AlN has a direct band gap at the Γ -point [42, 122, 123], which are shown in **Figure**. 6.8 that contain the band electronic structure and **DOS** for w-AlN. Note: In **Figure**. 6.8, the band structure and **DOS** are plotted using **HSE06**, meaning that it would underestimate the E_{gap} by around 0.556 [eV].

On the other hand, we observe that the band gap from experimental results has different values in the literature: 6.015 [122], 6.040 [123], and 6.200 [42] in [eV]. We find that this variation arises from various experimental factors, such as crystal size, crystalline alignment, and film thickness. Additionally, it also depends on the measurement method employed, as detailed in **Ref.** [122].

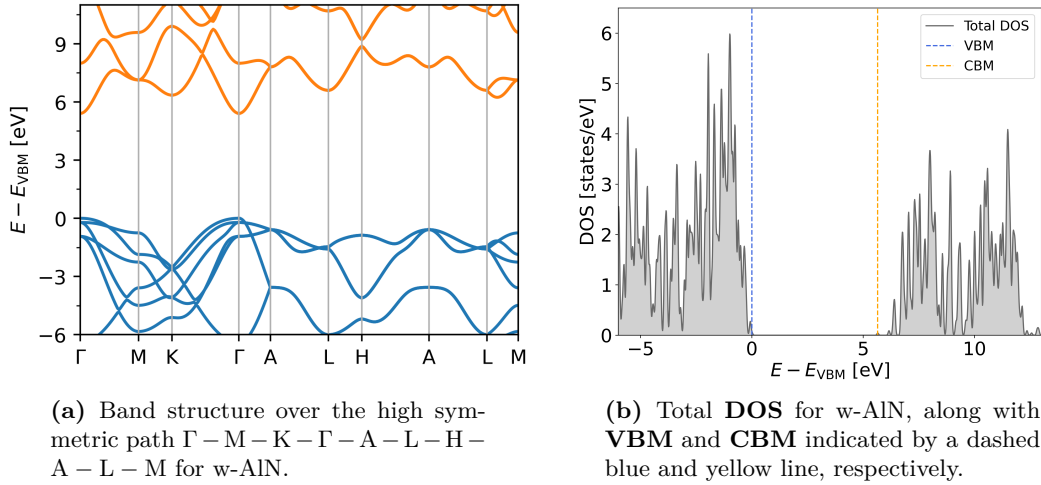


Figure 6.8: Band structure and total **DOS** for w-AlN using **HSE06**.

6.3 Defect analysis: native, impurity and complex

This section analyzes the native, impurity, and complex defects investigated as candidates for a **QT**. The first analysis is based on the initial selection of interesting defects from the literature review to further explore their electronic configuration properties. The second analysis is made by calculating formation energy diagrams to find the thermodynamically stable defects, stable defect charge states and **TTLs**. This step is performed using **PBE**, with a supercell size of $6 \times 6 \times 3$, a **k**-point density of $2 \times 2 \times 2$, and an energy cutoff of 520 [eV]. The third analysis is carried out to filter the most suitable defects and defect charge states for **QT** through the examination of **KS** eigenvalue distribution and their corresponding orbital localization factors. The

final analysis examines the spin electronic configuration properties of the filtered defect charge states to select the most promising candidates as potential point defect platforms for **QT**. This final analysis is conducted using **HSE06**, with a supercell size of $5 \times 5 \times 3$, employing only the Γ point and an energy cutoff of 500 [eV]. On top of that the final analysis is completed by carrying out a $\mathbf{G}_0\mathbf{W}_0$ calculation to further estimate the spin electronic configuration and compare them with the results from **DFT**. For $\mathbf{G}_0\mathbf{W}_0$ calculations we used a smaller supercell size of $4 \times 4 \times 2$ with only the Γ point and energy cutoff 500 [eV], as was discussed in **Section 6.1.2**.

6.3.1 Literature study: Initial defect selection

As was discussed in **Section 2.6.2**, the selected defects are chosen based on practicality, literature findings, and comparison with known defects in materials like diamond and silicon, which demonstrate desirable properties such as spin qubits and single-photon emission. These defects include six types, primarily focusing on simple native defects: nitrogen vacancy defect (V_N), aluminum vacancy (V_{Al}), and aluminum antisite (Al_N). There is one impurity defect: carbon substitutional defect (C_N). Additionally, two complex defects are considered: the divacancy ($V_N V_{Al}$) and the double substitutional carbon, or carbon dimer ($C_N C_{Al}$).

6.3.2 Formation energy diagram and thermodynamic transition levels

The formation energies for the different point defects are calculated using **Equ.** (5.4). It would need three components : the total energy with and without defect, finite size correction for charged defects, the chemical potential of the elements that have been considered, and the formation energy of AlN. The total energies are obtained by running a **DFT** calculation including ionic relaxation. The finite error correction is estimated using the package **PYDEFECT**, which has to be passed the dielectric tensor, or the perpendicular (ϵ_{\perp}) and parallel (ϵ_{\parallel}) component to the c-axi. They are determined using linear-response **DFT** perturbation theory, with numerical values of $\epsilon_{\perp} = 8.228$ and $\epsilon_{\parallel} = 9.750$ relative to the dielectric constant in vacuum, which are consistent with the literature [130, 131]¹. Then, the chemical potentials are computed by running a **DFT** calculation to determine the total energy of the most stable phases of the corresponding elements, divided by the number of atoms. For this study, the relevant elements are aluminum (Al), nitrogen (N), and carbon (C). The chemical potentials for carbon and nitrogen are computed using metallic aluminum and the diamond phase, respectively. While the nitrogen potential is calculated using the gas phase (N_2). The computed numerical values are presented in **Table. 6.5**. Finally, the formation energy of w-AlN is calculated using chemical potential of Al and N calculated before, resulting in $E^f[2AlN] = -5.650$ [eV].

The total energy and finite error correction are shown in the **Table. 6.6**

Table 6.5: Chemical potentials at the upper limit of the constituent elements are used in the calculation of formation energies.

Element X	μ_X [eV]
Al	0

¹In this thesis, we will not discuss the **DFT** perturbation theory calculations further, as they are beyond the scope of this work. However, additional details about linear-response **DFT** perturbation theory are presented in Ref. [132].

Al	-3.738
N	-8.326
C	-9.224

The formation energies are shown **Figure. 6.9** within **PBE** approximation, for the different selected point defects: V_N , V_{Al} , Al_N , C_N , $V_{Al}V_N$, and C_NCaI . They are calculated for two different limits, Al-rich and N-rich condition, by varying the Fermi level between $0 \leq E_F \leq E_{gap}$.

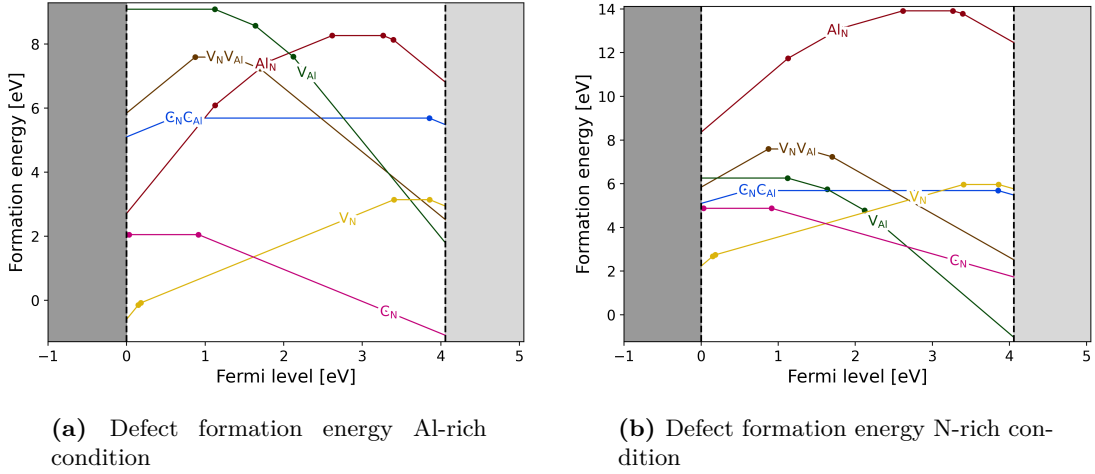


Figure 6.9: Defect formation energies using **PBE** for: V_N , V_{Al} , Al_N , C_N , $V_{Al}V_N$, and C_NCaI

A metastable state is found for the nitrogen vacancy V_N in the charge $q = -1$. The metastable state has spin configuration $s = 1$, which is illustrated in **Figure. 6.10**, along with the stable one $s = 0$. The energies of the metastable $s = 1$ and stable $s = 0$ states are found to be quite similar under the **PBE** approximation with 0.08 [eV] lower, which have been corroborated in the reference Ref. [133, 134] using different **XC** energy approximation, reporting values 0.055 and 0.1 [eV]. Additionally, in the Ref. [133], they have proposed those as “mechanics” quantum bit using the two different spin state, giving the scenario to manipulated and control through changed in external strain condition.

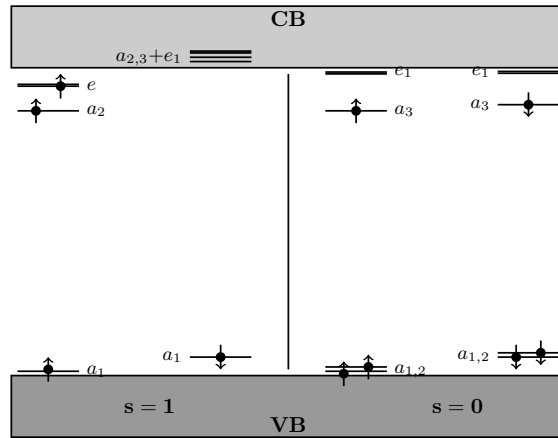


Figure 6.10: Metastability of V_N^- in the two different spin electronic configurations: $s = 1$ and $s = 0$, with the specified localized orbitals a and e denoting singly and doubly degenerate orbital states, respectively. These spin configurations are constructed based on the **KS** eigenstate distribution and their corresponding orbital localization factors (Figure. A.3).

It is also observed for divacancy defect $V_{Al}V_N$ a low stability in spin states of the thermodynamic stable charged $q = 0$ and $q = +2$, both present two different spin configuration $s = 0, 1$ and $s = 1, 3/2$. To secure the most stable spin state is performed a **HSE06** calculation on them, finding quite close energies for the different spin configuration for each charged, $q = 0$ is found $s = 1$ most stable with a lower energy around 0.039 [eV], while $q = +2$ shows $s = 1$ most stable with an energy 0.90 [eV] lower. More importantly, these states do not present **KS** and **KSOLF** distribution suitable electronic conserving spin excitation, see the result in Figure. A.4. Regarding the Ref. [133], they have found $s = 0$ and $s = 3/2$ for each charged $q = +2$ and $q = 0$ this time within **GGA**. These behaviors may be indicated for deep level spin qubit in $V_{Al}V_N$ defect would no ideal in these two charged state, since this can introduce decoherence by fliting from one spin state to other.

Table. 6.6 presents the thermodynamically stable charge states of each defect and their corresponding spin states, total energy, correction energy, and formation energy value without correction under the situation where chemical potentials of the elements are set at their standard total energy by atom and the electron chemical potential is located at energy zero, for each of them. These results are compared with the available literature, verifying if the stable charge and spin states are consistent [133–139]. Note that the spin state is calculated as $s = (N_\uparrow - N_\downarrow)/2$, where N_\uparrow and N_\downarrow are the number of electrons with spin up and down, respectively.

Table 6.6: Formation energies and electronic spin states of the selected defects using **PBE**.

Defect X^q	Spin	$E^{tot}[X^q]$ [eV]	$E^{corr}[X^q]$ [eV]	$E_0^f[X^q, \mu_i]$ [eV]
V_N^{+3}	0	-3224.770	1.161	1.068
V_N^{+2}	1/2	-3218.000	0.516	1.863
V_N^{+1}	0	-3211.450	0.125	2.437

V_N^0	1/2	-3201.946	0.000	5.965
V_N^{-1}	0	-3192.258	0.146	9.678
V_{Al}^0	3/2	-3203.414	0.000	9.085
V_{Al}^{-1}	1	-3196.499	0.146	10.026
V_{Al}^{-2}	1/2	-3189.338	0.555	11.212
V_{Al}^{-3}	0	-3181.954	1.229	12.617
Al_N^{+3}	1/2	-3225.332	1.286	4.246
Al_N^{+2}	1	-3217.529	0.588	6.072
Al_N^{+1}	3/2	-3209.311	0.157	8.314
Al_N^0	1	-3200.562	0.000	11.088
Al_N^{-1}	1/2	-3191.431	0.112	14.242
Al_N^{-2}	0	-3182.443	0.493	17.255
C_N^{+1}	1	-3218.399	0.129	4.714
C_N^0	1/2	-3212.261	0.000	4.875
C_N^{-1}	0	-3205.509	0.138	5.651
$(V_N V_{Al})^{+2}$	1	-3207.866	0.410	8.259
$(V_N V_{Al})^0$	1	-3193.758	0.000	10.416
$(V_N V_{Al})^{-1}$	1/2	-3186.630	0.189	11.568
$(V_N V_{Al})^{-2}$	0	-3179.408	0.644	12.813
$(C_N C_{Al})^{+1}$	1/2	-3220.790	0.115	7.808
$(C_N C_{Al})^0$	0	-3214.110	0.000	8.512
$(C_N C_{Al})^{-1}$	1/2	-3204.436	0.155	12.210

Table. 6.7 presents the **TTLs** and estimated ionization energy ($E_{ion}(q/q')$) for each charge state transition levels. The last one is calculated by subtracting the transition level $\varepsilon(q/q')$ [eV] to the **CBM** reference with respect to **VBM**, which is equivalent to $E_{ion}(q'/q) = E_{gap} - \varepsilon(q/q')$.

Table 6.7: Thermodynamics charge **TTLs** and ionization energies for different defect calculated using **PBE**: V_N , V_{Al} , Al_N , C_N , $V_{Al}V_N$, and $C_N C_{Al}$

Defect X	Charge transition	$\varepsilon(q/q')$ [eV]	$E_{ion}(q'/q)$ [eV]
V_N	(+3/+2)	0.150	3.906

	(+2/+1)	0.182	2.236
	(+1/0)	3.404	0.652
	(0/-1)	3.858	0.198
V _{Al}	(0/-1)	1.122	2.934
	(-1/-2)	1.638	2.418
	(-2/-3)	2.120	1.936
Al _N	(+3/+2)	1.127	2.929
	(+2/+1)	1.811	2.245
	(+1/0)	2.617	1.442
	(0/-1)	3.266	0.790
C _N	(-1/-2)	3.394	0.662
	(+1/0)	0.032	4.024
	(0/-1)	0.914	3.142
V _N V _{Al}	(+2/0)	0.874	3.182
	(0/-1)	1.341	2.715
	(-1/-2)	1.700	2.356
C _N C _{Al}	(+1/0)	0.588	3.498
	(0/-1)	3.852	0.204

6.3.3 Selected defect charge states

Due to the presence of various broad defects, we have selected several attractive defect charge states candidates for further study. These are shown in **Table.** 6.8. These candidates were chosen based on three different criteria, which are presented below.

Selection criteria:

1. Higher spin state $\mathbf{s} \geq 1/2$
2. A proper single **KS** orbitals distribution
3. Effective localization factor of the single **KS** orbitals

The first criterion is to identify a paramagnetic electronic state, which can be initialized either by absorbing a photon or via electron spin resonance, and manipulated by splitting it into sublevels that facilitate a well-defined transition path between the ground and excited states. The second criterion, which is related to the first, is that the single **KS** orbitals must have a suitable distribution to promote or excite an electron

from the ground state to an excited state while ensuring spin conservation. The final criterion is essential to ensure that the associated **KS** orbitals are well localized, leading to isolated states that exhibit minimal interaction with the surrounding environment [9, 11, 36, 110].

Table 6.8: Selected charged defects and their corresponding spin states.

Defect X^q	Spin
V_N^0	$1/2$
V_{Al}^0	$3/2$
V_{Al}^{-1}	1
V_{Al}^{-2}	$1/2$
Al_N^{+2}	1
Al_N^{+1}	$3/2$
Al_N^0	1
C_N^0	$1/2$
$(V_N V_{Al})^{-1}$	$1/2$
$(C_N C_{Al})^{+1}$	$1/2$

6.3.4 Electronic configuration of selected defect charge states

Point defect states require certain characteristic properties to be used in **QT** applications; some of these properties have been briefly discussed in the previous section (**Section 6.3.3**). For further reading, see Ref. [36]. Among these properties, a fundamental one related to experimental measurements is an adequate (E_{ZPL}) value, which must be sufficiently large to prevent thermodynamic excitation while also being experimentally detectable. An acceptable E_{ZPL} value is considered herein to be larger than 0.5 [eV]. Hence, in this subsection, we will try to estimate the **ZPL** emission values for the preselected defect state charge states (see **Table. 6.8**).

The process for calculating **ZPL** energies involves examining the **KS** distribution of localized deep level states to identify the appropriate electronic excitation transitions between the ground and excited states, followed by calculations using **Equ.** (5.22). In this context, the ground state represents the total energy of the final configuration of the defect after ionic relaxation, while the excited state is obtained by promoting one electron from the highest occupied localized state to the lowest unoccupied localized state through a constrained **DFT** calculation with ionic relaxation. Furthermore, since **PBE** tends to underestimate and **HSE06** tends to overestimate the **ZPL** energy (E_{ZPL}), the electronic excitation transitions are calculated using both **XC** approximations in an attempt to find a more appropriate range for the **ZPL** emission values for comparison with experimental results.

The analysis of the selected defect charge states will be divided into two portions. In the first portion, we will focus on the native defects, followed by a second portion that considers the selected impurity and complex charged defects. Throughout this discussion, we will utilize three concepts to represent the electronic spin configuration of **KS** states: localized states, apparently localized states, and delocalized states. The term "localized" state refers to states with a higher orbital localization factor, represented in yellow and green in the **KS** orbital localization factor plot for both approaches: **IPRs** and **IOWs**. The term "apparently localized state" indicates states that exhibit a higher orbital localization factor in one approach while appearing delocalized in the other. Finally, the term "delocalized state" consists of those states with a lower localization factor and is represented in purple.

Selected charge states of native defects

This first portion will consider the native charge defects, starting with **V_N** in the charge state $q = 0$. Next, we will examine **V_{Al}** in three different charge states $q = 0, -1, -2$. Finally, **Al_N** with the charge states $q = +2, +1, 0$.

The **KS** eigenvalue distribution and their corresponding orbital localized factor through **IPRs** and **IOWs** are presented in **Figure. 6.12** for **V_N⁰**. We have identified two possible excitation transitions between the localized states: a shorter transition for spin up from the single orbital (a_2) to the double degenerate state (e_1), and a longer transition for spin down from the single orbital (a_1) to (a_2). These transitions are schematically illustrated in **Figure. 6.11**. Each transition is considered individually, as standard **DFT** theory cannot handle multi-determinantal systems; thus, the constrained excitation state can only correspond to a single excitation determinant. The **ZPL** energies estimated for the longer and shorter transitions with **PBE** $E_{ZPL} = 0.169$ [eV] and $E_{ZPL} = 3.417$ [eV]. For **HSE06**, we are only able to estimate the energy for the longer transition with $E_{ZPL} = 3.775$ [eV] value, as the shorter transition does not reach the ionic and electronic relaxation. The last result is somewhat unexpected because these states exhibit a very well-localized **KS** orbital factor with both methods used, suggesting that they should be able to promote excitation of an electron between a_2 and e_1 as calculated for **PBE**; See **Figure. 6.12**, with yellow and green colors indicating the localized states. Nonetheless, we suspect that this discrepancy may be related to the fact that **DFT** is a ground state theory and is not the most appropriate method for considering excited states.

These values are presented in **Table. 6.9**, along with the total energies of the ground and excited states for each spin channel considered, and the corresponding wavelengths (λ) (in [nm]), which are often used to compare experimental results with these **DFT** calculations. Note: The wavelengths (λ) are calculated using the energy-wavelength relation ($\lambda = hc/E_{ZPL}$), where h is the Planck constant and c is the speed of light.

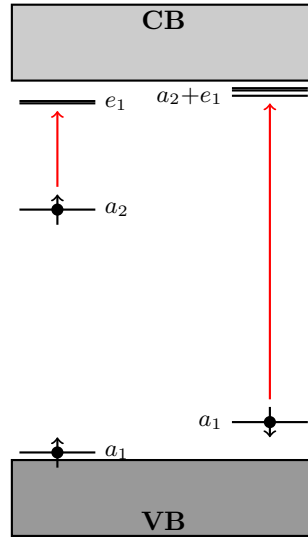


Figure 6.11: KS eigenvalues of the localized states for V_N in the neutral charge state $q = 0$, with the specified orbitals a and e denoting singly and doubly degenerate orbital states, respectively.

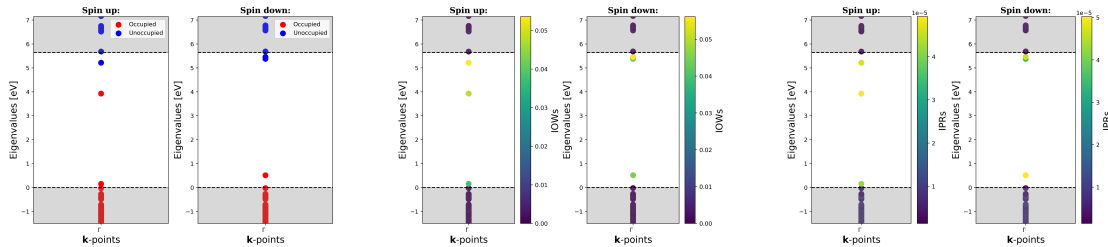


Figure 6.12: KS eigenvalue distribution and corresponding orbital localization factors analyzed using the IPRs and IOWs methods for V_N^0 , calculated with **HSE06** at the Γ point. Orbital localization factors are indicated in yellow/green for localized states and purple for delocalized states.

Table 6.9: Ground (E_g) and excited (E_e) states calculated using **PBE** and **HSE06** for V_N in the selected charge state $q = 0$, along with the corresponding ZPL line for the selected spin channel, given in units of energy and wavelength.

Charge	Channel	XC	E_g [eV]	E_e [eV]	E_{ZPL} [eV]	E_{ZPL} [nm]
$q = 0$	\uparrow	PBE	-3201.777	-3201.608	0.169	7336.342
	\downarrow	PBE	-3201.777	-3198.360	3.417	362.845
		HSE06	-2605.058	-2601.283	3.775	328.434

Meanwhile, the **KS** eigenvalues distribution and its local factor are given in **Figure 6.14** for V_{Al} in their three selected charge states V_{Al}^0 , V_{Al}^{-1} , and V_{Al}^{-2} . A schematic

representation of the spin configuration is provided in **Figure. 6.13**, illustrating localized (black), apparently localized (green), and delocalized (blue) states for the selected charge states V_{Al}^0 , V_{Al}^{-1} , and V_{Al}^{-2} . we identify single excitation electronic transitions with a spin down channel for all states. The transition in V_{Al}^0 occurs by promoting an electron from the highest occupied state (a_1) to the lowest unoccupied state (a_2), yielding a **ZPL** energy of $E_{\text{ZPL}} = 0.821$ [eV]. while, for V_{Al}^{-2} , the transition occurs by promoting an electron from a_3 to a_4 , resulting in a **ZPL** energy of $E_{\text{ZPL}} = 0.806$ [eV]. See in **Table. 6.10** with the details of the ground and excited energy state. Both values are calculated only within the **PBE** approximation, because we are unable to estimate them with **HSE06** due to failure to reach convergence criteria for the excite electronic configuration. This may indicate that a_1 apparently localized state is not truly localized in the case V_{Al}^0 . Unfortunately, we cannot make an estimation of **ZPL** energy for V_{Al}^{-1} related to the electronic excitation from a_2 to (a_3) , sugesting that a_3 must be delocalized state.

On the other hand, it has been reported in the literature that V_{Al}^{-2} may be a stable charge state around a temperature of 10 [K], based on **DFT** calculations combined with experimental data, where an emission peak at 2.782 [eV] has been attributed to this charge state [140]. This, along with the distribution of the localized states, suggests that V_{Al}^{-2} is a promising candidate for **SPE** or spin qubit applications.

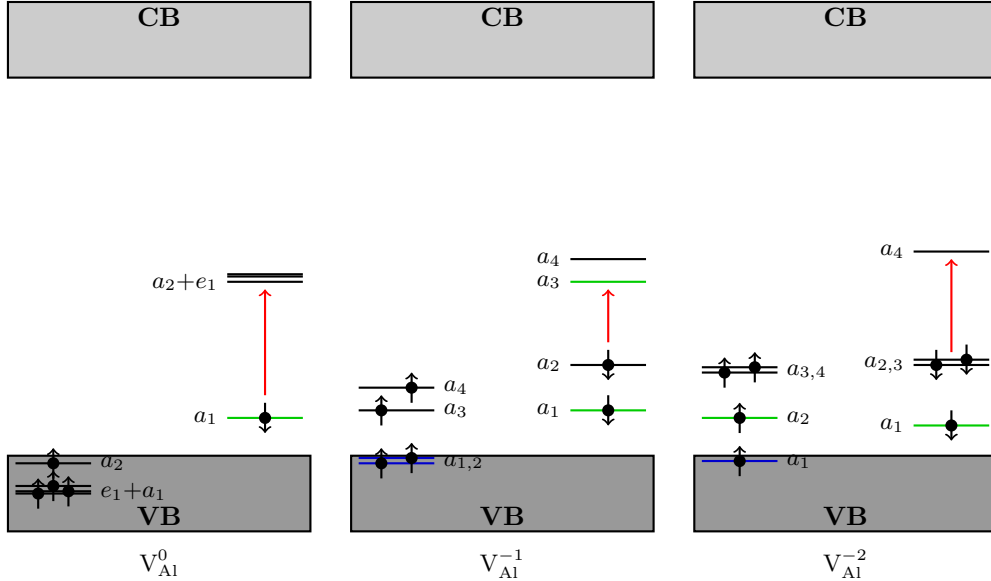
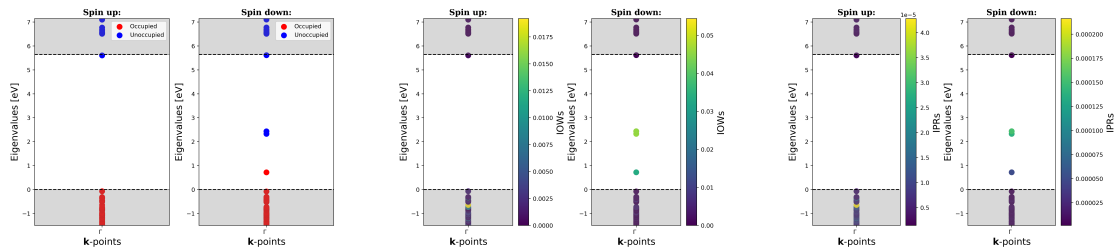


Figure 6.13: KS eigenvalues of the localized (black), apparently localized (green), and delocalized (blue) states for V_{Al} in the charge states $q = 0, -1, -2$, with the specified orbitals a and e denoting singly orbital state and doubly degenerate orbital state, respectively.



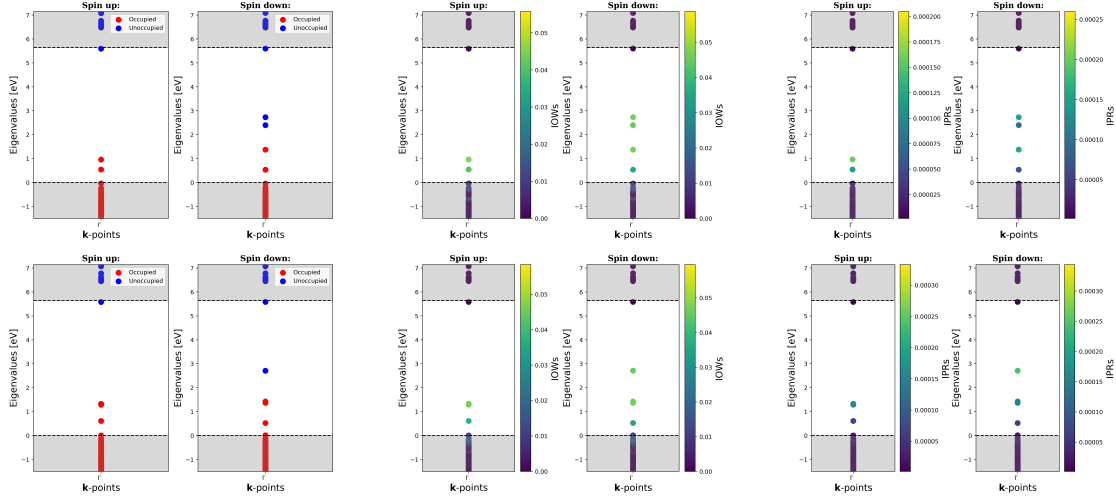


Figure 6.14: KS eigenvalue distribution and corresponding orbital localization factors analyzed using the **IPRs** and **IOWs** methods for V_N^0 (top), V_N^{-1} (middle), and V_N^{-2} (bottom), calculated using **HSE06** at the Γ point. Orbital localization factors are indicated in yellow/green for localized states and purple for delocalized states.

Table 6.10: Ground (E_g) and excited (E_e) states calculated using **PBE** for V_{Al} in the charge state $q = 0, -2$, along with the corresponding **ZPL** line for the selected spin channel, given in units of energy and wavelength.

Charge	Channel	XC	E_g [eV]	E_e [eV]	E_{ZPL} [eV]	E_{ZPL} [nm]
$q = 0$	\downarrow	PBE	-3203.274	-3202.453	0.821	1510.160
$q = -2$	\downarrow	PBE	-3189.159	-3188.353	0.806	1538.265

In the Al_N defect, the charge state Al_N^{+2} shows two possible excitation transitions: a shorter one with spin up from the doubly degenerate state e_1 to the single orbital a_2 , and a longer one with spin up from the single orbital a_1 to a_2 . For the other two charge states Al_N^{+1} and Al_N^0 , there is one transition with spin down. For Al_N^{+1} , the transition is larger, going from the single orbital a_1 to the doubly degenerate e_1 , while for Al_N^0 , it is shorter, moving from the single orbital a_3 to the doubly degenerate orbital e_1 as well, as shown in **Figure. 6.15**. The estimated **ZPL** energies for these transitions are presented in **Table. 6.11** using two different approximations, with the exception of Al_N^0 , for which we are only able to provide an estimate using **PBE**.

These three charge states look promising for **SPE**, particularly Al_N^{+1} and Al_N^0 , which may also be utilized as spin qubit states for **QT**, especially due to the **KS** eigenvalue distribution of the localized state. Even though the **ZPL** energy associated with Al_N^0 is found to be low at 0.180 [eV], we expect a larger value because it is well known that the **PBE** approximation tends to underestimate it.

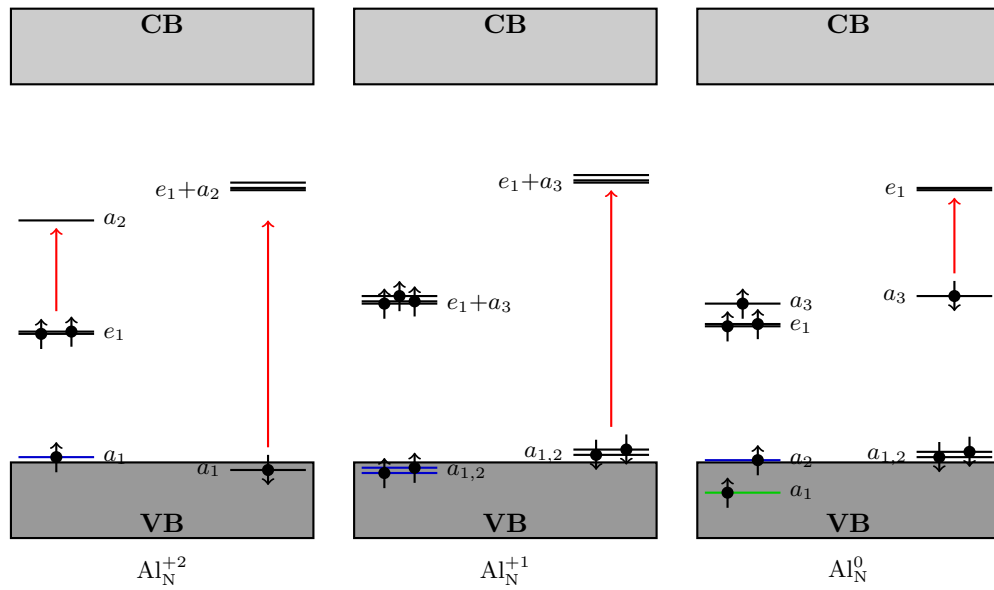


Figure 6.15: KS eigenvalues of the localized (black), apparently localized (green), and delocalized (blue) states for Al_N in the charge states $q = +2, +1, 0$, with the specified orbitals a and e denoting singly orbital state and doubly degenerate orbital state, respectively.

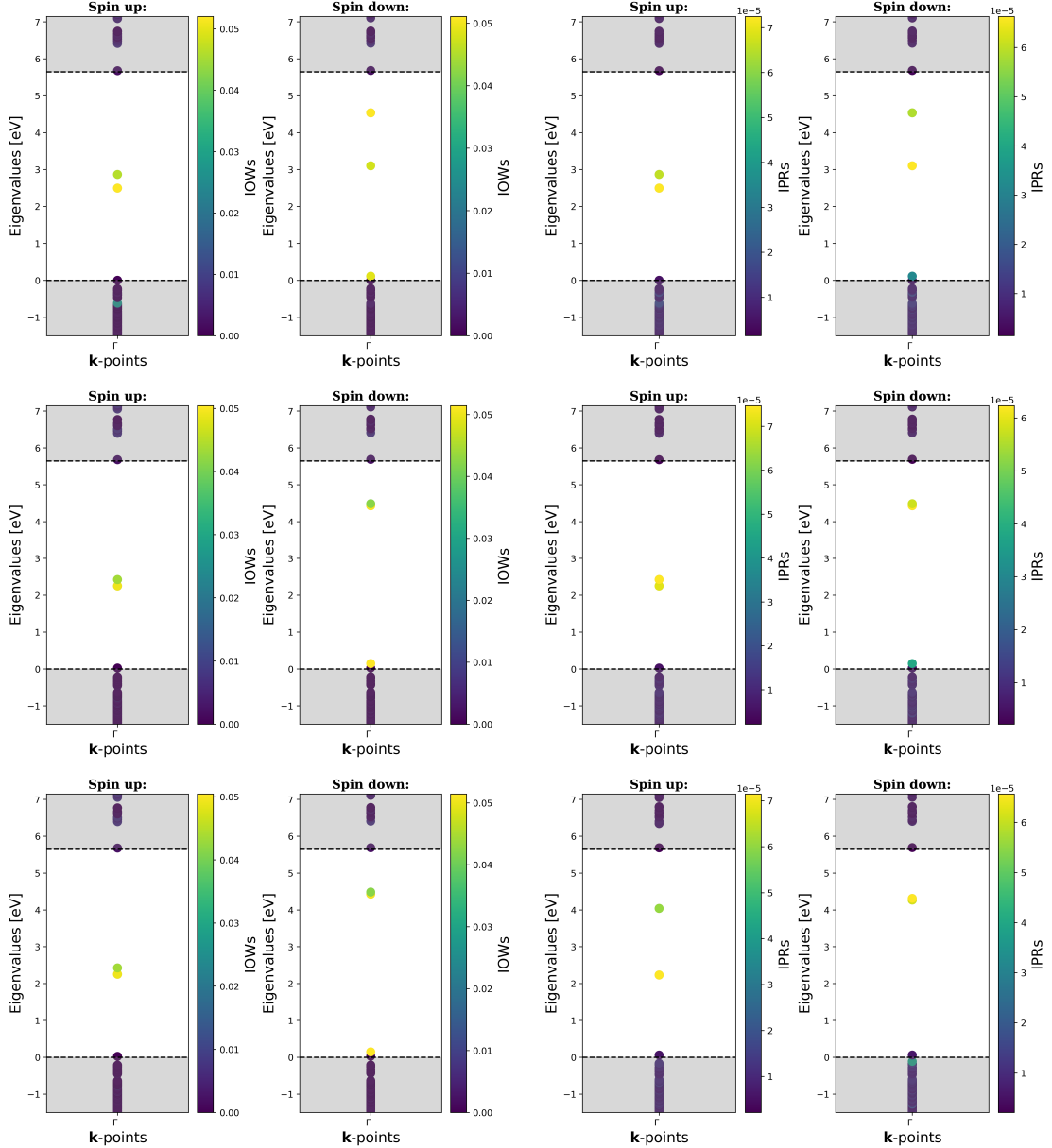


Figure 6.16: KS eigenvalue distribution and corresponding orbital localization factors analyzed using the **IPRs** and **IOWs** methods for V_N^{+2} (top), V_N^{+1} (middle), and V_N^0 (bottom), calculated using **HSE06** at the Γ point. Orbital localization factors are indicated in yellow/green for localized states and purple for delocalized states.

Table 6.11: Ground (E_g) and excited (E_e) states calculated using **PBE** and **HSE06** for Al_N in the selected charge state $q = +2$, $q = +1$ and $q = 0$, along with the corresponding **ZPL** line for the selected spin channel, given in units of energy and wavelength.

Charge	Channel	XC	E_g [eV]	E_e [eV]	E_{ZPL} [eV]	E_{ZPL} [nm]
	\uparrow	PBE	-3217.375	-3216.967	0.408	3038.828
$q = +2$						

		PBE	-3217.375	-3214.682	2.693	460.394
		HSE06	-2621.162	-2617.838	3.324	372.996
$q = +1$	\downarrow	PBE	-3209.148	-3206.192	2.956	419.432
		HSE06	-2612.698	-2609.197	3.501	354.139
$q = 0$	\downarrow	PBE	-3200.388	-3200.208	0.180	6888.010

Selected charge states of Impurity/complex defects

The second portion, we will discuss the selected chage for imputity/complex defects, C_N , V_{NVAl} and C_{NCAl} in the select charge defect states $q = 0$, $q = -1$ and $q = +1$, repectively.

The **KS** eigenvalue distribution and its localized factors are presented in **Figure. 6.18**. In **Figure. 6.17**, the electronic spin distribution for the highest occupied orbitals is schematically illustrated, showing the localization of each orbital and the diffferent excitation electronic transiiton identified. Unluckily, we are only capabed to estimate the **ZPL** energy for C_N^0 by promoting an electron from the doubly degenerate e_1 to the single orbital a_1 state, obtaining a value of $E_{ZPL} = 0.207$ [eV], which is also presented in units of wavelength alongside the ground and excited states in **Table. 6.12**. On the other hand, in the literature [14–16], V_{NVAl} defects have been identified as potential candidate responsible for **SPE**, exhibiting a peak energy around 1.43 [eV]. In contrast, our findings suggest that the electronic transition for $(V_{NVAl})^{-1}$ occurs from the single orbital a_1 to a_4 at a lower energy value. This difference raises the possibility that the charge state $(V_{NVAl})^{-1}$ may not be responsible for the observed peak in **SPE**. However, further investigations are necessary to explore alternative mechanisms or methods beyond **DFT** that account for excited electron properties and offer more accurate descriptions of single-electron orbital states. Finally, $(C_{NCAl})^{+1}$ is still particularly interesting because the formation energy for this specific charge state intersects with that of C_N (**Figure. 6.9b**), suggesting that this charge state may be more likely to form in an atmosphere with carbon impurities atoms, which is corroborated in **Ref. [138]** by further studies using **XC** hybrid functional. Additionally, the **KS** distribution of the localized state could be linked to a potential **SPE**.

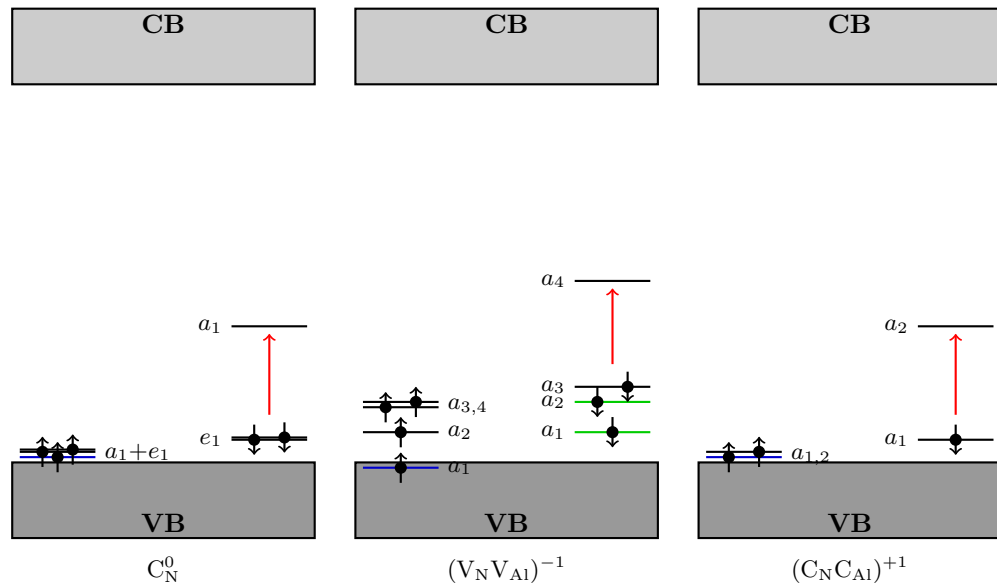


Figure 6.17: KS eigenvalues of the localized (black), apparently localized (green), and delocalized (blue) for the charge state $q = 0$ for V_N , $q = -1$ for $V_N V_{Al}$ and $q = +1$ for $C_N C_{Al}$, with the specified orbitals a and e denoting singly orbital state and doubly degenerate orbital state, respectively.

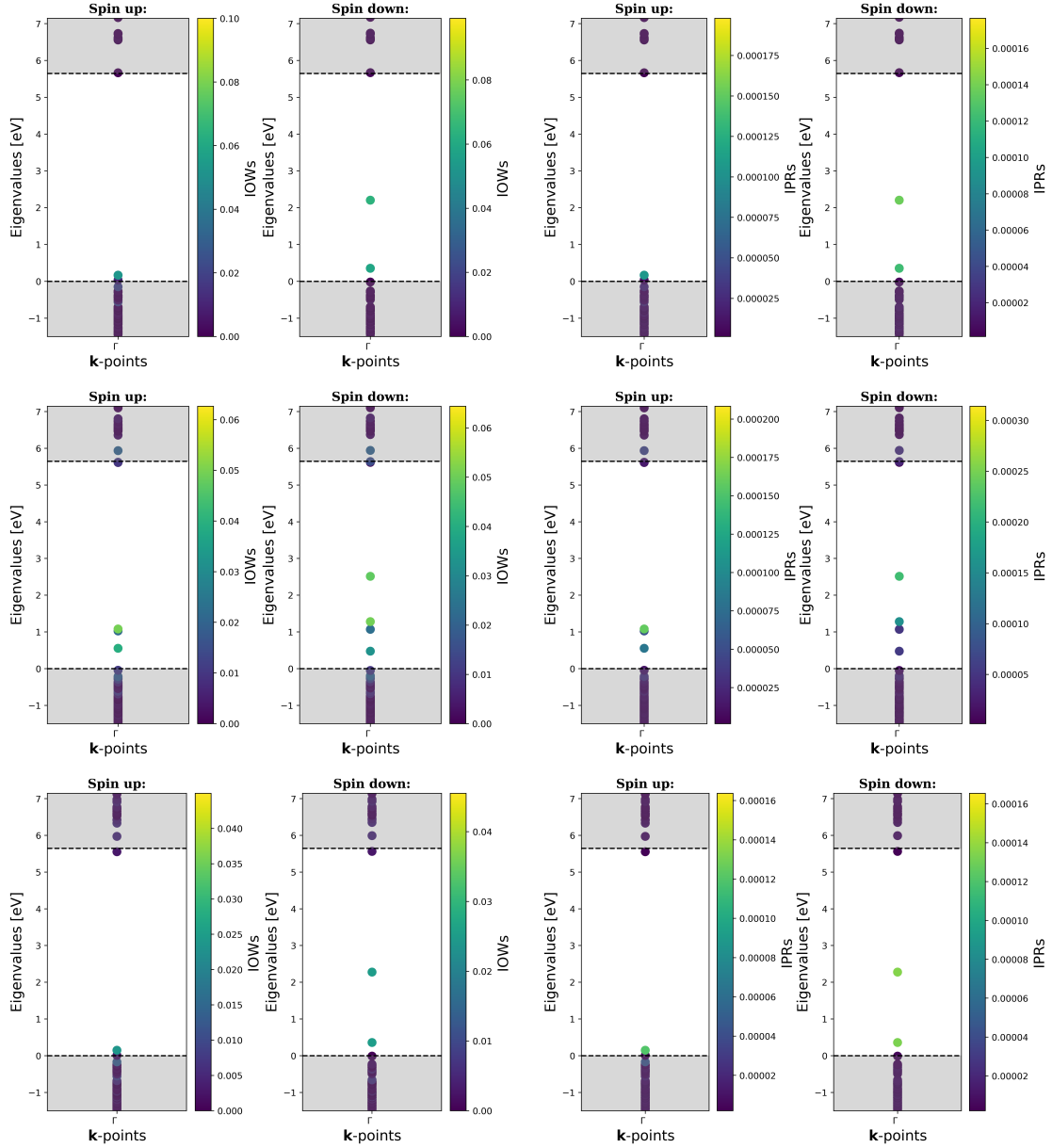


Figure 6.18: KS eigenvalue distribution and corresponding orbital localization factors analyzed using the IPRs and IOWs methods for C_N^0 (top), $(V_N V_{Ai})^{-1}$ (middle), and $(C_N C_N)^{+1}$ (bottom), calculated using **HSE06** at the Γ point. Orbital localization factors are indicated in yellow/green for localized states and purple for delocalized states.

Table 6.12: Ground (E_g) and excited (E_e) states calculated using **PBE** for C_N in the charge state $q = 0$, along with the corresponding **ZPL** line for the selected spin channel, given in units of energy and wavelength.

Charge	Channel	XC	E_g [eV]	E_e [eV]	E_{ZPL} [eV]	E_{ZPL} [nm]
$q = 0$	\downarrow	PBE	-3212.099	-3211.892	0.207	5989.574

6.3.5 Further study of the promising charge defects using G_0W_0

Chapter 7

Concluding remarks

7.1 Conclusions

7.2 Future work

Appendices

Appendix A

Further results and convergence test

A.1 Convergence tests: force, pressure

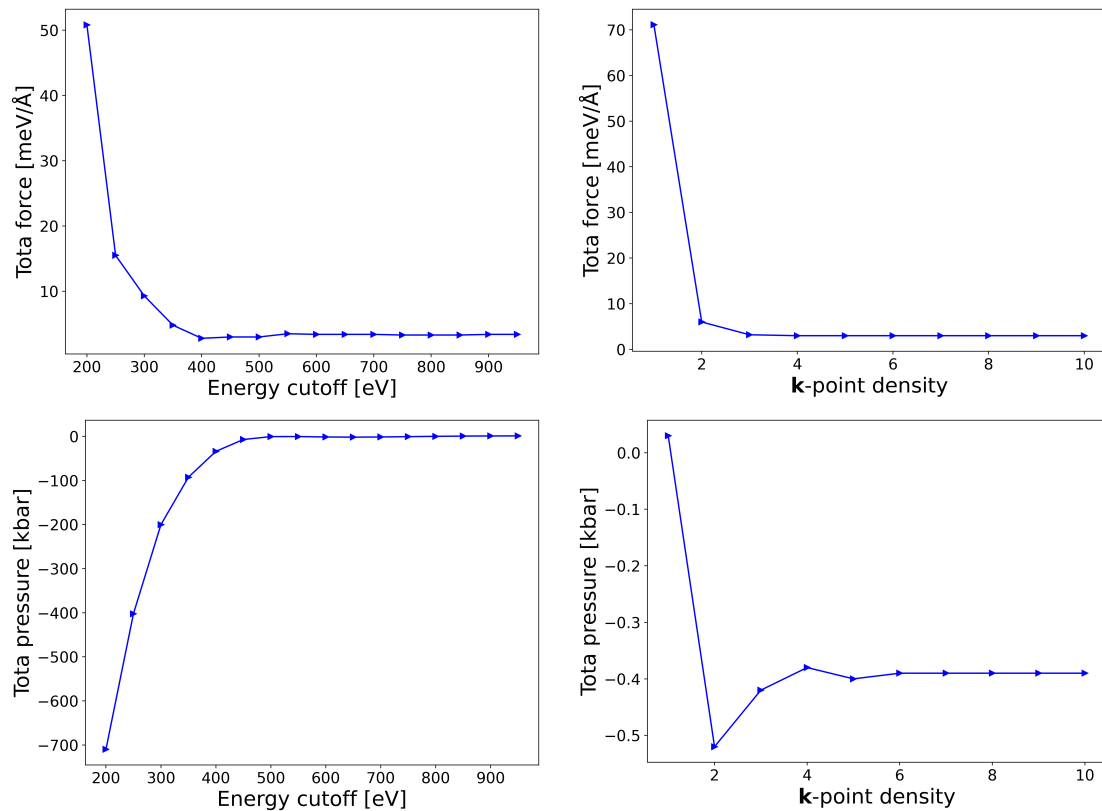
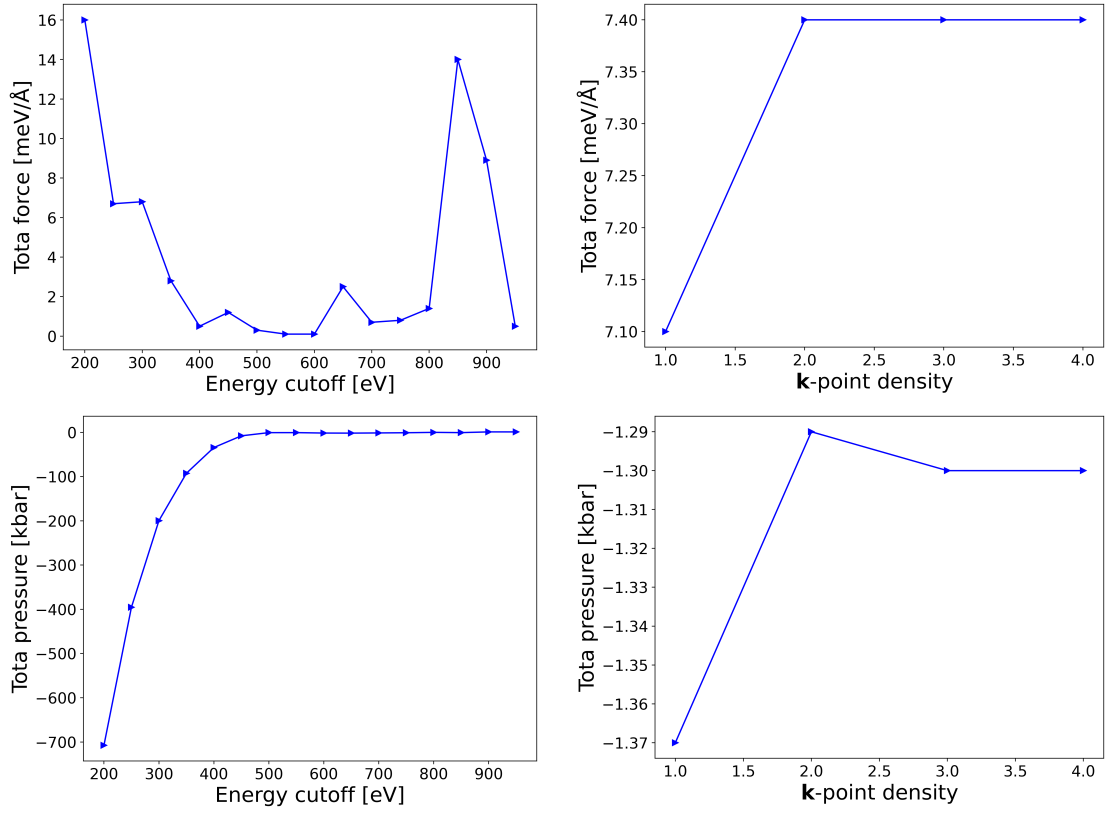


Figure A.1: Unit cell

**Figure A.2:** Supercell

A.2 Convergence table

Table A.1: Calculated values of the energy cutoff test for w-AlN, with energy cutoff range from 200 to 950.

E^{cut} [eV]	E^{tot} [Bulk] [eV]	$E^{tot}[\mathbf{V}_N]$ [eV]	E^{rel} [eV]	$ \Delta E $ [meV]
200	-3260.087	-3239.997	20.090	3038.177
250	-3215.205	-3198.153	17.052	40.449
300	-3212.401	-3195.389	17.012	650.576
350	-3212.776	-3196.415	16.361	77.455
400	-3216.530	-3200.092	16.438	180.967
450	-3217.132	-3200.875	16.257	65.059
500	-3216.464	-3200.271	16.192	1.949
550	-3216.383	-3200.192	16.190	3.408
600	-3216.684	-3200.497	16.187	10.910
650	-3217.039	-3200.841	16.198	18.004

700	-3217.376	-3201.160	16.216	5.661
750	-3217.495	-3201.285	16.210	12.067
800	-3217.624	-3201.402	16.222	46.163
850	-3217.728	-3201.552	16.176	79.854
900	-3217.842	-3201.586	16.256	34.825
950	-3217.809	-3201.588	16.221	—

Table A.2: Calculated values of the K-Points density test for w-AlN, with K-Points density range from 1 to 4.

K-Points density	E^{tot} [Bulk] [eV]	E^{tot} [\mathbf{V}_N][eV]	E^{rel} [eV]	$ \Delta E $ [meV]
1	-3216.009	-3201.733	14.276	12.000
2	-3216.341	-3202.053	14.288	1.000
3	-3216.339	-3202.052	14.287	1.000
4	-3216.340	-3202.053	14.288	—

A.3 KS eigenvalue distribution and their corresponding orbital localization factor

A.3.1 PBE

V_N

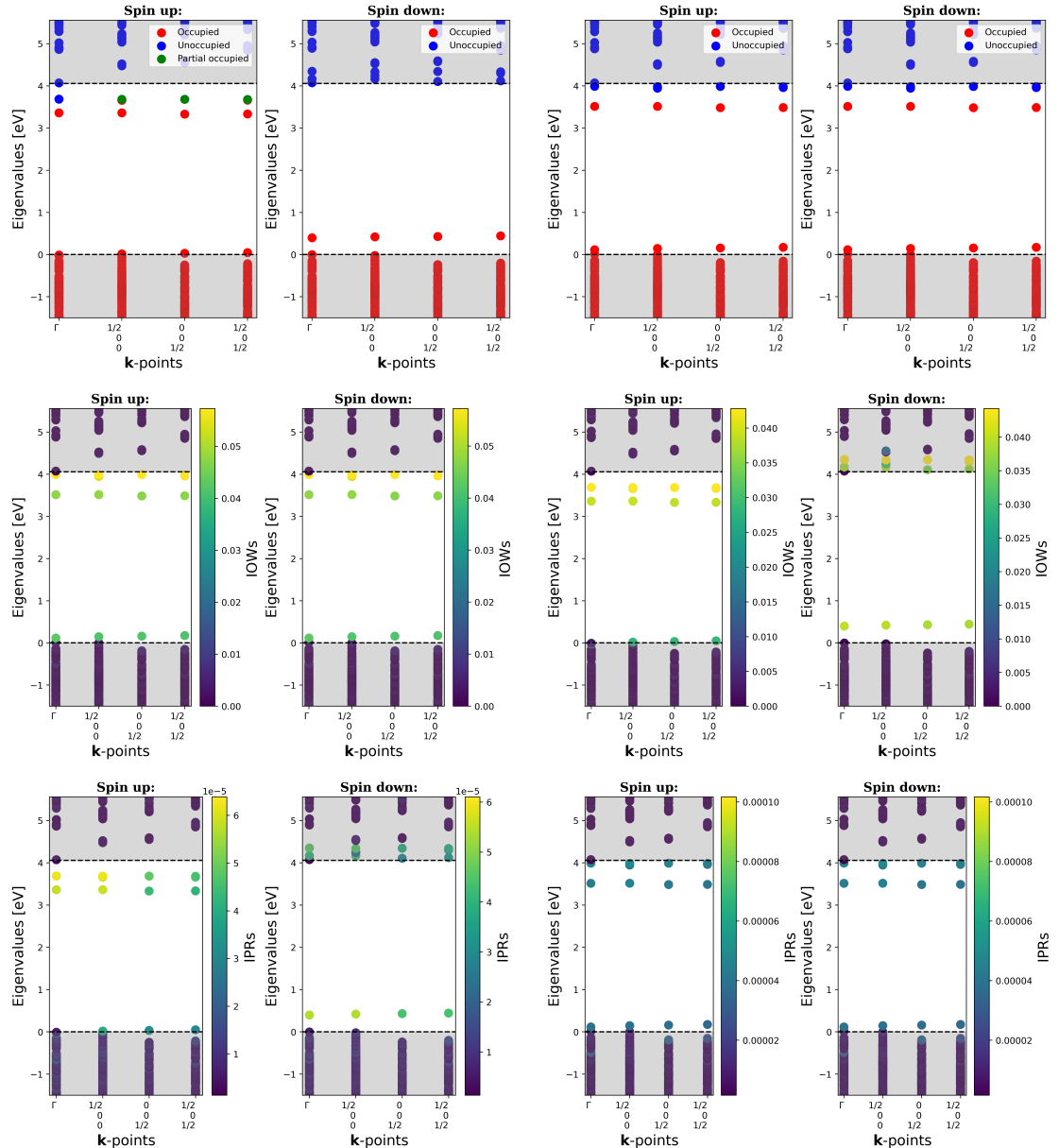


Figure A.3: KS eigenvalue distribution and corresponding orbital localization factors analyzed using the IPRs and IOWs methods for V_N^{-1} in the two different metastable spin electronic configurations: $s = 1$ (top) and $s = 0$ (bottom). Both are calculated using PBE with k-points density 2.0 ($2 \times 2 \times 2$). Orbital localization factors are indicated in yellow/green for localized states and purple for delocalized states.

A.3.2 HSE06

$V_{AI}V_N$

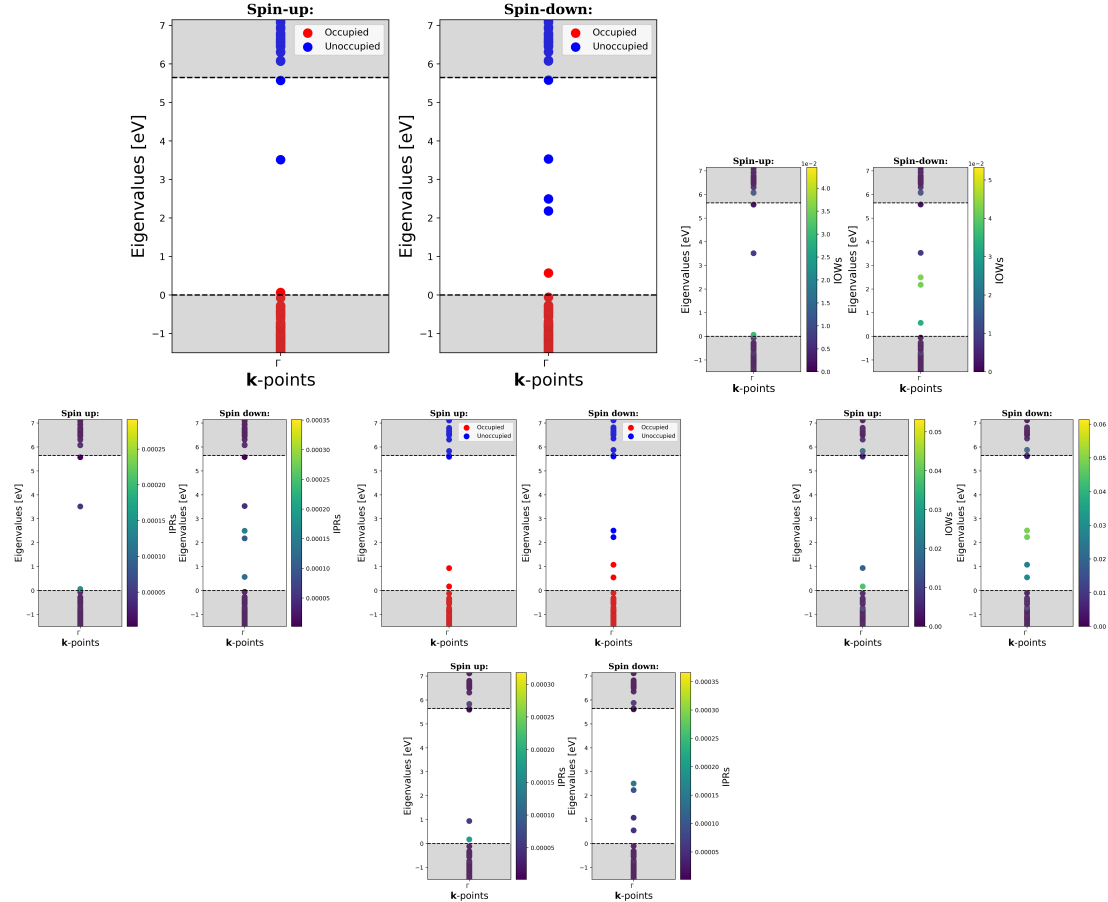


Figure A.4: KS eigenvalue distribution and their corresponding orbital localization factors analyzed using the **IPRs** and **IOWs** methods for V_N^{+2} (top) and $(V_N V_{AL})^0$ (bottom) in the stable spin electronic configurations $s = 1$. Both are calculated using **HSE06** at the Γ point. Orbital localization factors are indicated in yellow/green for localized states and purple for delocalized states.

Bibliography

- [1] A. G. J. MacFarlane, Jonathan P. Dowling and Gerard J. Milburn. ‘Quantum technology: the second quantum revolution’. In: *Philosophical Transactions of the Royal Society of London. Series A: Mathematical, Physical and Engineering Sciences* 361.1809 (2003), pp. 1655–1674. DOI: 10.1098/rsta.2003.1227. eprint: <https://royalsocietypublishing.org/doi/pdf/10.1098/rsta.2003.1227>. URL: <https://royalsocietypublishing.org/doi/abs/10.1098/rsta.2003.1227>.
- [2] Andrew Steane. ‘Quantum computing’. In: *Reports on Progress in Physics* 61.2 (Feb. 1998), p. 117. DOI: 10.1088/0034-4885/61/2/002. URL: <https://dx.doi.org/10.1088/0034-4885/61/2/002>.
- [3] C. L. Degen, F. Reinhard and P. Cappellaro. ‘Quantum sensing’. In: *Rev. Mod. Phys.* 89 (3 June 2017), p. 035002. DOI: 10.1103/RevModPhys.89.035002. URL: <https://link.aps.org/doi/10.1103/RevModPhys.89.035002>.
- [4] Nicolas Gisin and Rob Thew. ‘Quantum communication’. In: *Nature Photonics* 1.3 (2007), pp. 165–171. ISSN: 1749-4893. DOI: 10.1038/nphoton.2007.22. URL: <https://doi.org/10.1038/nphoton.2007.22>.
- [5] T. D. Ladd et al. ‘Quantum computers’. In: *Nature* 464.7285 (2010), pp. 45–53. ISSN: 1476-4687. DOI: 10.1038/nature08812. URL: <https://doi.org/10.1038/nature08812>.
- [6] Sergio O. Valenzuela et al. ‘Microwave-Induced Cooling of a Superconducting Qubit’. In: *Science* 314.5805 (2006), pp. 1589–1592. DOI: 10.1126/science.1134008. eprint: <https://www.science.org/doi/pdf/10.1126/science.1134008>. URL: <https://www.science.org/doi/abs/10.1126/science.1134008>.
- [7] Alec Jenkins et al. ‘Ytterbium Nuclear-Spin Qubits in an Optical Tweezer Array’. In: *Phys. Rev. X* 12 (2 May 2022), p. 021027. DOI: 10.1103/PhysRevX.12.021027. URL: <https://link.aps.org/doi/10.1103/PhysRevX.12.021027>.
- [8] S. A. Lyon. ‘Spin-based quantum computing using electrons on liquid helium’. In: *Phys. Rev. A* 74 (5 Nov. 2006), p. 052338. DOI: 10.1103/PhysRevA.74.052338. URL: <https://link.aps.org/doi/10.1103/PhysRevA.74.052338>.
- [9] Cyrus E. Dreyer et al. ‘First-Principles Calculations of Point Defects for Quantum Technologies’. In: *Annual Review of Materials Research* 48. Volume 48, 2018 (2018), pp. 1–26. ISSN: 1545-4118. DOI: <https://doi.org/10.1146/annurev-matsci-070317-124453>. URL: <https://www.annualreviews.org/content/journals/10.1146/annurev-matsci-070317-124453>.
- [10] Guido Burkard et al. ‘Semiconductor spin qubits’. In: *Rev. Mod. Phys.* 95 (2 June 2023), p. 025003. DOI: 10.1103/RevModPhys.95.025003. URL: <https://link.aps.org/doi/10.1103/RevModPhys.95.025003>.

- [11] Viktor Ivády, Igor A. Abrikosov and Adam Gali. ‘First principles calculation of spin-related quantities for point defect qubit research’. In: *npj Computational Materials* 4.1 (2018), p. 76. ISSN: 2057-3960. DOI: 10.1038/s41524-018-0132-5. URL: <https://doi.org/10.1038/s41524-018-0132-5>.
- [12] Marianne Etzelmüller Bathen and Lasse Vines. ‘Manipulating Single-Photon Emission from Point Defects in Diamond and Silicon Carbide’. In: *Advanced Quantum Technologies* 4.7 (2021), p. 2100003. DOI: <https://doi.org/10.1002/qute.202100003>. eprint: <https://advanced.onlinelibrary.wiley.com/doi/pdf/10.1002/qute.202100003>. URL: <https://advanced.onlinelibrary.wiley.com/doi/abs/10.1002/qute.202100003>.
- [13] Oliver Lerstøl Hebnes et al. ‘Predicting solid state material platforms for quantum technologies’. In: *npj Computational Materials* 8.1 (2022), p. 207. ISSN: 2057-3960. DOI: 10.1038/s41524-022-00888-3. URL: <https://doi.org/10.1038/s41524-022-00888-3>.
- [14] Yongzhou Xue et al. ‘Experimental Optical Properties of Single-Photon Emitters in Aluminum Nitride Films’. In: *The Journal of Physical Chemistry C* 125.20 (2021), pp. 11043–11047. DOI: 10.1021/acs.jpcc.1c01376. eprint: <https://doi.org/10.1021/acs.jpcc.1c01376>. URL: <https://doi.org/10.1021/acs.jpcc.1c01376>.
- [15] Yongzhou Xue et al. ‘Single-Photon Emission from Point Defects in Aluminum Nitride Films’. In: *The Journal of Physical Chemistry Letters* 11.7 (2020). PMID: 32186889, pp. 2689–2694. DOI: 10.1021/acs.jpclett.0c00511. eprint: <https://doi.org/10.1021/acs.jpclett.0c00511>. URL: <https://doi.org/10.1021/acs.jpclett.0c00511>.
- [16] Sam G. Bishop et al. ‘Room-Temperature Quantum Emitter in Aluminum Nitride’. In: *ACS Photonics* 7.7 (2020). PMID: 32905301, pp. 1636–1641. DOI: 10.1021/acsphotonics.0c00528. eprint: <https://doi.org/10.1021/acsphotonics.0c00528>. URL: <https://doi.org/10.1021/acsphotonics.0c00528>.
- [17] Tsung-Ju Lu et al. ‘Bright High-Purity Quantum Emitters in Aluminum Nitride Integrated Photonics’. In: *ACS Photonics* 7.10 (2020), pp. 2650–2657. DOI: 10.1021/acsphotonics.0c01259. eprint: <https://doi.org/10.1021/acsphotonics.0c01259>. URL: <https://doi.org/10.1021/acsphotonics.0c01259>.
- [18] Lee C. Bassett et al. In: *Nanophotonics* 8.11 (2019), pp. 1867–1888. DOI: doi: 10.1515/nanoph-2019-0211. URL: <https://doi.org/10.1515/nanoph-2019-0211>.
- [19] Nanxi Li et al. In: *Nanophotonics* 10.9 (2021), pp. 2347–2387. DOI: doi:10.1515/nanoph-2021-0130. URL: <https://doi.org/10.1515/nanoph-2021-0130>.
- [20] Angus Rockett. *The Materials Science of Semiconductors*. 1st ed. Springer New York, NY, 2008, pp. XVIII, 622. ISBN: 978-0-387-25653-5. DOI: 10.1007/978-0-387-68650-9. URL: <https://doi.org/10.1007/978-0-387-68650-9>.
- [21] Walter Borchardt-Ott. *Crystallography: An Introduction*. 3rd ed. Published: 31 August 2011 (eBook), 28 September 2011 (Softcover). Springer Berlin, Heidelberg, 2012, pp. XVI, 355. ISBN: 978-3-642-16451-4. DOI: 10.1007/978-3-642-16452-1.
- [22] Giuseppe Iadonisi, Giovanni Cantele and Maria Luisa Chiofalo. *Introduction to Solid State Physics and Crystalline Nanostructures*. 1st. UNITEXT for Physics. Milan: Springer Milano, 2014, pp. XXIV, 685. ISBN: 978-88-470-2804-3. DOI: 10.1007/978-88-470-2805-0.

- [23] Charles Kittel. *Introduction to Solid State Physics*. 8th ed. Wiley, 2004. ISBN: 9780471415268. URL: http://www.amazon.com/Introduction-Solid-Physics-Charles-Kittel/dp/047141526X/ref=dp_ob_title_bk.
- [24] Philip Hofmann. *Solid State Physics: An Introduction*. 3rd ed. John Wiley & Sons, 2022. ISBN: 978-3-527-41410-9. URL: <https://www.wiley.com/en-au/Solid+State+Physics%3A+An+Introduction%2C+3rd+Edition-p-9783527414109>.
- [25] Peter W. Atkins and Ronald S. Friedman. *Molecular Quantum Mechanics*. 5th. Oxford: Oxford University Press, 2010.
- [26] Ben Streetman and Sanjay Banerjee. *Solid State Electronic Devices, Global Edition*. Pearson Deutschland, 2015, p. 632. ISBN: 9781292060552. URL: <https://elibrary.pearson.de/book/99.150005/9781292060767>.
- [27] David J. Griffiths and Darrell F. Schroeter. *Introduction to Quantum Mechanics*. 3rd ed. Cambridge University Press, 2018.
- [28] N.W. Ashcroft and N.D. Mermin. *Solid State Physics*. Fort Worth: Saunders College Publishing, 1976.
- [29] Daniel V. Schroeder. *An Introduction to Thermal Physics*. x, 422 p. : illustrations. London: Addison Wesley Longman, 2000. URL: <https://worldcat.org/title/488246685>.
- [30] Robert H. Swendsen. *An Introduction to Statistical Mechanics and Thermodynamics*. Oxford: Oxford University Press, 2012. URL: <https://global.oup.com/academic/product/an-introduction-to-statistical-mechanics-and-thermodynamics-9780199646944>.
- [31] Stephen A. Campbell. *Fabrication Engineering at the Micro- and Nanoscale*. Oxford, UK: Oxford University Press, 2012.
- [32] Aloke Paul et al. *Thermodynamics, Diffusion and the Kirkendall Effect in Solids*. 1st ed. 188 b/w illustrations, 126 illustrations in colour. Cham: Springer International Publishing, 2014, pp. XVIII, 530. ISBN: 978-3-319-07460-3. DOI: 10.1007/978-3-319-07461-0. URL: <https://doi.org/10.1007/978-3-319-07461-0>.
- [33] David A. Porter and Kenneth E. Easterling. *Phase Transformations in Metals and Alloys (Revised Reprint)*. 3rd. Boca Raton: CRC Press, 2009, p. 536. ISBN: 9780429112256. DOI: 10.1201/9781439883570. URL: <https://doi.org/10.1201/9781439883570>.
- [34] Richard J. D. Tilley. *Defects in Solids*. John Wiley & Sons, Inc., 2008. ISBN: 9780470077948. DOI: 10.1002/9780470380758. URL: <https://doi.org/10.1002/9780470380758>.
- [35] M. H. Devoret, A. Wallraff and J. M. Martinis. *Superconducting Qubits: A Short Review*. 2004. arXiv: cond-mat/0411174 [cond-mat.mes-hall]. URL: <https://arxiv.org/abs/cond-mat/0411174>.
- [36] J. R. Weber et al. ‘Quantum computing with defects’. In: *Proceedings of the National Academy of Sciences* 107.19 (2010), pp. 8513–8518. DOI: 10.1073/pnas.1003052107. eprint: <https://www.pnas.org/doi/pdf/10.1073/pnas.1003052107>. URL: <https://www.pnas.org/doi/abs/10.1073/pnas.1003052107>.
- [37] Ettore Bernardi et al. ‘Nanoscale Sensing Using Point Defects in Single-Crystal Diamond: Recent Progress on Nitrogen Vacancy Center-Based Sensors’. In: *Crystals* 7.5 (2017). ISSN: 2073-4352. DOI: 10.3390/crust7050124. URL: <https://www.mdpi.com/2073-4352/7/5/124>.

- [38] Y. Baik and Robin A.L. Drew. ‘Aluminum Nitride: Processing and Applications’. In: *Advanced Ceramic Materials*. Vol. 122. Key Engineering Materials. Trans Tech Publications Ltd, Sept. 1996, pp. 553–. DOI: 10.4028/www.scientific.net/KEM.122-124.553.
- [39] Syed T. Haider et al. ‘A Review of the Recent Applications of Aluminum Nitride-Based Piezoelectric Devices’. In: *IEEE Access* 11 (2023), pp. 58779–58795. DOI: 10.1109/ACCESS.2023.3276716.
- [40] Heinz Schulz and K.H. Thiemann. ‘Crystal structure refinement of AlN and GaN’. In: *Solid State Communications* 23.11 (1977), pp. 815–819. ISSN: 0038-1098. DOI: https://doi.org/10.1016/0038-1098(77)90959-0. URL: https://www.sciencedirect.com/science/article/pii/0038109877909590.
- [41] M A Moram and M E Vickers. ‘X-ray diffraction of III-nitrides’. In: *Reports on Progress in Physics* 72.3 (Feb. 2009), p. 036502. DOI: 10.1088/0034-4885/72/3/036502. URL: https://dx.doi.org/10.1088/0034-4885/72/3/036502.
- [42] P. B. Perry and R. F. Rutz. ‘The optical absorption edge of single-crystal AlN prepared by a close-spaced vapor process’. In: *Applied Physics Letters* 33.4 (Aug. 1978), pp. 319–321. ISSN: 0003-6951. DOI: 10.1063/1.90354. eprint: https://pubs.aip.org/aip/apl/article-pdf/33/4/319/18437468/319_1_online.pdf. URL: https://doi.org/10.1063/1.90354.
- [43] Herbert Goldstein, Charles P. Poole and John L. Safko. *Classical Mechanics*. 3rd. Addison-Wesley, 2002.
- [44] Louis Albert de Broglie. ‘Recherches sur la théorie des quanta’. In: URL: https://api.semanticscholar.org/CorpusID:118951873.
- [45] Tomáš Mančal. *Translation of Werner Heisenberg’s Paper "Quantum-Theoretical Reinterpretation of Kinematic and Mechanical Relations"* Zeitschrift für Physik 33, 1925, 879-893 into Czech language. 2021. arXiv: 2108 . 03119 [physics.ed-ph]. URL: https://arxiv.org/abs/2108.03119.
- [46] Kurt Gottfried and Tung-Mow Yan. *Quantum Mechanics: Fundamentals*. 2nd. Graduate Texts in Contemporary Physics. 1st ed. was originally published by Benjamin, 1996, ISBN 0-8053-3332-0, now with Westview Press, ISBN 0-201-40633-0. Springer New York, NY, 2003, pp. XVIII, 622. ISBN: 978-0-387-95576-6. DOI: 10.1007/978-0-387-21623-2. URL: https://doi.org/10.1007/978-0-387-21623-2.
- [47] J. J. Sakurai and Jim Napolitano. *Modern Quantum Mechanics*. 3rd ed. Cambridge University Press, 2020.
- [48] E. Schrödinger. ‘Quantisierung als Eigenwertproblem’. In: *Annalen der Physik* 385.13 (1926), pp. 437–490. DOI: https://doi.org/10.1002/andp.19263851302. eprint: https://onlinelibrary.wiley.com/doi/pdf/10.1002/andp.19263851302. URL: https://onlinelibrary.wiley.com/doi/abs/10.1002/andp.19263851302.
- [49] E. Schrödinger. ‘An Undulatory Theory of the Mechanics of Atoms and Molecules’. In: *Phys. Rev.* 28 (6 Dec. 1926), pp. 1049–1070. DOI: 10.1103/PhysRev.28.1049. URL: https://link.aps.org/doi/10.1103/PhysRev.28.1049.
- [50] Oskar Klein. ‘Quantum Theory and Five-Dimensional Theory of Relativity. (In German and English)’. In: *Z. Phys.* 37 (1926). Ed. by J. C. Taylor, pp. 895–906. DOI: 10.1007/BF01397481.

- [51] Paul Adrien Maurice Dirac and Ralph Howard Fowler. ‘The quantum theory of the electron’. In: *Proceedings of the Royal Society of London. Series A, Containing Papers of a Mathematical and Physical Character* 117.778 (1928), pp. 610–624. DOI: 10.1098/rspa.1928.0023. eprint: <https://royalsocietypublishing.org/doi/pdf/10.1098/rspa.1928.0023>. URL: <https://royalsocietypublishing.org/doi/abs/10.1098/rspa.1928.0023>.
- [52] Richard P. Feynman, Albert R. Hibbs and Daniel F. Styer. *Quantum Mechanics and Path Integrals, Emended Edition*. First edition published by McGraw-Hill, New York, 1965. Mineola, New York: Dover Publications, 2010, pp. 371 + xii. ISBN: 978-0-486-47722-0.
- [53] Takao Tsuneda. *Density Functional Theory in Quantum Chemistry*. 1st ed. X, 200. Springer Tokyo, 2014. ISBN: 978-4-431-54824-9. DOI: 10.1007/978-4-431-54825-6. URL: <https://doi.org/10.1007/978-4-431-54825-6>.
- [54] Jos Thijssen. *Computational Physics*. 2nd ed. Cambridge University Press, 2007.
- [55] Hiroyuki Nakashima and Hiroshi Nakatsuji. ‘Solving the Schrödinger equation for helium atom and its isoelectronic ions with the free iterative complement interaction (ICI) method’. In: *The Journal of Chemical Physics* 127.22 (Dec. 2007), p. 224104. ISSN: 0021-9606. DOI: 10.1063/1.2801981. eprint: https://pubs.aip.org/aip/jcp/article-pdf/doi/10.1063/1.2801981/13500190/224104_1_online.pdf. URL: <https://doi.org/10.1063/1.2801981>.
- [56] Gareth Hardwick, Senwei Liang and Haizhao Yang. *Solving High-Dimensional Partial Integral Differential Equations: The Finite Expression Method*. 2024. arXiv: 2410.00835 [math.NA]. URL: <https://arxiv.org/abs/2410.00835>.
- [57] M. Born and R. Oppenheimer. ‘Zur Quantentheorie der Moleküle’. In: *Annalen der Physik* 389.20 (1927), pp. 457–484. DOI: <https://doi.org/10.1002/andp.19273892002>. eprint: <https://onlinelibrary.wiley.com/doi/pdf/10.1002/andp.19273892002>. URL: <https://onlinelibrary.wiley.com/doi/abs/10.1002/andp.19273892002>.
- [58] Attila Szabo and Neil S. Ostlund. *Modern Quantum Chemistry: Introduction to Advanced Electronic Structure Theory*. New York: Dover Publications, 1989.
- [59] Richard M. Martin. *Electronic Structure: Basic Theory and Practical Methods*. Cambridge University Press, 2004.
- [60] David S. Sholl and Janice A. Steckel. *Density Functional Theory: A Practical Introduction*. 2nd. Wiley, 2023. ISBN: 978-1-119-84086-2.
- [61] Robert G Parr and Yang Weitao. *Density-Functional Theory of Atoms and Molecules*. Oxford University Press, Jan. 1995. ISBN: 9780195092769. DOI: 10.1093/oso/9780195092769.001.0001. URL: <https://doi.org/10.1093/oso/9780195092769.001.0001>.
- [62] J. C. Slater. ‘The Self Consistent Field and the Structure of Atoms’. In: *Phys. Rev.* 32 (3 Sept. 1928), pp. 339–348. DOI: 10.1103/PhysRev.32.339. URL: <https://link.aps.org/doi/10.1103/PhysRev.32.339>.
- [63] Prashant Singh and Manoj K Harbola. ‘Density-functional theory of material design: fundamentals and applications-I’. In: *Oxford Open Materials Science* 1.1 (Dec. 2021), itab018. ISSN: 2633-6979. DOI: 10.1093/oxfmat/itab018. eprint: <https://academic.oup.com/ooms/article-pdf/1/1/itab018/45723625/itab018.pdf>. URL: <https://doi.org/10.1093/oxfmat/itab018>.

- [64] Douglas R. Hartree. *The Calculation of Atomic Structures*. John Wiley and Sons, Inc, 1957.
- [65] I. M. Gelfand and S. V. Fomin. *Calculus of Variations*. Dover Books on Mathematics. Dover Publications, 2000. ISBN: 978-0486414485.
- [66] Enrico Clementi and Carla Roetti. ‘Roothaan-Hartree-Fock atomic wavefunctions: Basis functions and their coefficients for ground and certain excited states of neutral and ionized atoms, $Z \leq 54$ ’. In: *Atomic Data and Nuclear Data Tables* 14.3 (1974), pp. 177–478. ISSN: 0092-640X. DOI: [https://doi.org/10.1016/S0092-640X\(74\)80016-1](https://doi.org/10.1016/S0092-640X(74)80016-1). URL: <https://www.sciencedirect.com/science/article/pii/S0092640X74800161>.
- [67] Charlotte Froese Fischer. ‘General Hartree-Fock program’. In: *Computer Physics Communications* 43.3 (1987), pp. 355–365. ISSN: 0010-4655. DOI: [https://doi.org/10.1016/0010-4655\(87\)90053-1](https://doi.org/10.1016/0010-4655(87)90053-1). URL: <https://www.sciencedirect.com/science/article/pii/0010465587900531>.
- [68] D. R. Hartree. ‘The Wave Mechanics of an Atom with a Non-Coulomb Central Field. Part I. Theory and Methods’. In: *Mathematical Proceedings of the Cambridge Philosophical Society* 24.1 (1928), pp. 89–110. DOI: [10.1017/S0305004100011919](https://doi.org/10.1017/S0305004100011919).
- [69] J. C. Slater. ‘The Electronic Structure of Metals’. In: *Rev. Mod. Phys.* 6 (4 Sept. 1934), pp. 209–280. DOI: [10.1103/RevModPhys.6.209](https://doi.org/10.1103/RevModPhys.6.209). URL: <https://link.aps.org/doi/10.1103/RevModPhys.6.209>.
- [70] J. C. Slater. ‘A Simplification of the Hartree-Fock Method’. In: *Phys. Rev.* 81 (3 Feb. 1951), pp. 385–390. DOI: [10.1103/PhysRev.81.385](https://doi.org/10.1103/PhysRev.81.385). URL: <https://link.aps.org/doi/10.1103/PhysRev.81.385>.
- [71] Pablo Echenique and J. L. Alonso. ‘A mathematical and computational review of Hartree–Fock SCF methods in quantum chemistry’. In: *Molecular Physics* 105.23–24 (Dec. 2007), pp. 3057–3098. ISSN: 1362-3028. DOI: [10.1080/00268970701757875](https://doi.org/10.1080/00268970701757875). URL: <http://dx.doi.org/10.1080/00268970701757875>.
- [72] R. O. Jones. ‘Density functional theory: Its origins, rise to prominence, and future’. In: *Rev. Mod. Phys.* 87 (3 Aug. 2015), pp. 897–923. DOI: [10.1103/RevModPhys.87.897](https://doi.org/10.1103/RevModPhys.87.897). URL: <https://link.aps.org/doi/10.1103/RevModPhys.87.897>.
- [73] P. Hohenberg and W. Kohn. ‘Inhomogeneous Electron Gas’. In: *Phys. Rev.* 136 (3B Nov. 1964), B864–B871. DOI: [10.1103/PhysRev.136.B864](https://doi.org/10.1103/PhysRev.136.B864). URL: <https://link.aps.org/doi/10.1103/PhysRev.136.B864>.
- [74] Eberhard Engel and Reiner M. Dreizler. *Density Functional Theory: An Advanced Course*. 1st ed. Theoretical and Mathematical Physics. Springer Berlin, Heidelberg, 2011, pp. XV, 531. ISBN: 978-3-642-14089-1. DOI: [10.1007/978-3-642-14090-7](https://doi.org/10.1007/978-3-642-14090-7).
- [75] Eric Cancès and Gero Friesecke, eds. *Density Functional Theory: Modeling, Mathematical Analysis, Computational Methods, and Applications*. 1st ed. Mathematics and Molecular Modeling. Springer Cham, 2023, pp. XIX, 580. ISBN: 978-3-031-22339-6. DOI: [10.1007/978-3-031-22340-2](https://doi.org/10.1007/978-3-031-22340-2).
- [76] Carlos Fiolhais, Fernando Nogueira and Miguel A. L. Marques, eds. *A Primer in Density Functional Theory*. 1st ed. Lecture Notes in Physics. Springer Berlin, Heidelberg, 2003, pp. XIII, 258. ISBN: 978-3-540-03083-6. DOI: [10.1007/3-540-37072-2](https://doi.org/10.1007/3-540-37072-2).

- [77] Reiner M. Dreizler and Eberhard K. U. Gross. *Density Functional Theory: An Approach to the Quantum Many-Body Problem*. 1st ed. Springer Book Archive, Copyright Springer-Verlag Berlin Heidelberg 1990. Published online: 06 December 2012. Springer Berlin, Heidelberg, 1990, pp. XI, 304. ISBN: 978-3-642-86105-5. DOI: <https://doi.org/10.1007/978-3-642-86105-5>.
- [78] W. Kohn and L. J. Sham. ‘Self-Consistent Equations Including Exchange and Correlation Effects’. In: *Phys. Rev.* 140 (4A Nov. 1965), A1133–A1138. DOI: 10.1103/PhysRev.140.A1133. URL: <https://link.aps.org/doi/10.1103/PhysRev.140.A1133>.
- [79] W. Kohn, A. D. Becke and R. G. Parr. ‘Density Functional Theory of Electronic Structure’. In: *The Journal of Physical Chemistry* 100.31 (1996), pp. 12974–12980. DOI: 10.1021/jp960669l. URL: <https://doi.org/10.1021/jp960669l>.
- [80] Jianwei Sun, John P. Perdew and Michael Seidl. ‘Correlation energy of the uniform electron gas from an interpolation between high- and low-density limits’. In: *Phys. Rev. B* 81 (8 Feb. 2010), p. 085123. DOI: 10.1103/PhysRevB.81.085123. URL: <https://link.aps.org/doi/10.1103/PhysRevB.81.085123>.
- [81] John P. Perdew, Kieron Burke and Matthias Ernzerhof. ‘Generalized Gradient Approximation Made Simple’. In: *Phys. Rev. Lett.* 77 (18 Oct. 1996), pp. 3865–3868. DOI: 10.1103/PhysRevLett.77.3865. URL: <https://link.aps.org/doi/10.1103/PhysRevLett.77.3865>.
- [82] Aliaksandr V. Krukau et al. ‘Influence of the exchange screening parameter on the performance of screened hybrid functionals’. In: *The Journal of Chemical Physics* 125.22 (Dec. 2006), p. 224106. ISSN: 0021-9606. DOI: 10.1063/1.2404663. eprint: https://pubs.aip.org/aip/jcp/article-pdf/doi/10.1063/1.2404663/13263224/224106_1_online.pdf. URL: <https://doi.org/10.1063/1.2404663>.
- [83] Edward N. Brothers et al. ‘Accurate solid-state band gaps via screened hybrid electronic structure calculations’. In: *The Journal of Chemical Physics* 129.1 (July 2008), p. 011102. ISSN: 0021-9606. DOI: 10.1063/1.2955460. eprint: https://pubs.aip.org/aip/jcp/article-pdf/doi/10.1063/1.2955460/15416413/011102_1_online.pdf. URL: <https://doi.org/10.1063/1.2955460>.
- [84] Jochen Heyd, Gustavo E. Scuseria and Matthias Ernzerhof. ‘Hybrid functionals based on a screened Coulomb potential’. In: *The Journal of Chemical Physics* 118.18 (May 2003), pp. 8207–8215. ISSN: 0021-9606. DOI: 10.1063/1.1564060. eprint: https://pubs.aip.org/aip/jcp/article-pdf/118/18/8207/19093575/8207_1_online.pdf. URL: <https://doi.org/10.1063/1.1564060>.
- [85] Risto M. Nieminen. ‘Supercell Methods for Defect Calculations’. In: *Theory of Defects in Semiconductors*. Ed. by David A. Drabold and Stefan K. Estreicher. Berlin, Heidelberg: Springer Berlin Heidelberg, 2007, pp. 29–68. ISBN: 978-3-540-33401-9. DOI: 10.1007/11690320_3. URL: https://doi.org/10.1007/11690320_3.
- [86] P. E. Blöchl. ‘Projector augmented-wave method’. In: *Phys. Rev. B* 50 (24 Dec. 1994), pp. 17953–17979. DOI: 10.1103/PhysRevB.50.17953. URL: <https://link.aps.org/doi/10.1103/PhysRevB.50.17953>.
- [87] G. Kresse and D. Joubert. ‘From ultrasoft pseudopotentials to the projector augmented-wave method’. In: *Phys. Rev. B* 59 (3 Jan. 1999), pp. 1758–1775. DOI: 10.1103/PhysRevB.59.1758. URL: <https://link.aps.org/doi/10.1103/PhysRevB.59.1758>.

- [88] David Vanderbilt. ‘Soft self-consistent pseudopotentials in a generalized eigenvalue formalism’. In: *Phys. Rev. B* 41 (11 Apr. 1990), pp. 7892–7895. DOI: 10.1103/PhysRevB.41.7892. URL: <https://link.aps.org/doi/10.1103/PhysRevB.41.7892>.
- [89] Peter E. Blöchl, Clemens J. Först and Johannes Schimpl. ‘Projector augmented wave method: ab initio molecular dynamics with full wave functions’. In: *Bulletin of Materials Science* 26.1 (2003), pp. 33–41. ISSN: 0973-7669. DOI: 10.1007/BF02712785. URL: <https://doi.org/10.1007/BF02712785>.
- [90] D. Hobbs, G. Kresse and J. Hafner. ‘Fully unconstrained noncollinear magnetism within the projector augmented-wave method’. In: *Phys. Rev. B* 62 (17 Nov. 2000), pp. 11556–11570. DOI: 10.1103/PhysRevB.62.11556. URL: <https://link.aps.org/doi/10.1103/PhysRevB.62.11556>.
- [91] Carsten Rostgaard. *The Projector Augmented-wave Method*. 2009. arXiv: 0910.1921 [cond-mat.mtrl-sci]. URL: <https://arxiv.org/abs/0910.1921>.
- [92] Marco Arrigoni and Georg K.H. Madsen. ‘Spinney: Post-processing of first-principles calculations of point defects in semiconductors with Python’. In: *Computer Physics Communications* 264 (2021), p. 107946. ISSN: 0010-4655. DOI: <https://doi.org/10.1016/j.cpc.2021.107946>. URL: <https://www.sciencedirect.com/science/article/pii/S0010465521000709>.
- [93] Chris G. Van de Walle and Anderson Janotti. ‘Advances in electronic structure methods for defects and impurities in solids’. In: *physica status solidi (b)* 248.1 (2011), pp. 19–27. DOI: <https://doi.org/10.1002/pssb.201046290>. eprint: <https://onlinelibrary.wiley.com/doi/pdf/10.1002/pssb.201046290>. URL: <https://onlinelibrary.wiley.com/doi/abs/10.1002/pssb.201046290>.
- [94] Jutta Rogal et al. ‘Perspectives on point defect thermodynamics’. In: *physica status solidi (b)* 251.1 (2014), pp. 97–129. DOI: <https://doi.org/10.1002/pssb.201350155>. eprint: <https://onlinelibrary.wiley.com/doi/pdf/10.1002/pssb.201350155>. URL: <https://onlinelibrary.wiley.com/doi/abs/10.1002/pssb.201350155>.
- [95] Christoph Freysoldt et al. ‘First-principles calculations for point defects in solids’. In: *Rev. Mod. Phys.* 86 (1 Mar. 2014), pp. 253–305. DOI: 10.1103/RevModPhys.86.253. URL: <https://link.aps.org/doi/10.1103/RevModPhys.86.253>.
- [96] Anuj Goyal et al. ‘A computational framework for automation of point defect calculations’. In: *Computational Materials Science* 130 (2017), pp. 1–9. ISSN: 0927-0256. DOI: <https://doi.org/10.1016/j.commatsci.2016.12.040>. URL: <https://www.sciencedirect.com/science/article/pii/S0927025617300010>.
- [97] Chris G. Van de Walle and Jörg Neugebauer. ‘First-principles calculations for defects and impurities: Applications to III-nitrides’. In: *Journal of Applied Physics* 95.8 (Apr. 2004), pp. 3851–3879. ISSN: 0021-8979. DOI: 10.1063/1.1682673. eprint: https://pubs.aip.org/aip/jap/article-pdf/95/8/3851/18708376/3851_1_online.pdf. URL: <https://doi.org/10.1063/1.1682673>.
- [98] Hannu-Pekka Komsa, Tapio T. Rantala and Alfredo Pasquarello. ‘Finite-size supercell correction schemes for charged defect calculations’. In: *Phys. Rev. B* 86 (4 July 2012), p. 045112. DOI: 10.1103/PhysRevB.86.045112. URL: <https://link.aps.org/doi/10.1103/PhysRevB.86.045112>.

- [99] Yu Kumagai and Fumiyasu Oba. ‘Electrostatics-based finite-size corrections for first-principles point defect calculations’. In: *Phys. Rev. B* 89 (19 May 2014), p. 195205. DOI: 10.1103/PhysRevB.89.195205. URL: <https://link.aps.org/doi/10.1103/PhysRevB.89.195205>.
- [100] Stephan Lany and Alex Zunger. ‘Accurate prediction of defect properties in density functional supercell calculations’. In: *Modelling and Simulation in Materials Science and Engineering* 17.8 (Nov. 2009), p. 084002. DOI: 10.1088/0965-0393/17/8/084002. URL: <https://dx.doi.org/10.1088/0965-0393/17/8/084002>.
- [101] Christoph Freysoldt, Jörg Neugebauer and Chris G. Van de Walle. ‘Fully Ab Initio Finite-Size Corrections for Charged-Defect Supercell Calculations’. In: *Phys. Rev. Lett.* 102 (1 June 2009), p. 016402. DOI: 10.1103/PhysRevLett.102.016402. URL: <https://link.aps.org/doi/10.1103/PhysRevLett.102.016402>.
- [102] Christoph Freysoldt, Jörg Neugebauer and Chris G. Van de Walle. ‘Electrostatic interactions between charged defects in supercells’. In: *physica status solidi (b)* 248.5 (2011), pp. 1067–1076. DOI: <https://doi.org/10.1002/pssb.201046289>. eprint: <https://onlinelibrary.wiley.com/doi/pdf/10.1002/pssb.201046289>. URL: <https://onlinelibrary.wiley.com/doi/abs/10.1002/pssb.201046289>.
- [103] G. Makov and M. C. Payne. ‘Periodic boundary conditions in ab initio calculations’. In: *Phys. Rev. B* 51 (7 Feb. 1995), pp. 4014–4022. DOI: 10.1103/PhysRevB.51.4014. URL: <https://link.aps.org/doi/10.1103/PhysRevB.51.4014>.
- [104] Y. Kumagai. ‘PYDEFECT’. In: (2021). URL: <https://github.com/kumagai-group/pydefect>.
- [105] Yu Kumagai et al. ‘Insights into oxygen vacancies from high-throughput first-principles calculations’. In: *Phys. Rev. Mater.* 5 (12 Dec. 2021), p. 123803. DOI: 10.1103/PhysRevMaterials.5.123803. URL: <https://link.aps.org/doi/10.1103/PhysRevMaterials.5.123803>.
- [106] Xiaodong Xu et al. ‘To define nonradiative defects in semiconductors: An accurate DLTS simulation based on first-principle’. In: *Computational Materials Science* 215 (2022), p. 111760. ISSN: 0927-0256. DOI: <https://doi.org/10.1016/j.commatsci.2022.111760>. URL: <https://www.sciencedirect.com/science/article/pii/S0927025622004736>.
- [107] Xavier Gonze et al. ‘Constrained Density Functional Theory: A Potential-Based Self-Consistency Approach’. In: *Journal of Chemical Theory and Computation* 18.10 (2022). PMID: 36099643, pp. 6099–6110. DOI: 10.1021/acs.jctc.2c00673. eprint: <https://doi.org/10.1021/acs.jctc.2c00673>. URL: <https://doi.org/10.1021/acs.jctc.2c00673>.
- [108] Benjamin Kaduk, Tim Kowalczyk and Troy Van Voorhis. ‘Constrained Density Functional Theory’. In: *Chemical Reviews* 112.1 (2012). PMID: 22077560, pp. 321–370. DOI: 10.1021/cr200148b. eprint: <https://doi.org/10.1021/cr200148b>. URL: <https://doi.org/10.1021/cr200148b>.
- [109] Audrius Alkauskas, Matthew D. McCluskey and Chris G. Van de Walle. ‘Tutorial: Defects in semiconductors—Combining experiment and theory’. In: *Journal of Applied Physics* 119.18 (May 2016), p. 181101. ISSN: 0021-8979. DOI: 10.1063/1.4948245. eprint: https://pubs.aip.org/aip/jap/article-pdf/doi/10.1063/1.4948245/19940133/181101_1_1.4948245.pdf. URL: <https://doi.org/10.1063/1.4948245>.

- [110] Luke Gordon et al. ‘Quantum computing with defects’. In: *MRS Bulletin* 38.10 (2013), pp. 802–807. DOI: 10.1557/mrs.2013.206.
- [111] Jimenez A.L.R. ‘VaspDefAnalysis’. In: (2025). URL: <https://github.com/luisrj11/VaspDefAnalysis.git>.
- [112] Audrius Alkauskas et al. ‘First-Principles Calculations of Luminescence Spectrum Line Shapes for Defects in Semiconductors: The Example of GaN and ZnO’. In: *Phys. Rev. Lett.* 109 (26 Dec. 2012), p. 267401. DOI: 10.1103/PhysRevLett.109.267401. URL: <https://link.aps.org/doi/10.1103/PhysRevLett.109.267401>.
- [113] Yongchao Jia et al. ‘First-principles study of the luminescence of Eu²⁺-doped phosphors’. In: *Phys. Rev. B* 96 (12 Sept. 2017), p. 125132. DOI: 10.1103/PhysRevB.96.125132. URL: <https://link.aps.org/doi/10.1103/PhysRevB.96.125132>.
- [114] Yuzo Shinozuka Yuzo Shinozuka. ‘Electron-Lattice Interaction in Nonmetallic Materials: Configuration Coordinate Diagram and Lattice Relaxation’. In: *Japanese Journal of Applied Physics* 32.10R (Oct. 1993), p. 4560. DOI: 10.1143/JJAP.32.4560. URL: <https://dx.doi.org/10.1143/JJAP.32.4560>.
- [115] Yu Jin et al. ‘Photoluminescence spectra of point defects in semiconductors: Validation of first-principles calculations’. In: *Phys. Rev. Mater.* 5 (8 Aug. 2021), p. 084603. DOI: 10.1103/PhysRevMaterials.5.084603. URL: <https://link.aps.org/doi/10.1103/PhysRevMaterials.5.084603>.
- [116] Agata Kaminska et al. ‘Defect-related photoluminescence and photoluminescence excitation as a method to study the excitonic bandgap of AlN epitaxial layers: Experimental and ab initio analysis’. In: *Applied Physics Letters* 117.23 (Dec. 2020), p. 232101. ISSN: 0003-6951. DOI: 10.1063/5.0027743. eprint: https://pubs.aip.org/aip/apl/article-pdf/doi/10.1063/5.0027743/14541299/232101_1_online.pdf. URL: <https://doi.org/10.1063/5.0027743>.
- [117] G. Kresse and J. Furthmüller. ‘Efficiency of ab-initio total energy calculations for metals and semiconductors using a plane-wave basis set’. In: *Computational Materials Science* 6.1 (1996), pp. 15–50. ISSN: 0927-0256. DOI: [https://doi.org/10.1016/0927-0256\(96\)00008-0](https://doi.org/10.1016/0927-0256(96)00008-0). URL: <https://www.sciencedirect.com/science/article/pii/0927025696000080>.
- [118] G. Kresse and J. Hafner. ‘Ab initio molecular-dynamics simulation of the liquid-metal–amorphous-semiconductor transition in germanium’. In: *Phys. Rev. B* 49 (20 May 1994), pp. 14251–14269. DOI: 10.1103/PhysRevB.49.14251. URL: <https://link.aps.org/doi/10.1103/PhysRevB.49.14251>.
- [119] G. Kresse and J. Furthmüller. ‘Efficient iterative schemes for ab initio total-energy calculations using a plane-wave basis set’. In: *Phys. Rev. B* 54 (16 Oct. 1996), pp. 11169–11186. DOI: 10.1103/PhysRevB.54.11169. URL: <https://link.aps.org/doi/10.1103/PhysRevB.54.11169>.
- [120] C. W. M. Castleton, A. Höglund and S. Mirbt. ‘Managing the supercell approximation for charged defects in semiconductors: Finite-size scaling, charge correction factors, the band-gap problem, and the ab initio dielectric constant’. In: *Phys. Rev. B* 73 (3 June 2006), p. 035215. DOI: 10.1103/PhysRevB.73.035215. URL: <https://link.aps.org/doi/10.1103/PhysRevB.73.035215>.

- [121] Ifeanyi H. Nwigboji et al. ‘Ab-initio computations of electronic and transport properties of wurtzite aluminum nitride (w-AlN)’. In: *Materials Chemistry and Physics* 157 (2015), pp. 80–86. ISSN: 0254-0584. DOI: <https://doi.org/10.1016/j.matchemphys.2015.03.019>. URL: <https://www.sciencedirect.com/science/article/pii/S0254058415001716>.
- [122] Martin Feneberg et al. ‘High-excitation and high-resolution photoluminescence spectra of bulk AlN’. In: *Phys. Rev. B* 82 (7 Aug. 2010), p. 075208. DOI: [10.1103/PhysRevB.82.075208](https://doi.org/10.1103/PhysRevB.82.075208). URL: <https://link.aps.org/doi/10.1103/PhysRevB.82.075208>.
- [123] Yanlian Yang et al. ‘Optical and Structural Properties of Aluminum Nitride Epi-Films at Room and High Temperature’. In: *Materials* 16.23 (2023). ISSN: 1996-1944. DOI: [10.3390/ma16237442](https://doi.org/10.3390/ma16237442). URL: <https://www.mdpi.com/1996-1944/16/23/7442>.
- [124] John P. Perdew. ‘Density functional theory and the band gap problem’. In: *International Journal of Quantum Chemistry* 28.S19 (1985), pp. 497–523. DOI: <https://doi.org/10.1002/qua.560280846>. eprint: [https://onlinelibrary.wiley.com/doi/abs/10.1002/qua.560280846](https://onlinelibrary.wiley.com/doi/pdf/10.1002/qua.560280846). URL: <https://onlinelibrary.wiley.com/doi/abs/10.1002/qua.560280846>.
- [125] Jason M. Crowley, Jamil Tahir-Kheli and William A. III Goddard. ‘Resolution of the Band Gap Prediction Problem for Materials Design’. In: *The Journal of Physical Chemistry Letters* 7.7 (2016). PMID: 26944092, pp. 1198–1203. DOI: [10.1021/acs.jpclett.5b02870](https://doi.org/10.1021/acs.jpclett.5b02870). eprint: <https://doi.org/10.1021/acs.jpclett.5b02870>. URL: <https://doi.org/10.1021/acs.jpclett.5b02870>.
- [126] Stephan Lany and Alex Zunger. ‘Assessment of correction methods for the band-gap problem and for finite-size effects in supercell defect calculations: Case studies for ZnO and GaAs’. In: *Phys. Rev. B* 78 (23 Dec. 2008), p. 235104. DOI: [10.1103/PhysRevB.78.235104](https://doi.org/10.1103/PhysRevB.78.235104). URL: <https://link.aps.org/doi/10.1103/PhysRevB.78.235104>.
- [127] J. P. Perdew and Alex Zunger. ‘Self-interaction correction to density-functional approximations for many-electron systems’. In: *Phys. Rev. B* 23 (10 May 1981), pp. 5048–5079. DOI: [10.1103/PhysRevB.23.5048](https://doi.org/10.1103/PhysRevB.23.5048). URL: <https://link.aps.org/doi/10.1103/PhysRevB.23.5048>.
- [128] John P. Perdew and Mel Levy. ‘Physical Content of the Exact Kohn-Sham Orbital Energies: Band Gaps and Derivative Discontinuities’. In: *Phys. Rev. Lett.* 51 (20 Nov. 1983), pp. 1884–1887. DOI: [10.1103/PhysRevLett.51.1884](https://doi.org/10.1103/PhysRevLett.51.1884). URL: <https://link.aps.org/doi/10.1103/PhysRevLett.51.1884>.
- [129] L. J. Sham and M. Schlüter. ‘Density-functional theory of the band gap’. In: *Phys. Rev. B* 32 (6 Sept. 1985), pp. 3883–3889. DOI: [10.1103/PhysRevB.32.3883](https://doi.org/10.1103/PhysRevB.32.3883). URL: <https://link.aps.org/doi/10.1103/PhysRevB.32.3883>.
- [130] The Materials Project. ‘Materials Data on AlN by Materials Project’. In: (July 2020). DOI: [10.17188/1268470](https://doi.org/10.17188/1268470).
- [131] S. Shokhovets et al. ‘Determination of the anisotropic dielectric function for wurtzite AlN and GaN by spectroscopic ellipsometry’. In: *Journal of Applied Physics* 94.1 (July 2003), pp. 307–312. ISSN: 0021-8979. DOI: [10.1063/1.1582369](https://doi.org/10.1063/1.1582369). eprint: https://pubs.aip.org/aip/jap/article-pdf/94/1/307/19273892/307_1_online.pdf. URL: <https://doi.org/10.1063/1.1582369>.

- [132] M. Gajdoš et al. ‘Linear optical properties in the projector-augmented wave methodology’. In: *Phys. Rev. B* 73 (4 Jan. 2006), p. 045112. DOI: 10.1103/PhysRevB.73.045112. URL: <https://link.aps.org/doi/10.1103/PhysRevB.73.045112>.
- [133] Hosung Seo, Marco Govoni and Giulia Galli. ‘Design of defect spins in piezoelectric aluminum nitride for solid-state hybrid quantum technologies’. In: *Scientific Reports* 6.1 (2016), p. 20803. ISSN: 2045-2322. DOI: 10.1038/srep20803. URL: <https://doi.org/10.1038/srep20803>.
- [134] J. B. Varley, A. Janotti and C. G. Van de Walle. ‘Defects in AlN as candidates for solid-state qubits’. In: *Phys. Rev. B* 93 (16 Apr. 2016), p. 161201. DOI: 10.1103/PhysRevB.93.161201. URL: <https://link.aps.org/doi/10.1103/PhysRevB.93.161201>.
- [135] D. Alden et al. ‘Point-Defect Nature of the Ultraviolet Absorption Band in AlN’. In: *Phys. Rev. Appl.* 9 (5 May 2018), p. 054036. DOI: 10.1103/PhysRevApplied.9.054036. URL: <https://link.aps.org/doi/10.1103/PhysRevApplied.9.054036>.
- [136] Qimin Yan et al. ‘Origins of optical absorption and emission lines in AlN’. In: *Applied Physics Letters* 105.11 (Sept. 2014), p. 111104. ISSN: 0003-6951. DOI: 10.1063/1.4895786. eprint: https://pubs.aip.org/aip/apl/article-pdf/doi/10.1063/1.4895786/13302410/111104_1_online.pdf. URL: <https://doi.org/10.1063/1.4895786>.
- [137] Benjamin E. Gaddy et al. ‘Vacancy compensation and related donor-acceptor pair recombination in bulk AlN’. In: *Applied Physics Letters* 103.16 (Oct. 2013), p. 161901. ISSN: 0003-6951. DOI: 10.1063/1.4824731. eprint: https://pubs.aip.org/aip/apl/article-pdf/doi/10.1063/1.4824731/13673594/161901_1_online.pdf. URL: <https://doi.org/10.1063/1.4824731>.
- [138] Ramón Collazo et al. ‘On the origin of the 265 nm absorption band in AlN bulk crystals’. In: *Applied Physics Letters* 100.19 (May 2012), p. 191914. ISSN: 0003-6951. DOI: 10.1063/1.4717623. eprint: https://pubs.aip.org/aip/apl/article-pdf/doi/10.1063/1.4717623/13982698/191914_1_online.pdf. URL: <https://doi.org/10.1063/1.4717623>.
- [139] Yuri Ossetsky et al. ‘Native and radiation induced point defects in AlN and Sc-doped AlN’. In: *Phys. Rev. Mater.* 6 (9 Sept. 2022), p. 094603. DOI: 10.1103/PhysRevMaterials.6.094603. URL: <https://link.aps.org/doi/10.1103/PhysRevMaterials.6.094603>.
- [140] A. Sedhain et al. ‘The origin of 2.78 eV emission and yellow coloration in bulk AlN substrates’. In: *Applied Physics Letters* 95.26 (Dec. 2009), p. 262104. ISSN: 0003-6951. DOI: 10.1063/1.3276567. eprint: https://pubs.aip.org/aip/apl/article-pdf/doi/10.1063/1.3276567/14423732/262104_1_online.pdf. URL: <https://doi.org/10.1063/1.3276567>.